Washington University in St. Louis
Washington University Open Scholarship

Arts & Sciences Electronic Theses and Dissertations

Arts & Sciences

Spring 5-15-2020

Measurement, Dissipation, and Quantum Control with Superconducting Circuits

Patrick Harrington
Washington University in St. Louis

Follow this and additional works at: https://openscholarship.wustl.edu/art_sci_etds

Part of the Condensed Matter Physics Commons, and the Quantum Physics Commons

Recommended Citation

Harrington, Patrick, "Measurement, Dissipation, and Quantum Control with Superconducting Circuits" (2020). *Arts & Sciences Electronic Theses and Dissertations*. 2195.
https://openscholarship.wustl.edu/art_sci_etds/2195

This Dissertation is brought to you for free and open access by the Arts & Sciences at Washington University Open Scholarship. It has been accepted for inclusion in Arts & Sciences Electronic Theses and Dissertations by an authorized administrator of Washington University Open Scholarship. For more information, please contact digital@wumail.wustl.edu.

WASHINGTON UNIVERSITY IN ST. LOUIS
DEPARTMENT OF PHYSICS

Dissertation Examination Committee:
Kater Murch, Chair
James Buckley
Sophia Hayes
Erik Henriksen
Henric Krawzynski
Alexander Seidel

Measurement, Dissipation, and Quantum Control with Superconducting Circuits

by
Patrick Michael Harrington

A dissertation presented to
The Graduate School
of Washington University in
partial fulfillment of the
requirements for the degree
of Doctor of Philosophy

May 2020
Saint Louis, Missouri

© 2020 by Patrick Michael Harrington
All rights reserved.

Table of Contents

List of Figures **iv**

List of Tables **vi**

List of Abbreviations **vii**

Acknowledgements **viii**

1 Quantum Circuits, Quantum Information, and the Environment **1**
1.1 A prehistory of circuit quantum electrodynamics 1
1.2 Quantum information processing 4
1.3 The environment as a resource 5

2 Circuit Quantum Electrodynamics **9**
2.1 Quantum circuits 9
2.2 Interactions of light and matter 18
2.3 The dispersive Jaynes-Cummings interaction 22

3 Experiment Methods & Techniques **28**
3.1 Device preparation 28
3.2 Cryostat setup 33
3.3 Amplification 37

4 Open Quantum Systems **46**
4.1 A quantum system with its environment 46
4.2 Quantum measurement theory 54
4.3 Dispersive measurement of quantum bit 57

5 The Statistical Arrow of Time in Quantum Measurement **61**
5.1 A statistical arrow of time 63
5.2 Time reversal of quantum measurement trajectories 64
5.3 Reversibility with inefficient measurement 72
5.4 Measurement trajectories of a transmon qubit 80

6 Quantum Bath Engineering with a Photonic Crystal **92**
6.1 Bath engineering for quantum control 93
6.2 A photonic crystal to shape the density of states 98
6.3 A qubit coupled to a photonic crystal 101
6.4 Dressed state dissipation 108

Bibliography **121**

A Quantum Operator Methods **[140]**

B Photonic Crystal Fabrication Parameters **[142]**

List of Figures

3.1 Niemeyer-Dolan bridge junction fabrication . . . 31
3.2 A high frequency absorptive filter . . . 37
3.3 A lumped element schematic of a current driven JPA . . . 40
3.4 JPA steady state response . . . 42
3.5 A JPA capacitively coupled to a Z_0 impedance . . . 43
3.6 JPA design layout and gain profile . . . 45

5.1 Measurement backaction and time reversal . . . 67
5.2 Measurement update with time reversal . . . 67
5.3 A measurement trajectory and its backward-in-time evolution . . . 70
5.4 The arrow of time statistic for measurement trajectories . . . 71
5.5 The dynamics of dispersive measurement on the Bloch sphere . . . 74
5.6 Multiple measurement channels to model measurement inefficiency . . . 85
5.7 Unraveled quantum measurement trajectories . . . 85
5.8 Distributions of the statistical arrow of time . . . 86
5.9 A detailed fluctuation theorem . . . 87
5.10 Distributions of the arrow of time statistic for measurement projection . . . 89
5.11 An integral fluctuation relation to quantify absolute irreversibility . . . 90

6.1 Engineering a steady-state on the Bloch sphere . . . 95
6.2 Dressed qubit decay transitions . . . 97
6.3 Periodic impedance modulation of a transmission line. . . . 99
6.4 Photonic crystal scattering parameters . . . 99
6.5 Photonic crystal dispersion relation . . . 102
6.6 A 3D transmon coupled to a photonic crystal . . . 103
6.7 Cryostat wiring diagram . . . 104
6.8 Schematic model of the transmon, resonator, and photonic crystal . . . 106
6.9 Energy relaxation and Rabi drive measurements . . . 108
6.10 Characterizing the environment density of states . . . 109
6.11 Energy diagram of dressed qubit eigenstates . . . 110
6.12 Dissipation dynamics of the driven qubit . . . 113
6.13 Time evolution of dressed state decay . . . 116

6.14 Tomography of the driven qubit steady state 117
6.15 Relative jump transition rates of the dressed qubit 118
6.16 Steady state tomography of the qubit populations 119

List of Tables

3.1 Attenuator layout for the cryostat 36

5.1 Quantum trajectory experiment parameters 81

B.1 The photonic crystal impedance sections . . . . . [142]

List of Abbreviations

CPW	coplanar waveguide
cQED	circuit quantum electrodynamics
DC	direct current
HEMT	high electron mobility transistor
OFHC	oxygen-free high purity copper
JPA	Josephson parametric amplifier
POVM	positive operator-valued measure
QND	quantum non-demolition
RCSJ	resistively and capacitively shunted junction
RF	radio frequency
SQUID	superconducting quantum interference device
TE	transverse electric
TEM	transverse electromagnetic
VNA	vector network analyzer

Acknowledgements

Together with my family, friends, mentors, and colleagues, I recognize a journey's end while celebrating another adventure's beginning. During this momentary conclusion, I am delighted to share my gratitude for the support I have received throughout my graduate studies.

I wish to wholeheartedly acknowledge my advisor, Kater Murch. His insight and encouragement are connected to every fruitful aspect of my graduate research. Kater's admirable blend of acumen and enthusiasm has been integral to my growth as a scientist. I am sincerely grateful for his continual support of my opportunities to amalgamate impactful discovery and creative exploration.

I would like to extend a special thanks to James Buckley for his supportive role of my involvement in the Axion Dark Matter eXperiment collaboration and my development as a physicist overall. It has been a pleasure to have a mentor who teaches through his curiosity and determination to find satisfying explanations.

I am especially grateful for guidance from Erik Henriksen. Throughout my graduate studies, he has always been a resource for practical solutions that are often highly technical yet simple. I am thankful for many conversations with Alexander Seidel that have bridged my understanding of open quantum systems and condensed matter physics. I have great

appreciation for Henric Krawczynski, who has encouraged me to teach and mentor since the beginning of my graduate studies. I am thankful to Sophia Hayes, for her willingness to sit on my committee and read my dissertation.

I have tremendous gratitude for the Axion Dark Matter eXperiment collaboration. My involvement in the "cold electronics" efforts has enriched my graduate research. I am thankful for many and I wish to recognize Gianpaolo Carosi, Gray Rybka, Andrew Sonnenschein, Rakshya Khatiwada, Christian Boutan, and Nathan Woolett.

I am thankful for the consistent presence of the Murch research group during the past five years. I appreciate Dian Tan, Mahdi Naghiloo, and Neda Forouzani for sharing their lab knowledge at the beginning of my time in the lab. Day-to-day life would have not been the same without Jonathan Monroe as a thoughtful colleague and trusted friend. It has been a joy to work alongside Maryam Abassi, Taeho Lee, Xingrui Song, Zoe Wang, Daria Kowsari, Weijian Chen, and Chandrashekhar Gaikwad as we have grappled with baffling experiments, calculations, and fabrication processes. I have great appreciation for Tommy Alamin, for his commitment to his research projects and for jumpstarting our microwave design and fabrication. I am grateful for the undergraduate students whom I have been able to mentor and to collaborate with: Michael Seitanakis, Arman Guerra, and Beatrice Barrar.

I am grateful for collaborative opportunities on multiple research projects. I wish to thank David Wisbey and Jacob Brewster, for their advice and measurements to help improve device fabrication. I have appreciated discussions shared with Yogesh Joglekar, which have aided my understanding of open quantum systems in a theoretical framework. A significant portion of my research on quantum measurement has been enabled

by many conversations with Andrew Jordan, Justin Dressel, and Philippe Lewalle.

My time at Washington University began in the Institute of Material Science and Engineering (IMSE). I appreciate support from Katherine Flores during my first year of graduate studies. I am grateful for the dedicated IMSE staff, especially Beth Gartin and Rahul Gupta, who have provided and maintained a cleanroom facility for device fabrication.

I am very thankful for incredible support from within the Department of Physics. I wish to recognize the organizational help from Sarah Akin, Linda Trower, and Shirley McTigue, as well as the technical expertise of Todd Hardt, Denny Huelsman, Kenny Schmidt, and Garry Simburger.

I have deep appreciation for all those who have marked many seasons of my graduate experience with life-giving fullness. I am thankful for my friendships with Jesse Balgley and Jeni Fehr, both of whom have become like family. I wish to recognize the Cook family for their great support during any given visit home. I am certainly grateful for support (and many meals) from the Laing family during the writing of this dissertation. I am thankful for my family and their ongoing encouragement throughout my education and research. Finally, I express a loving and deep appreciation for Olivia, who has been patient and thoughtful in her support, while eager for the journey ahead.

Patrick M. Harrington

Washington University in St. Louis

May 2020

For my brothers & sisters
Andrew, Shannon, Kerry, Abby, and Jack

Chapter 1

Quantum Circuits, Quantum Information, and the Environment

1.1 A prehistory of circuit quantum electrodynamics

Quantum circuits were created for the observation of macroscopic quantum phenomena. In 1978, Anthony Leggett suggested a superconducting loop with a weak link could demonstrate quantum tunneling of a macroscopic degree of freedom [1], and he stated that the quantum coherence between the macroscopically distinct circuit states "would probably be as near as we are likely to get to a laboratory version of Schrödinger's Cat" [2]. The "ridiculous" [3, 4] scenario of quantum interference with arbitrarily complex macroscopic systems has been contemplated epistemologically and confronted through theoretical explanations since the inception of quantum mechanics. Physical models of quantum measurement [5–9], system-environment decoherence [10–17], and wavefuction collapse to a "preferred basis" [18–21] were proposed on a justifying premise that quantum in-

terference is *absent* on a macroscopic scale. However, these theoretical programs lacked rigorous discussion of macroscopic features aimed at experimental verification [22].

Once low temperature circuits were discovered to be feasible for the observation of quantum mechanics on a macroscopic scale, Leggett and others developed a path integral formalism for open quantum systems based on a Wentzel-Kramers-Brillouin approximation. Quantitative predictions were produced [23–27] for the tunneling of a Josephson tunnel junction circuit phase degree of freedom [28, 29]. Experimental tests to measure the tunnel junction "switching rate" [30–38] showed agreement with theory: macroscopic tunneling out of a metastable energy state is activated by thermal fluctuations at high temperature and, remarkably, quantum mechanical fluctuations at low temperatures. Tunneling rate models produced by in situ characterization of circuit parameters, showed strong quantitative agreement with parameter-free calculations [39–41]. From the onset of these experimental developments, an account of the strong interactions with environment degrees of freedom was considered essential for a quantum treatment of microwave circuitry. The tunneling rate experiments highlighted how quantum tunneling is *suppressed* by strong interactions with a dissipative electromagnetic environment [42–44].

The tunneling of singe electric charges was demonstrated by circuits in the "Couloumb blockade" regime, containing a capacitively decoupled metallic grain [45, 46] and these devices later showed evidence of electron superpositions [47–50]. Coherent charge-type superconducting circuits [51, 52] produced the first temporal demonstration of quantum coherence of a circuit plasmon mode resonance with non-adiabatic driving [53, 54]. This became known the Cooper-pair Box, and further experimentation [54–56]

included improvements to mitigate the deleterious effects of uncontrolled charge fluctuations on qubit coherence times [57–59]. Quantum state readout with a single-electron transistor [60] facilitated a mechanism for single shot readout of the qubit state [61, 62].

In 2004, the paradigm of *circuit quantum electrodynamics* (cQED) was initiated when Andreas Wallraff and others working in the group of Robert Schoelkopf adopted principles of cavity quantum electrodynamics [63] to demonstrate strong coupling of a charge qubit with a microwave resonator [64]. The experiment showcased quantum coherent control of the light-matter interaction with single photons with a solid state device. However, low frequency fluctuations of charge across the circuit Josephson junction continued to upset quantum coherence of the circuit. Schoelkopf proposed to electrically short the junction with a transmission line section, making a low impedance shunt for low frequencies while remaining a high impedance to the circuit plasmon mode [65]. The "*transm*ission line shunted plas*mon* oscillation circuit" inherited the moniker *transmon*, although the device debuted with a capacitive shunt instead [66, 67]. The dissipation of charge through the large capacitance essentially flattens the transmon circuit charge dispersion, making the circuit impervious to charge noise and directly resulted in an order of magnitude improvement of qubit coherence times [68]. The transmon circuit has since enabled exquisite control of quantum degrees of freedom in the microwave domain, and by becoming the workhorse of cQED, it is the foremost solid-state device architecture of scalable quantum information processing [69].

1.2 Quantum information processing

In the past four decades, superconducting circuit technology has converged with quantum information theory to implement quantum algorithms and perform quantum simulation. The motivation to encode and process quantum information is rooted in the inherent inefficiency of classical computers to model physical systems [70]. Quantum systems were proposed as a means to simulate, or calculate, complex physical phenomena that would be impossible to model on a classical computer [71, 72]. Quantum coherence between few discrete systems is modeled by linear superposition in an exponentially large Hilbert space, thereby presenting a resource for quantum computation [73]. In 1985, David Deutsch distilled these aspirations into a proposed universal quantum computer, which can be programmed to simulate any physical process [74–76].

The cultivation of quantum information theory has been accompanied by technological development of quantum coherent devices. The progress toward a programmable quantum computer has been marked by advancements in the creation, storage, control, and measurement of quantum states of light and matter [77]. This necessitates a bridge across the ostensible quantum-classical boundary, with a capability to dictate quantum coherent operations with macroscopic degrees of freedom. All realistic quantum computation devices are inherently open quantum systems and the preparation and measurement of quantum states requires interaction at the quantum-classical boundary. In this, there appears to be a trade-off between quantum coherence and quantum control; the environment which mediates the control and measurement of a quantum system can also compromise coherent superpositions of computational states. Thus, well controlled environment de-

grees of freedom are necessary for quantum device technology.

1.3 The environment as a resource

In circuit quantum electrodynamics, quantum degrees of freedom naturally interact strongly in comparison to the energy scale of microwave frequencies electromagnetic excitations. This places superconducting qubit in contrast to other platforms for quantum computation, since interactions between quantum circuits, resonators, and their environment can be uniquely tailored for quantum processor "programmability" with classical controls. However, the time scale for quantum coherence of superconducting circuits is limited by interactions with an environment that seemingly evades equilibrium. Coherence time scales are characteristic of the quantum circuit fabrication quality and can be improved by microwave engineering "hygiene" aimed at isolating fragile quantum degrees of freedom from an uncontrolled fluctuating environment.

While it is advantageous to decouple a quantum system from an uncontrolled environment, interactions with a controlled environment present a resource for quantum computation. Environment degrees of freedom form the basis of quantum state preparation of measurement: the process of encoding classical information on quantum degrees of freedom (and vice versa) is mediated by environment degrees of freedom. As witnessed in the earliest quantum circuit experiments, dissipation can localize quantum degrees of freedom. This principle led to the burgeoning of cQED through the development of the transmon circuit, as dissipation of uncontrolled charge fluctuations, in a dual sense, localizes the circuit phase degree of freedom.

Quantum bath engineering[1] is a modality of quantum control using many degrees of freedom of an environment [78]. The system-environment interactions of quantum bath engineering methods are tailored for selective dissipation involving quantum degrees of freedom of the system. A quantum bath engineering protocol reliably involves classical control, such as coherent driving. A central concept of quantum bath engineering is that effective, and usually nonunitary, system dynamics result from ignoring distinct instances of the environment state at a given time.

An early example of dissipation engineering is laser cooling of atoms, where drive in combination with atomic decay is used to initialize atomic states [79]. Such techniques have been extended to cool mechanical objects through cavity dissipation [80] and for control of quantum circuits [81]. The dynamics open quantum systems enabled by quantum bath engineering has applications for quantum state reset [82, 83], stabilization of quantum states [82, 84–92], creation of subspaces that are decoherence free [93] or conserve excitation number [94–96], and the implementation of quantum error correction [97–99]. These quantum bath engineering methods in cQED involve both spectral and temporal control of environment degrees of freedom. In practice, the spectral composition of the electromagnetic environment is designed from its microwave impedance and temporally controlled driving allows the energy selective coupling to environment degrees of freedom.

Quantum bath engineering principles are markedly pronounced in the process of quantum measurement: there are undetected, and ignored, environment degrees of freedom

[1] Quantum bath engineering is also called *quantum reservoir engineering*, *engineered dissipation*, *autonomous feedback*, and *coherent feedback*.

which, *for all practical purposes*, erase quantum coherence during wavefunction collapse. Quantum measurement dynamics, accompanied by each measurement result, provides additional selectivity for quantum control. Since measurement results are correlated to macroscopic states of the environment, quantum dynamics conditioned on these measurement results simulates a feedforward control process on the quantum state. Measurement post-selection techniques have application for quantum error correction, however the statistics of conditional dynamics does not scale favorably with quantum system size.

Nevertheless, the statistics of quantum measurement outcomes are intertwined with the dynamics of wavefunction collapse. And, in terms of quantum bath engineering, the dynamics of wavefunction collapse can be dictated by quantum measurement outcomes. In this dissertation, I present an experiment to characterize a statistical arrow of time in continuous quantum measurement trajectories of a superconducting qubit [100]. The experimental results show qubit measurement dynamics and statistics are correlated for a single measurement trajectory evolving forward-in-time. Moreover, an emergent statistical arrow of time is revealed by ensembles of measurement trajectories. A statistical arrow of time attributes a "second law"-like description to wavefunction collapse, and furthermore, measurement ensembles adhere to an entropy-like fluctuation theorem.

Following this discussion, I present an experiment which demonstrates qubit state stabilization by dissipative interactions with a microwave photonic crystal environment [101]. The photonic crystal is created as a step-impedance transmission line which structures the electromagnetic spectral density of states. Near the photonic crystal band edge, a coher-

ent drive near the qubit transition imparts selective dissipation of the qubit state. On a short time scale, the qubit then stabilizes to a desired effective ground state. Through this bath engineering protocol, these results demonstrate how the many electromagnetic modes that form bands and gaps of a photonic crystal present a resource for quantum state preparation.

In Chapter 2, I present a theoretical background of circuit quantum electrodynamics by discussing lumped element nonlinear circuits, the Jaynes-Cummings interaction, and dispersive measurement. In Chapter 3, I present a technical description of quantum circuit experiments by giving an overview of fabrication, experiment setup, and signal amplification. Next, in Chapter 4, I develop a model of open quantum system dynamics applicable to dissipation and measurement of superconducting qubit states. Then, in Chapter 5, I discuss the characterization of a statistical arrow of time in continuous quantum measurement. Then, in Chapter 6, I discuss a bath engineering experiment which demonstrates quantum state stabilization using a photonic crystal environment.

Chapter 2

Circuit Quantum Electrodynamics

2.1 Quantum circuits

2.1.1 Quantization of a linear circuit

The interaction of light and matter is central to quantum electrodynamics. As photons mediate the interaction of charged particles, a description of the electromagnetic field is inseparable from the physics of current and voltage. Electrons and electrical circuits alike are accompanied by the quantization of electromagnetic energy. For this reason, electromagnetic energy localized by a microwave resonator occupies discrete energy levels. The electromagnetic energy of an electrical circuit is shared between the quantum degrees of freedom of matter and light in terms of charge and flux.

In the case of a lumped element LC circuit, the quantum degrees of freedom are the displacement charge $\hat{q}$, contributing capacitive energy $\hat{q}^2/2C$, and the generalized flux $\hat{\phi}$,

contributing inductive energy $\hat{\phi}^2/2L$ [102]. The circuit Hamiltonian is

$$\hat{H} = \frac{\hat{q}^2}{2C} + \frac{\hat{\phi}^2}{2L}, \tag{2.1.1}$$

where the operators $\hat{q}$ and $\hat{\phi}$ are canonically conjugate operators: $[\hat{\phi}, \hat{q}] = i\hbar$. We recognize the Hamiltonian (Eq. 2.1.1) as a quantum harmonic oscillator and rewrite the charge and flux operators in terms of creation and annihilation operators

$$\hat{\phi} = \phi_{\mathrm{ZPF}}(a + a^\dagger), \quad \hat{q} = -iq_{\mathrm{ZPF}}(a - a^\dagger). \tag{2.1.2}$$

where $\phi_{\mathrm{ZPF}} = \sqrt{\hbar Z/2}$ and $q_{\mathrm{ZPF}} = \sqrt{\hbar/2Z}$ are the zero point fluctuation amplitudes of the harmonic oscillator ground state and $Z = \sqrt{L/C}$ is the characteristic impedance of the resonator. The Hamiltonian of the resonator is

$$\hat{H} = \hbar\omega_0\left(a^\dagger a + \frac{1}{2}\right), \tag{2.1.3}$$

where $\omega_0 = 1/\sqrt{LC}$ is the resonant frequency of the circuit.

At a given moment, and while in equilibrium with an environment, thermal fluctuations and quantum fluctuations of charge and flux account for the electromagnetic energy stored in the microwave circuit. For reasonable circuit parameters ($L \sim$ nH, $C \sim$ pF), the quantized energy levels are spaced by $\hbar\omega_0 \sim \hbar(2\pi \cdot 5\,\mathrm{GHz})$. A resonator of this frequency occupies its ground state at sub-Kelvin temperatures, such that $k_\mathrm{B}T \ll \hbar\omega$ for $k_\mathrm{B}/h = 20.8\,\mathrm{GHz/K}$. At these low temperatures, the suppression of thermal excitations

from electromagnetic blackbody radiation can make apparent the quantum fluctuations of the microwave circuit ground state.

We make measurements of a quantum circuit by scattering microwave pulses which are both time and frequency dependent. An interaction between a circuit and its electromagnetic environment is necessary to perform measurement. The measurement pulses originate from, and scatter into, a transmission line containing a continuum of electromagnetic modes [103]. Each independent electromagnetic mode contains conjugate charge and flux degrees of freedom. The effect of an electromagnetic environment on the *LC* circuit is modeled as a lumped element frequency dependent shunting admittance.

An excitation of the original circuit mode (Eq. 2.1.3) is shared with the many modes of electromagnetic continuum [42], such that the shunting admittance effectively damps and shifts the original *LC* circuit resonance as [104],

$$\omega_0 \rightarrow \omega_0 + \left(\Delta + \frac{j\omega_0}{2Q}\right) \simeq \omega_0\left(1 + \frac{j}{2}Z_0 Y(\omega_0)\right), \tag{2.1.4}$$

where Δ is the frequency shift of the resonance and Q is the resonance coupled quality factor. The resonance of the shunted circuit is approximated by the original *LC* circuit mode, given sufficiently weak damping. Weak damping is required for observation of individual quantum energy levels of this mode, since the spacing of energy levels must be larger than energy level broadening due to hybridization with many environment modes.

Since dissipation can "wash out" the quantum character of a circuit, quantum circuits are made of materials that contribute minimal electrical loss. A low temperature environ-

ment suppresses the thermal occupation of not only electromagnetic modes, but also the phononic modes of the circuit's material environment. As such, the low temperature behavior of materials such as silicon and sapphire have desirable insulating properties, since the "wires" of a circuit must rest on a substrate of low conductance. On the other hand, the circuit wires must have exceptionally low resistance. Crucially, low temperatures enable the electronic state of some materials, such as aluminum and niobium, to condense into a superconducting phase. The nearly negligible current loss of the superconducting state significantly eliminates dissipation into the continuum of phononic modes.

2.1.2 Tunneling of Cooper pairs

A classically driven linear circuit responds identically in the quantum regime as it does in the classical limit. In contrast, a nonlinear circuit in the quantum regime responds with distinctly quantum mechanical behavior in comparison to its response in the classical limit [2, 105]. An anharmonic oscillator has a classical fundamental frequency, and infinite harmonics, which do not match the transition frequencies between low-lying energy levels [106]. In the quantum limit, energy eigenstates of an anharmonic oscillator can be addressed individually with classical driving, due to the unequal spacing of energy levels. In turn, an anharmonic oscillator exhibits observable quantum interference between individual energy eigenstates which cannot be described in terms of a classical oscillator response. To modify a linear *LC* circuit (Eq. 2.1.3) into an anharmonic oscillator, we introduce a dissipationless nonlinear circuit element known as a Josephson tunnel junction.

A Josephson junction consists of a two superconductors separated by an insulating

barrier. In the absence of a bias potential, current can flow between the superconductors by quantum tunneling through the insulating barrier. Although a junction geometry and its specific material properties introduce a linear electrical impedance, the quantum coherent tunneling of Cooper pairs through the insulating barrier creates an additional nonlinear electromagnetic response. In contrast to electron tunneling in normal metals, the tunneling of Cooper pairs is a coherent process between discrete states of the coherent superconducting ground state [107].

We develop a phenomenological description of Josephson tunneling by considering two superconductors separated by a tunneling barrier, with a total number of Cooper pairs $N = N_{\mathrm{L}} + N_{\mathrm{R}}$, where N_{L} and N_{R} are the number of Cooper pairs in superconductor L and R respectively. If the system is initially in the state $|\Psi_{\mathrm{L}}, \Psi_{\mathrm{R}}\rangle = |N_{\mathrm{L}}, N_{\mathrm{R}}\rangle$, then the tunneling of n Cooper pairs from L to R results in a new superconducting state

$$|n\rangle = |N_{\mathrm{L}} - n, N_{\mathrm{R}} + n\rangle \,. \tag{2.1.5}$$

We define the number operator $\hat{n}$ which counts the number of Cooper pairs which have tunneled through the junction,

$$\hat{n}\,|n\rangle = \left(\sum_m m|m\rangle\langle m|\right)|n\rangle = n\,|n\rangle \,. \tag{2.1.6}$$

The states $|m\rangle$ are degenerate in energy, since there is an insignificant energetic cost to add a Cooper pair to the superconducting ground state. However, there is an energetic cost for the tunneling process; the coherent tunneling between the superconducting states is

described by the hopping interaction

$$\hat{H} = -\frac{1}{2}E_J \sum_n |n\rangle\langle n+1| + |n+1\rangle\langle n|, \tag{2.1.7}$$

where E_J is the Josephson coupling energy. We recognize that Eq. 2.1.7 describes one-dimensional nearest neighbor hopping. The hopping of a Cooper pair from the left to right superconductor is described by the unitary operator

$$e^{i\hat{\theta}} |n\rangle = |n+1\rangle , \tag{2.1.8}$$

where the phase operator $\hat{\theta}$ is the generator of discrete translations of Cooper pairs. The phase operator $\hat{\theta}$ is canonically conjugate to the number operator, together sharing the commutation relation $[\hat{n}, \hat{\theta}] = i$. We apply the operation of Equation 2.1.8 to the Hamiltonian (Eq. 2.1.7) to find

$$\hat{H} = -E_J \cos\hat{\theta}. \tag{2.1.9}$$

The eigenstates of the hopping Hamiltonian (Eq. 2.1.7) are simultaneous eigenstates of the phase operator. The energy eigenstates are the superpositions

$$|\theta\rangle = \sum_n e^{i\hat{n}\theta} |n\rangle , \tag{2.1.10}$$

which describe a constant current of tunneling Cooper pairs.

As each tunneled Cooper pair displaces $2e$ of charge across the junction we define the operator $\hat{q} = (2e)\hat{n}$ as the charge operator. For an energy eigenstate $|\theta\rangle$, we solve for the ex-

pectation value of persistent current by employing the Ehrenfest theorem: $I = d\langle\hat{q}\rangle/dt = (i/\hbar)\langle[\hat{H},\hat{q}]\rangle$. From this, we recover the first Josephson relation:

$$I(\theta) = \frac{2e}{\hbar}E_J \sin\theta = I_c \sin\theta. \tag{2.1.11}$$

where $I_c = E_J/\varphi_0$ is the junction critical current and φ_0 is the reduced flux quantum $\varphi_0 = \hbar/2e$.

If we apply a constant bias potential of voltage V across the junction, the interaction Hamiltonian becomes

$$\hat{H} = -2eV\hat{n} - E_J \cos\hat{\theta}. \tag{2.1.12}$$

From Equation 2.1.12, we find the second Josephson relation by solving for the equation of motion for the phase. The phase evolves as

$$\frac{d\langle\hat{\theta}\rangle}{dt} = \frac{i}{\hbar}\langle[\hat{H},\hat{\theta}]\rangle = \frac{2e}{\hbar}V, \tag{2.1.13}$$

which gives the equation

$$V = \varphi_0 \frac{d\langle\hat{\theta}\rangle}{dt}. \tag{2.1.14}$$

2.1.3 Quantization of a nonlinear circuit

We examine a nonlinear quantum circuit by revisiting the linear LC circuit model (Eq. 2.1.1) and replacing the inductor with a lumped element Josephson junction. The nonlinear circuit then consists of a capacitively shunted Josephson junction. The circuit nodes on either

side of the capacitor are the two superconductors tunnel coupled by the junction. This circuit has the Hamiltonian,

$$\hat{H} = \frac{\hat{q}^2}{2C} - E_J \cos\hat{\theta}. \tag{2.1.15}$$

The phase operator $\hat{\theta}$ does not correspond directly to the flux operator $\hat{\phi}$ for the original linear LC circuit linear inductance (Eq. 2.1.1), although these operators are both generators of charge translations, being conjugate to the charge operator. The phase operator is defined as a compact variable, being the generator for *discrete* changes of charge (Eq. 2.1.8) across the junction, it is 2π-periodic. In contrast, the flux operator is defined on the real line, since it is the generator for continuous charge translations [107]. These operators are reconciled by considering the energetics of the circuit when shunted by an inductance L that is arbitrarily large [108].

The added linear inductance contributes a term $\hat{\phi}^2/2L$ to the circuit Hamiltonian. By Faraday's law, a change in the flux induces a voltage across the circuit nodes; the junction phase follows the flux proportionally, according to the second Josephson relation. Since the phase couples directly to the flux degree of freedom, the additional parabolic flux term in the Hamiltonian breaks the degeneracy of Hamiltonian eigenstates that are 2π-periodic in phase. Since this phase symmetry is tacitly broken by an arbitrary large parasitic inductance, we replace the phase operator $\hat{\theta}$ with the normalized flux operator $\hat{\varphi} = \hat{\phi}/\varphi_0$ which is defined on the continuous real line. We take the circuit Hamiltonian to be

$$\hat{H} = 4E_C\hat{n}^2 - E_J \cos\hat{\varphi}, \tag{2.1.16}$$

where $E_C = e^2/2C$ is the capacitive energy per electron charge and we have expressed the capacitive charging energy in terms of number of Cooper pairs.

According to the virial theorem, the charge and phase degrees of freedom equally share the zero point energy fluctuations of the circuit wavefunction. In the limit $E_J \gg E_C$, we self-consistently approximate the circuit as a harmonic oscillator [109] and find the amplitude of phase excursions is relatively small. Since the phase is well localized, we refer to it as a position coordinate. The phase-dependent cosine term has the role of an energetic potential. We similarly associate the capacitive energy to kinetic energy, since charge contributions do not affect the energy eigenstates.

Since the phase coordinate is well localized, we series expand the cosine potential of Equation 2.1.16 to perturbatively investigate the energetics of the circuit,

$$\hat{H} = 4E_C\hat{n}^2 + \frac{E_J}{2}\hat{\varphi}^2 - \frac{E_J}{24}\hat{\varphi}^4. \tag{2.1.17}$$

The first and second terms of the Hamiltonian together are a linear LC circuit resonance. We identify the Josephson junction contributes an effective linear inductance defined from the relation $E_J = {\varphi_0}^2/L_J$, and the harmonic oscillator resonance is $\sqrt{8E_JE_C}$, upon neglecting the quartic term of the Hamiltonian.

Since the circuit is a harmonic oscillator in the perturbative limit ($E_J \gg E_C$), we employ harmonic oscillator ladder operators in terms of the normalized charge and flux operators,

$$\hat{\varphi} = \varphi_{\mathrm{ZPF}}(a + a^\dagger), \quad \hat{n} = -in_{\mathrm{ZPF}}(a - a^\dagger), \tag{2.1.18}$$

where the amplitudes of zero point fluctuations are,

$$\varphi_{\text{ZPF}} = \left(\frac{2E_C}{E_J}\right)^{1/4}, \quad n_{\text{ZPF}} = \left(\frac{E_J}{32E_C}\right)^{1/4}. \tag{2.1.19}$$

After applying normal ordering the Hamiltonian ladder operators and removing constant terms, we make a rotating wave approximation. Here, the rotating wave approximation is applicable since excitation non-conversing operators oscillate rapidly in the Heisenberg picture, relative to the interaction timescale of interactions between eigenstates of the ladder operators. Low energy excitations of the circuit are described by the Hamiltonian

$$\hat{H} \simeq \left(\sqrt{8E_J E_C} - E_C\right) a^\dagger a - \frac{E_C}{2} a^\dagger a^\dagger a a. \tag{2.1.20}$$

We find the negative quartic term of Equation 2.1.17 renormalizes the harmonic oscillator resonance by $-E_C$ and introduces a relative anharmonicity $-E_C$ between the first and second energy level transitions. The Hamiltonian (Eq. 2.1.20) describes the lowest three energy levels of a quantum circuit known as a *transmon* [66].

2.2 Interactions of light and matter

2.2.1 A qubit from a circuit

When the anharmonicity $-E_C$ of Equation 2.1.20 is large compared to the timescale of driven circuit dynamics, we can treat the anharmonicity as infinite to describe the dynamics of the two lowest circuit energy levels. With this approximation, we truncate the

circuit Hilbert space to two dimensions, realizing a qubit system. A qubit is analogous to the spin degree of freedom of a non-relativistic spin-1/2 particle, which is represented by a two-component spinor defined in an operator space by Pauli matrices.

We choose the Pauli σ_z operator to commute with the qubit energy eigenstates. The Hamiltonian for the qubit system is

$$\hat{H} = \omega_q \sigma^\dagger \sigma, \tag{2.2.1}$$

where ω_q is the bare qubit frequency and $\sigma = (\sigma_x + i\sigma_y)/2$ is the lowering operator. For a transmon circuit, the bare qubit frequency is (setting $\hbar = 1$),

$$\omega_q = \sqrt{8E_J E_C} - E_C. \tag{2.2.2}$$

2.2.2 The Jaynes-Cummings system

The Jaynes-Cummings Hamiltonian describes the interaction of an electromagnetic mode and a qubit provided they share a weak dipole-dipole interaction, relative to the characteristic energy of each system [110]. The qubit is defined in a two-dimensional Hilbert space $\mathcal{H}_q$, while the resonator state space is defined in the countably infinite Hilbert space $\mathcal{H}_r$ of a harmonic oscillator. The composite state space of the qubit and oscillator is defined in a tensor product space, $\mathcal{H}_q \otimes \mathcal{H}_r$. By expressing operators of the qubit and oscillator in this

space, we write the Jaynes-Cummings Hamiltonian as

$$\hat{H} = \omega_r\left(a^\dagger a \otimes \mathbb{1}_2\right) + \omega_q\left(\mathbb{1} \otimes \sigma^\dagger\sigma\right) + g\left(a \otimes \sigma^\dagger + a^\dagger \otimes \sigma\right), \tag{2.2.3}$$

where ω_r is the resonator frequency and $2g$ is the rate of vacuum Rabi oscillations.

Diagonalization of the Jaynes-Cummings Hamiltonian

We directly solve for the system eigenstates and energy spectrum by first expressing ladder operators as matrices in the operator product space,

$$\hat{H} = \begin{pmatrix} \omega_q\sigma^\dagger\sigma & \sqrt{1}g\sigma^\dagger & 0 & \\ \sqrt{1}g\sigma & \omega_r\mathbb{1}_2 + \omega_q\sigma^\dagger\sigma & \sqrt{2}g\sigma^\dagger & \cdots \\ 0 & \sqrt{2}g\sigma & 2\omega_r\mathbb{1}_2 + \omega_q\sigma^\dagger\sigma & \\ & \vdots & & \ddots \end{pmatrix}, \tag{2.2.4}$$

We then express the Pauli operators in matrix form to reveal the block diagonal structure of the Hamiltonian,

$$\hat{H} = \begin{pmatrix} 0 & 0 & 0 & \\ 0 & M_1 & 0 & \cdots \\ 0 & 0 & M_2 & \\ & \vdots & & \ddots \end{pmatrix}. \tag{2.2.5}$$

The block diagonal submatrices are

$$M_n = \begin{pmatrix} (n-1)\omega_r + \omega_q & \sqrt{n}g \\ \sqrt{n}g & n\omega_r, \end{pmatrix} \tag{2.2.6}$$

$$= \left(n\omega_r + \frac{\Delta}{2}\right)\mathbb{1}_2 + \frac{\Delta}{2}\sigma_z + \frac{\sqrt{n}g}{2}\sigma_x, \tag{2.2.7}$$

where $\Delta = \omega_q - \omega_r$ is the qubit-resonator detuning. Each submatrix represents a subspace of n total excitations between the qubit and resonator. We diagonalize each submatrix independently in an orderly fashion by defining the trigonometric relations

$$\cos 2\theta_n = \frac{\Delta}{g_n}, \quad \sin 2\theta_n = \frac{2\sqrt{n}g}{g_n}, \tag{2.2.8}$$

where

$$g_n = \sqrt{\left(2\sqrt{n}g\right)^2 + \Delta^2} \tag{2.2.9}$$

is the excitation number dependent rate of Rabi oscillations between the qubit and resonator. The Jaynes-Cummings Hamiltonian has a unique zero energy ground state $\epsilon_0 = 0$, corresponding to zero excitations in the system, while the energy eigenvalues for each excitation subspace are

$$\epsilon_{n,\pm} = \left(n\omega_r + \frac{\Delta}{2}\right) \pm \frac{g_n}{2}. \tag{2.2.10}$$

The eigenstates of each excitation subspace are

$$|n_-\rangle = \cos\theta_n \,|m,\, g\rangle - \sin\theta_n \,|m-1,\, e\rangle \tag{2.2.11}$$

$$|n_+\rangle = \sin\theta_n \,|m,\, g\rangle + \cos\theta_n \,|m-1,\, e\rangle\,, \tag{2.2.12}$$

where we express the eigenstates in a basis of the bare qubit and resonator, such that m denotes the number of photons in the resonator and the labels $\{g, e\}$ denote the ground and excited state of the qubit. The mixing angle $\theta_n = \arctan\left(2\sqrt{n}g/\Delta\right)/2$ prescribes the relative mixing of the bare qubit and resonator for a given excitation number.

The eigenstates $|n_\pm\rangle$ are degenerate eigenstates of the excitation number operator $\hat{N} = a^\dagger a + \sigma^\dagger\sigma$ for the qubit and resonator together. Since the full Jaynes-Cummings Hamiltonian is composed of the excitation subspaces *independently*, the eigenstates are simultaneous eigenstates of the total excitation number operator, $[\hat{H}, \hat{N}] = 0$, which is a Hamiltonian symmetry endowed from the rotating wave approximation.

2.3 The dispersive Jaynes-Cummings interaction

2.3.1 The dispersive approximation

We now investigate the Jaynes-Cummings system in the dispersive regime. Dispersively interacting degrees of freedom influence each other's energetic dispersion without necessarily exchanging energy. In the present context, we make a dispersive approximation in the large detuning limit $g \ll \Delta$, such that the exchange interaction of Equation 2.2.3

can be treated as a density-density interaction for the low energy excitations of the Jaynes-Cummings interaction.

This effective interaction results from a Schrieffer-Wolff transformation of the Jaynes-Cummings Hamiltonian (Eq. 2.2.3) [111]. The Hamiltonian is diagonalized to first-order in the exchange interaction by the transformation $\hat{H} \rightarrow U\hat{H}U^{\dagger}$, with unitary operator

$$U = \exp\left[\frac{g}{\Delta}(a \otimes \sigma^{\dagger} - a^{\dagger} \otimes \sigma)\right]. \tag{2.3.1}$$

We make the dispersive approximation by applying the unitary transformation (Eq. 2.3.1) and retaining terms up to second order in g/Δ. The Jaynes-Cummings Hamiltonian in the linear dispersive regime is [112]

$$\hat{H} = \omega_r\left(a^{\dagger}a \otimes \mathbb{1}_2\right) + \omega_r\left(\mathbb{1} \otimes \sigma^{\dagger}\sigma\right) + \chi\left(a^{\dagger}a \otimes \sigma^{\dagger}\sigma\right), \tag{2.3.2}$$

where $\chi = \frac{g^2}{\Delta}$ is the dispersive shift. As the dispersive Hamiltonian (Eq. 2.3.2) is applicable for low energy excitation of the Jaynes-Cummings Hamiltonian, this approximation breaks down for large excitation numbers, scaling with the resonator photon occupation $n_c = \Delta^2/4g^2$, called the critical photon number. The dispersive interaction describes an excitation number dependent shift of the qubit resonance. Likewise, the resonator frequency effectively shifts by 2χ whether the qubit is in the ground or excited state.

2.3.2 Dispersive measurement

Adding a drive

In experiment, coherent microwave drives are used to measure and control quantum circuits and resonators. For example, a weakly coupled microwave drive can be a absorptive probe to indicate energetic transitions or a method to pump excitations into the system. Alternatively, an intense microwave tone can strongly perturb a quantum system, induce otherwise forbidden transitions, and pump the system into the classical regime.

The effect of driving a resonator is characterized by dipole coupling to an electromagnetic mode of the environment. Here we apply a semiclassical steady state treatment by considering strong coherent driving with a sufficiently dissipative environment mode. An electromagnetic mode of the environment, with an annihilation operator b and at the drive frequency ω_d, interacts with a resonator mode through a dipole coupling within the rotating wave approximation,

$$\hat{H} = \omega_r a^\dagger a + \omega_d b^\dagger b + \left(g a b^\dagger + g^* a^\dagger b\right). \tag{2.3.3}$$

Given the environment mode is sufficiently dissipative, the mode is occupied by a coherent state described by a classical steady state solution of driven mode. If the coherent state has a large amplitude, and the environment state is not affected by state of the resonator mode, we make the stiff pump approximation and ignore effects of quantum fluctuations. The stiff pump approximation allows the replacement of the environment mode ladder operators with the steady state amplitude of the environment field. The Hamiltonian for

the driven resonator mode is

$$\hat{H}(t) = \omega_r a^\dagger a + \left(\epsilon e^{-i\omega_d t} a + \epsilon^* e^{+i\omega_d t} a^\dagger\right), \tag{2.3.4}$$

where the Hamiltonian has explicit time dependence in the Heisenberg picture and the ϵ is the effective coupling rate of the resonator and environment. In this semiclassical description, the effective coupling rate to the environment is enhanced by the high excitation number of the coupled resonator-mode interaction. Note this is similar to the excitation number dependent Rabi oscillation rate in the resonant Jaynes-Cummings model.

To eliminate the time dependence of the Hamiltonian (Eq. 2.3.4), we move to the rotating frame of the drive by applying the unitary transformation $U = e^{i\omega_d a^\dagger a t}$,

$$\hat{H} = \Delta_d a^\dagger a + \left(\epsilon a + \epsilon^* a^\dagger\right), \tag{2.3.5}$$

where $\Delta_d = \omega_r - \omega_d$ is the resonator-drive frequency detuning.

The displaced frame of the resonator field

The state of a qubit that is dispersively coupled to a resonator can be determined from a measurement of the resonator response. Here we consider a measurement probe near the resonance frequency of a dissipative resonator. A detailed description of a dissipative quantum system is explained in Chapter 4. We consider a coherent drive of amplitude ϵ is applied to the bare resonator frequency such that the qubit-resonator density matrix

evolves as

$$\dot{\rho} = -i[\hat{H}, \rho] + \kappa \mathcal{D}[a]\rho, \tag{2.3.6}$$

where $\mathcal{D}[a]\rho = (2a\rho a^\dagger - a^\dagger a\rho - \rho a^\dagger a)/2$ is the Lindblad dissipator and the Hamiltonian of the qubit and resonator is,

$$\hat{H} = -\chi a^\dagger a \sigma_z + \epsilon^* a + \epsilon a^\dagger. \tag{2.3.7}$$

We move into the displaced frame of the resonator by defining a displaced operator of the resonator field $d = a - \bar{a}$. The resonator dissipation superoperator is then,

$$\begin{aligned} \kappa \mathcal{D}[a]\rho &= \kappa \mathcal{D}[\bar{a} + d]\rho \\ &= -i[\Delta\hat{H}, \rho] + \kappa \mathcal{D}[a]\rho, \end{aligned} \tag{2.3.8}$$

where $\Delta\hat{H}$ becomes an additional term to the Hamiltonian,

$$\Delta\hat{H} = \frac{i\kappa}{2}(\bar{a}^* d - \bar{a} d^\dagger). \tag{2.3.9}$$

The resonator field is displaced according to the classical steady-state of the resonator field, which in the limit where $\chi \ll \kappa$, the classical steady state amplitude is

$$\bar{a} = \frac{\epsilon}{i\kappa/2}, \tag{2.3.10}$$

and the intra-resonator photon number is $\bar{n} = |\bar{a}|^2$. The additional Hamiltonian term is then

$$\Delta\hat{H} = \epsilon d^\dagger + \epsilon^* d^\dagger, \tag{2.3.11}$$

We absorb the term $\Delta\hat{H}$ into the Hamiltonian and rewrite the Hamiltonian in terms of the displaced field,

$$\begin{aligned}
\hat{H} &= -\chi(\bar{a}+d)^\dagger(\bar{a}+d)\sigma_z \\
&\qquad + \epsilon^*(\bar{a}+d) + \epsilon(\bar{a}+d)^\dagger + \Delta\hat{H} \\
&= -\chi(\bar{n} + d^\dagger d) - \chi(\bar{a}^* d + \bar{a} d^\dagger)\sigma_z \\
&\qquad + \underbrace{\bar{a}^*\epsilon + \bar{a}\epsilon^*}_{\to 0} + \underbrace{\epsilon d^\dagger + \epsilon^* d}_{-\Delta\hat{H}} + \Delta\hat{H} \\
\hat{H} &= -\chi(\bar{n} + d^\dagger d) - \chi(\bar{a}^* d + \bar{a} d^\dagger)\sigma_z.
\end{aligned} \tag{2.3.12}$$

We choose the phase of the resonator drive, without loss of generality, such that the field displacement is real valued. We also remove the constant term in the effective Hamiltonian to find

$$\hat{H} = -\chi d^\dagger d - 2\chi\sqrt{\bar{n}}(d + d^\dagger)\sigma_z. \tag{2.3.13}$$

The qubit-resonator interaction term of Equation 2.3.13 indicates that, in steady state, expectation values of the qubit are correlated to a single quadrature of the resonator field. A homodyne measurement of the cavity field, in the basis of this quadrature, is then an indirect measurement of the bare qubit populations.

Chapter 3

Experiment Methods & Techniques

3.1 Device preparation

3.1.1 Microfabrication

In the previous chapters, I have discussed the quantum mechanics of electromagnetic modes and circuits with a theoretic framework applicable to the physics of a single atom. However, electromagnetic modes at microwave frequencies have a length scale of millimeters, and quantum circuits are fabricated by materials with macroscopic properties. Microwave devices are made of distributed circuit elements; the near-field electromagnetic response of the circuit is determined by the geometry of its materials. Electron beam and optical lithography define the sub-microwave wavelength features of superconducting quantum circuits, and importantly, these techniques are integral to the fabrication of Josephson tunnel junctions.

Lift-off process

A transmon circuit device is fabricated on a silicon substrate as two aluminum superconductors that are coupled both capacitively and by a Josephson tunnel junction. The geometry of the circuit is defined by thin film deposition through a lithographic mask in a lift-off process. The workflow of fabrication by a lift-off process is described through the following steps:

The mask is created by first spin-coating electron sensitive polymer resist on an intrinsic silicon wafer. The resist coated wafer is then exposed to an electron beam that patterns the planar geometry of the circuit. After exposure, the sample is developed in a solvent solution which selectively removes the exposed resist while leaving the unexposed resist intact. The developing is stopped after a prescribed development time by plunging the sample in solution. The sample is subsequently rinsed and dried. Since residual resist adheres to the substrate surface after development, samples are further cleaned by a descuming process in which the sample is momentarily placed in a low pressure oxygen plasma.

With the substrate wafer partially unmasked by development, the mask and substrate is coated with an aluminum thin film. Samples achieve the lowest microwave losses by stripping the silicon of its native oxide surface by submerging the sample in hydrofluoric acid immediately prior to the deposition step. Samples are held in ultra-high vacuum for an overnight duration prior to aluminum deposition. Josephson junctions are created in two aluminum deposition steps; after an initial deposition, we perform a controlled oxidation, in situ, before a final oxidation.

After deposition, a lift-off is performed by submerging the sample in a heated solvent solution. This removes the aluminum coated lithography mask while leaving behind the aluminum deposited directly on the silicon substrate. The solvent polymer swells, causing the resist to lose adhesion to the silicon substrate while it dissolves into the solvent. The mask lifts off the substrate, along with its unwanted aluminum coating. After the resist removal, the sample is rinsed and dried.

Josephson tunnel junctions

While the transmon shunting capacitance is defined from a lithography pattern, the Josephson junction element of the circuit is created by a well-defined insulating barrier separating the two aluminum films at a point of contact. Fabrication of a tunnel junction requires directionally selective aluminum deposition, which is made possible by particular lithographic mask features, such as the Niemeyer-Dolan bridge [113, 114]. Thin film deposition on a narrow bridge feature suspended above the substrate creates an area without metallic film, where the bridge "casts a shadow" on the substrate below (Fig. 3.1a). This shadowing technique is used to create galvanically separate thin films by performing two depositions, each with the substrate surfaces oriented at different angles relative to the evaporator source. Between the angled depositions, an insulating tunnel barrier is created by oxidation of the initial aluminum layer, with a controlled time and pressure (Fig. 3.1b).

The Josephson tunneling energy is determined by the thickness and area of the tunnel junction oxide barrier. For aluminum superconductors, an aluminum oxide barrier thickness of approximately 1 nm and a junction overlap area of 0.1 μm^2 defines a Josephson

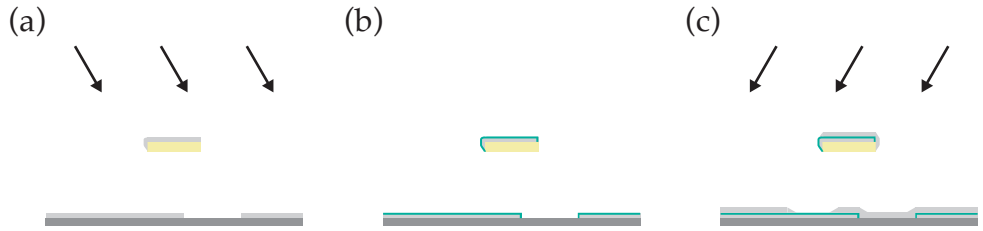

Figure 3.1: The Niemeyer-Dolan bridge technique for junction fabrication begins with a bridge of resist (yellow) suspended over the sample substrate (dark gray). (a) A thin film of aluminum (light gray) is deposited on the sample with a highly directional evaporation. The presence of a resist bridge creates a "shadow" where the substrate is not metalized (b) An oxide layer (teal) is formed by a controlled oxidation of the deposited aluminum. (c) A second directional evaporation of aluminum, at a different angle than the first, results in a small Al-AlO_x-Al junction. The large continuous regions of aluminum on oxide form high critical current Josephson junctions which contribute negligibly to the Josephson tunneling energy.

energy of $E_J/h = 20\,\mathrm{GHz}$. The junction geometry contributes an additional capacitance of $45\,\mathrm{fF}/\mu\mathrm{m}^2$ between the superconductors [109]. The Josephson tunneling energy can be inferred from a measurement of the junction conductance at room temperature. The Josephson energy is calculated from the Ambegaokar-Baratoff formula [115],

$$E_J = \frac{\Delta_{\mathrm{gap}}}{4}\frac{G_N}{G_0} \tag{3.1.1}$$

where Δ_{gap} is the superconducting energy gap, $G_0 = 2e^2/h$ is the conductance quantum, and $G_N = 1/R_N$ is the normal state junction conductance (inverse of the series resistance).

3.1.2 Sample packaging

3D transmon

In the setup of the experiments discussed in later chapters, the transmon circuits were placed into the experiment setup by placement in a three-dimensional waveguide cavity [116]. The cavity primarily provides a method to measurement the quantum states of the transmon circuit. Additionally, the cavity encloses the circuit, thereby shielding it from surrounding electromagnetic blackbody radiation. While transmon circuits can be integrated in a planar device with lithographically defined resonators, the large mode volume of a three-dimensional cavity is advantageous, since the mode has an overall weaker electric field density and thereby has comparatively less microwave loss. The cavity is machined from two blocks of high purity aluminum, or oxygen free high purity copper, with dimensions chosen for a fundamental resonance frequency above the qubit transition frequency.

Microwave launches

Microwave circuit devices, such as planar resonators and Josephson parameter amplifiers, are "launched" by a connection to the rest of the measurement setup. A microwave launch secures and thermalizes a silicon substrate device while providing a transmission line connection to a 50-Ω coax geometry. The silicon substrate is fastened to the dielectric material (Rogers TMM6) of the launch using a small amount of GE Varnish epoxy. The microwave launch has a coaxial connector which transfers to a coplanar waveguide (CPW) transmission line geometry. The CPW connects to the silicon substrate circuit through multiple

wirebonds which are connected to a bondpad on the circuit.

3.2 Cryostat setup

The observation of coherent quantum effects at microwave frequencies requires a thermal background reduced to the scale milliKelvin temperatures. The experiments discussed in the forthcoming chapters were performed in a cryogen-free dilution refrigerator. The dilution cryostat has a pulse tube cryocooler which cools the apparatus to about 3.5 K. A mixture of helium isotopes, ^{3}He and ^{4}He, are then precooled and condensed in the mixing chamber of the dilution refrigerator. The phase separation and mixing of ^{3}He into ^{4}He provides a cooling effect on the surrounding cryostat. Importantly, the dilution refrigerator maintains cooling power at temperatures approaching absolute zero due to the persistent and appreciable solubility of ^{3}He in ^{4}He [117].

Sample holder

Superconducting microwave devices at milliKelvin temperatures must be shielded from thermal radiation and shielded from stray magnetic fields. The transmon circuit cavity, contains a transmon circuit, is placed in an oxygen free high purity (OFHC) sample holder, attached to an enclosure cap mounted on the dilution refrigerator mixing chamber. The copper sample holder has feedthrough ports for microwave signal line and connections for a DC flux bias solenoid. The sample holder enclosure is made light-tight by placing an indium gasket in the seam between the sample holder shell and its cap. The indium is squished by tightening the machine screws that hold the sample holder shell and cap

together.

Samples are further shielded from stray magnetic field from two additional metal cans enclosed around the sample holder. First, an aluminum can is placed over the sample holder, which traps a static magnetic field by the Meissner effect, upon transitioning to superconducting at $\sim 1.2\,\mathrm{K}$. A second can, formed of Cryoperm alloy, is placed around the aluminum can. The alloy is highly diamagnetic at low temperatures, thereby canceling static magnetic fields, i.e. earth's field, within its enclosed volume. Since the Cryoperm is diamagnetic above the superconducting transition temperature of aluminum, this can cancel magnetic fields which are then "locked into place" by the aluminum superconductor.

Thermalization and filtering

All experiment components at milliKelvin temperatures are thermalized to the cryostat mixing chamber plate. These components include sample enclosures, circulators, attenuators, and filters. Components are thermally linked to the gold plated mixing chamber plate of the cryostat with oxygen free high purity copper (OFHC) mounting fixtures and wires, which has appreciable thermal conductivity at cryogenic temperatures [118]. Experiment sample enclosures are attached to the cryostat with oxygen free high purity copper (OFHC) mounting fixtures, which provide thermal continuity with the gold plated mixing chamber plate cooled by the dilution refrigerator.

Coaxial cable transmission lines are thermalized at each temperature stage as they lead room temperature microwave signals to the milliKelvin stage of the cryostat. Input sig-

nal coaxial cables are attenuated by approximately 60 dB before milliKelvin microwave components in order to mitigate thermal noise. Microwave thermal noise originates effectively as blackbody radiation from finite temperature materials with nonzero emissivity. A blackbody radiator that is an electrical component of admittance $Y(\omega)$ and at an equilibrium temperature T, has the power spectral density of current fluctuations [119]

$$S_{II}(\omega) = 4k_{\mathrm{B}}T\frac{\hbar\omega/k_{\mathrm{B}}T}{e^{\hbar\omega/k_{\mathrm{B}}T}-1}\,\mathrm{Re}\{Y(\omega)\}. \tag{3.2.1}$$

For thermal noise originating at room temperature, we consider Equation 3.2.1 in the high temperature or low frequency limit, recovering the Johnson-Nyquist noise formula [120],

$$S_{II}(\omega) \simeq 4k_{\mathrm{B}}T\,\mathrm{Re}\{Y(\omega)\}. \tag{3.2.2}$$

From Equation 3.2.2, infer the power spectral density of room temperature thermal fluctuations are 10^4 times larger than the power spectral density of quantum fluctuations $\sim \hbar\omega/2$ at 5 GHz microwave frequencies. As the thermal noise is linear in temperature, this implies at least 40 dB of the room temperature thermal noise should be dissipated into a zero temperature bath. Cryostat attenuators, however, are not zero temperature thermal baths. Consequently, attenuators of each temperature stage also emit thermal noise. Accounting for this in the cryostat attenuator, along with the cooling power at each temperature stage, we use an attenuator stack listed in Table 3.1.

Microwave signals for device measurements propagate in the TEM mode of coaxial transmission lines. While a signal of any wavelength can propagate in the TEM mode,

Stage	Temperature (K)	Cooling power (mW)	Attenuation
—	300 K	—	0 dB
—	50 K	1000	0 dB
—	4 K	100–300	20 dB
Still	1 K	25	10 dB
Cold plate	0.25 K	—	0 dB
Mixing chamber	0.01 K	0.25	30 dB

Table 3.1: Cryostat temperature stages are outfitted with inline coaxial attenuators to reduce thermal noise leading to mixing chamber microwave components. A 0 dB attenuator is a 50-Ω component which serves to thermalize the coaxial center pin without attenuating the signal.

signals of a wavelength comparable or smaller than the total coaxial diameter can also propagate in other mode geometries (e.g., the TE_{11} mode) [121]. The coaxial cable dielectric and conductive losses are not sufficient to filter high frequency (THz) thermal noise. For this reason, each RF measurement line connected to the mixing chamber is interrupted with a high frequency absorptive filter.

An absorptive filter is constructed as a short 50-Ω transmission line section which has significantly large dielectric loss at high frequencies ($> 25\,\text{GHz}$). The filter is made of OFHC package with stripline geometry (Fig. 3.2a), which is then potted with Eccosorb CR-110 epoxy (Fig. 3.2b). In Figure 3.2c, the reflection scattering parameter (S11) indicates only a small fraction of is reflected from the filter, since the filter impedance is well-matched to the 50-Ω characteristic impedance of the vector network analyzer (VNA). The scattering parameter for transmission (S21), indicates that the filter attenuation scales with frequency. For output measurement lines, an absorptive filter is located between milliKelvin microwave components and higher temperature microwave devices, such as amplifiers. Since signals are attenuated before significant amplification, it is desirable to have a neg-

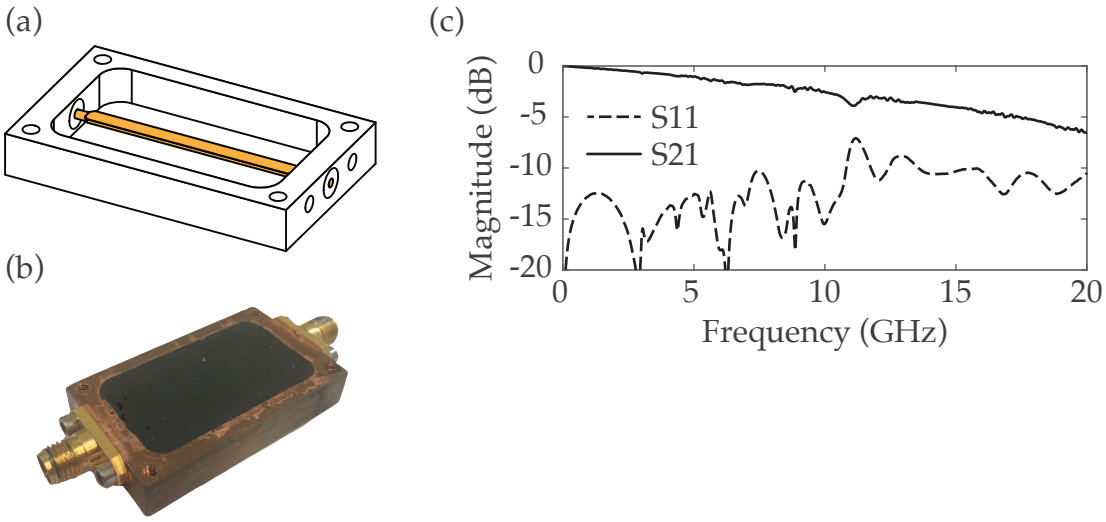

Figure 3.2: (a) A design model of a high frequency absorptive filter with stripline geometry. (b) The dielectric material of the stripline geometry is an absorptive epoxy. (c) A transmission measurement shows the filter attenuates high frequency signals. At lower frequencies for experiment signal detection, the filter transmission (S21) shows modestly little attenuation (-2 dB at 5 GHz).

ligible amount of attenuation at lower frequencies, since filter loss is indiscriminate to the signals we would like to detect.

3.3 Amplification

The microwave circuits and resonators at milliKelvin temperatures have a thermal excitation background equivalent to less than a single microwave photon per 1 MHz bandwidth. These devices are also driven and measured with microwave drives with similarly low microwave powers. Signal detection of these microwave signals requires amplification above the thermal noise background at room temperature. However, the process of signal amplification invariably contributes noise to the microwave signal. The power of this added noise is characterized by a thermal noise temperature at the input of an amplifier. The Friis

formula describes the scaling of the system noise temperature for a cascade of amplifiers, each with a specified gain factor and noise temperature [122],

$$T_{\text{sys}} = T_0 + \frac{T_1}{G_0} + \frac{T_2}{G_0 G_1} + \ldots + \frac{T_k}{G_1 G_2 \cdots G_{k-1}}, \tag{3.3.1}$$

where G_k and T_k are the linear gain factor and noise temperature for the k^{th} amplifier. Note that the gain factor can also describe signal attenuation when $G < 1$ which causes a signal to noise decrease since the attenuated signal is "replaced" by Johnson noise at the physical temperature of the attenuating element. The Friis formula shows us that a given amount of signal gain can improve the signal to noise ratio more significantly at low noise temperature stages. In the absence of gain, noise power contributed from a small amount of attenuation at a high temperatures is equivalent to a large amount of attenuation at low temperatures. This proportional trade-off can be offset by including gain in the amplification chain before any attenuation at higher temperatures. Since the effective noise temperature of an amplifier is typically consistent with the amplifier physical temperature, it is always advantageous to include amplification at lower temperature stages.

In the experiment setup, amplification is performed with a low noise commercial the high electron mobility transistor (HEMT) amplifier. The amplifier is attached and thermalized to the cryostat 4 K stage, which is itself thermalized to the pulse tube cryocooler. A superconducting niobium coaxial cable connects milliKelvin experiment devices to the input port of the HEMT amplifier. The superconducting cable contributes little signal loss while also thermally isolating milliKelvin microwave components from the relatively

warmer stages HEMT amplifier and 4 K cryostat stage. In addition, the HEMT electrical noise is isolated from circuits and resonators at milliKelvin temperature by placing two ferrite-core isolators between the last milliKelvin microwave component and the superconducting cable leading to the HEMT. The isolators are thermalized to the mixing chamber stage of the cryostat.

3.3.1 The Josephson parametric amplifier

The noise contribution of a HEMT amplifier limits our ability to make microwave measurements at the single photon limit. While, in principle, enough signal averaging can overcome a noise background, this method is insufficient for single-shot readout of quantum states on a microsecond time scale. We address this issue by implementing a preamplification stage at milliKelvin temperatures. A Josephson parametric amplifier (JPA) performs near-quantum-limited signal amplification as a nonlinear single mode circuit operated as a semiclassical quantum device. A JPA reliably produces signal gain of about 20 dB with 50 MHz instantaneous bandwidth, sufficient for single shot quantum state readout. Importantly, a JPA amplifier can achieve a noise temperature of about 300 mK, which can decrease the overall measurement noise temperature by an order of magnitude.

Amplification from a nonlinear circuit

We approach the operation of a JPA from a lumped element model. The nonlinear circuit model contains a Josephson junction of critical current I_c, and effective inductance $L = \varphi_0 / I_c$, along with a shunting capacitor C, which are connected to a current source

$I(t)$ of characteristic impedance Z_0. By applying Kirchhoff's law to currents in the circuit branches and expressing the current degree of freedom in terms of magnetic flux $\Phi(t)$, we find the equation of motion

$$C\ddot{\Phi}(t) + Y_0\dot{\Phi}(t) + \frac{\varphi_0}{L}\sin\delta(t) = I(t) \tag{3.3.2}$$

where $\delta(t)$ is the gauge-invariant superconducting phase difference across the Josephson junction. We express the magnetic flux in terms of the superconducting phase by the relation $\Phi = \varphi_0\delta$, divide by the reduced magnetic flux quantum, and multiply by the inductance

$$\frac{1}{\omega_p^2}\ddot{\delta}(t) + \frac{\gamma}{\omega_p^2}\dot{\delta}(t) + \sin\delta(t) = \frac{1}{I_c}I(t). \tag{3.3.3}$$

where $\omega_p = 1/\sqrt{LC}$ is the oscillator plasma frequency and $\gamma = 1/Z_0C$ is the oscillator damping rate. Equation 3.3.3 is known as the Resistively and Capacitively Shunted Junction (RCSJ) equation and is analogous to a driven damped pendulum in a constant gravitation field [123, 124]. The oscillator is damped as a result of the current source finite admittance, together with the circuit capacitance, which limits the flux amplitude to small values for relatively weak driving.

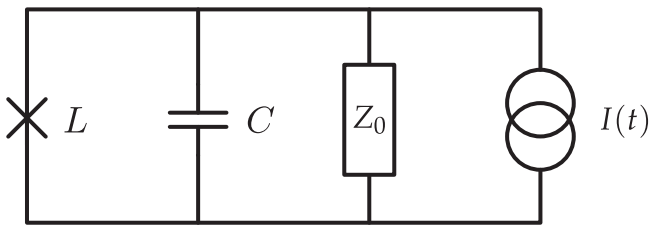

Figure 3.3: The JPA is modeled as a lumped element circuit connected to a current source.

We consider a single-frequency sinusoidal current source (up to a phase) and expand the sinusoidal term of Equation 3.3.2 up to third order

$$\frac{1}{\omega_p^2}\ddot{\delta}(t) + \frac{\gamma}{\omega_p^2}\dot{\delta}(t) + \delta(t) - \frac{1}{6}\delta(t)^3 = \frac{I_d}{I_c}\cos\omega_d t \tag{3.3.4}$$

which is a non-linear second-order differential equation describing a Duffing oscillator. Apart from the nonlinear cubic term, the equation of motion (Eq. 3.3.4) has a harmonic oscillator-like resonance at the plasma frequency in the weak driving limit. Finite amplitude perturbations effectively increase the circuit inductance by way of the nonlinear cubic term, thereby depressing the oscillator resonance. The steady state response, in terms of amplitude and phase, can be found using the method of harmonic balance, by which the oscillator response takes the form

$$\delta(t) = \delta_0 e^{i\phi} = \delta_{||}\cos\omega_d t + \delta_{\perp}\sin\omega_d t. \tag{3.3.5}$$

We insert this ansatz into Equation 3.3.4 and arrive at the following coupled equations by removing fast oscillating terms,

$$\begin{aligned} \delta_{||} - 2\delta_{\perp}Q\left(\frac{\omega_d}{\omega_p} + \frac{\delta_0^2}{16} - 1\right) &= 0 \\ \delta_{\perp} - 2\delta_{||}Q\left(\frac{\omega_d}{\omega_p} + \frac{\delta_0^2}{16} - 1\right) &= Q\frac{I_d}{I_c}. \end{aligned} \tag{3.3.6}$$

where $Q = \omega_p/\gamma$ is the coupled quality factor of the oscillator. For certain parameter regimes, the phase response of the oscillator has a sharp dependence on the drive fre-

quency (Figure 3.4). This is an underlying mechanism for amplification with a nonlinear oscillator; a strong drive biases the oscillator to a regime where a small signal perturbation can dramatically shift the oscillator phase, and the phase shift of the strong drive itself.

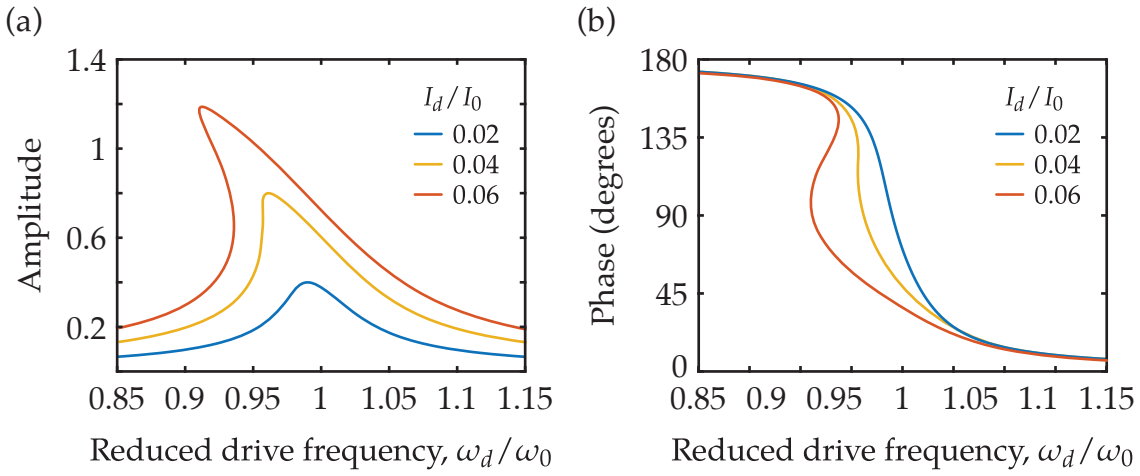

Figure 3.4: The steady state amplitude and phase response of the JPA is solved by the method of harmonic balance with $Q = 20$ for the coupled quality factor. For strong drives the oscillator is driven in a bifurcation regime, where the steady state response has multiple solutions. (a) The peak of the amplitude response shifts to lower frequencies for increasing drive strengths. (b) The phase response of the JPA "stiffens" as the drive current increases, before having multiple solutions in the bifurcation regime.

A Josephson parametric amplifier device

Here, we consider an amplifier device fabricated from a single step lift-off process (Section 3.1), as aluminum on silicon circuits. The JPA is designed as a lumped element resonator illustrated in the schematic of Figure 3.5. The Josephson junction element, of effective inductance L_J, is a single DC Superconducting QUantum Interference Device (SQUID) for circuit tunability. The device is designed with two interdigitated capacitors create the resonator capacitance C_R to ground. Another interdigitated structure is used for a coupling capacitance C_C to the amplifier port of characteristic impedance Z_0. The coupling

capacitance determines the coupled quality factor of the resonator by determining the overall conductance to ground. Each lumped component was modeled in Ansys AWR Microwave Office as a planar geometry (Fig. 3.6a). Once simulating and optimizing the electromagnetic response for each component separately, the resonator was modeled as a whole assembled structure. The resonator parameters were determined while treating the Josephson junction element as a linear inductor.

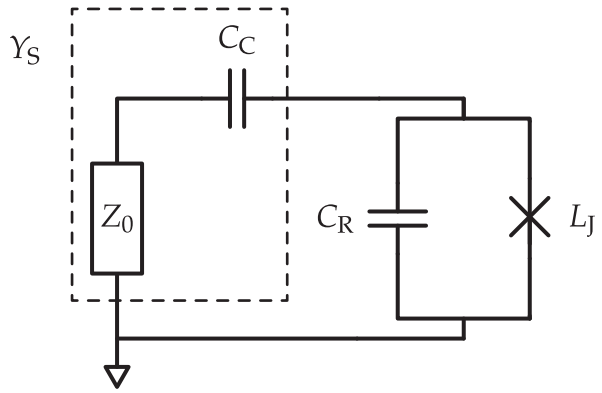

Figure 3.5: A schematic model of the Josephson parametric amplifier capacitively coupled to a Z_0 characteristic impedance. The coupled quality factor of the nonlinear oscillator mode depends on the shunting admittance Y_S.

We now consider certain requirements for JPA operation and fabrication design constraints. The JPA resonance must be in the frequency range 4–8 GHz, at readout resonator frequencies, and have an instantaneous bandwidth of about 50 MHz, for amplification of signal transients on a reasonably short time scale (Fig. 3.6b).

Additionally, the circuit nonlinearity must be sufficiently strong to cause signal amplification while the strength of the drive current is well below the Josephson junction critical current. We address this requirement in terms of the participation ratio $p = L_J/L_\Sigma$, where L_Σ is the total shunting inductance embedded in the circuit. The participation ratio

measures the relative strength of the nonlinear inductance. To meet the operating regime convenient for amplification, we desire the relation $pQ \gg 1$, that is, the product of the coupled quality factor and participation ratio is much greater than unity [125]. Given these considerations, the JPA was design to have a quality factor of approximately $Q \simeq 20$.

The schematic model (Fig. 3.5) was used to calculate an expected oscillator resonance and quality factor. These circuit parameters were then adjusted given circuit parameters and physical constraints given by the dielectric constant of the silicon substrate, the resolution of optical lithography, and the attainable values of Josephson junction critical current density. The circuit frequency of resonance and quality factor were calculated from the total circuit admittance. We define the shunting impedance as $Z_S(\omega) = 1/Y_S(\omega) = Z_0 + 1/j\omega C_C$ and the total admittance is

$$\begin{aligned} Y(\omega) &= j\omega C_R + \frac{1}{j\omega L_J} + Y_S(\omega) \\ &= j\omega C_R + \frac{1}{j\omega L_J} + \frac{j\omega C_C}{1 + j\omega Z_0 C_C}. \end{aligned} \tag{3.3.7}$$

We solve for the oscillator resonance by calculating the zeros of the total admittance. The oscillator quality factor is then evaluated as

$$Q = \frac{\omega_0 C}{\mathrm{Re}\{Y(\omega_0)\}} \tag{3.3.8}$$

where ω_0 is the oscillator resonance frequency and $C = \frac{1}{2}\,\mathrm{Im}\{Y'(\omega)\}|_{\omega=\omega_0}$ is the effective capacitance C at the resonance frequency, evaluated from the slope of the admittance.

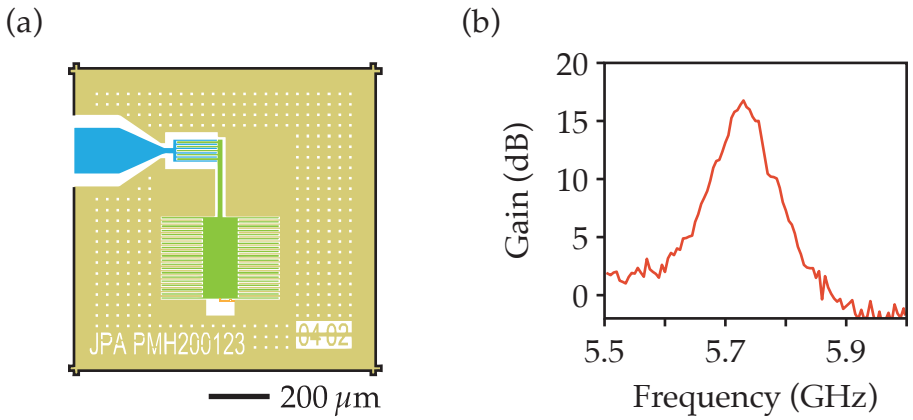

Figure 3.6: (a) The JPA design layout has electromagnetic structures for the wirebond pad and coupling capacitor (blue), the resonator shunting capacitor (green), a SQUID Josephson junction (red), and a perforated ground plane (brown). (b) When the JPA is driven by a pump tone, its response to a weak signal displays approximately 17 dB of gain with 40 MHz instantaneous bandwidth. The gain is normalized by the device weak signal response when it is not driving by pump tone.

Chapter 4

Open Quantum Systems

4.1 A quantum system with its environment

All quantum systems interact with an environment. When a quantum system interacts with many environment degrees of freedom that often cannot be measured or controlled, system dynamics display dissipation and dephasing. Unitary dynamics of the system alone cannot describe decoherence, instead, this dynamics emerges from the joint unitary dynamics of the system and environment. We typically develop an effective description of the quantum system in terms of a master equation by averaging over all possible, yet unknown, states of the environment. In all circumstances, the dynamics of an open quantum system are conditioned on the properties of its environment. Notably, measurements on the environment provide information of the system state. When we are informed by the outcomes of environment measurements, a conditional evolution of the quantum system describes the dynamics of quantum measurement, known as *measurement backaction* [126].

4.1.1 The reduced dynamics of the system

Any complete description of a quantum system provides the expectation value of an observable, which is the average over a distribution of all possible system states. Since we wish to evaluate expectation values for a quantum system conditioned on unknown states of its environment, we use a density operator formalism which can account for both quantum and classical uncertainty. The density operator is self-adjoint, positive semidefinite, and of unit trace [127].

We use a quantum mechanical description for the degrees of freedom of both the system and its environment. Without providing microscopic details of the environment, we will assume it has many degrees of freedom, for which we call it a *reservoir*. States of the system are defined in the Hilbert space $\mathcal{H}_S$ which are distinct from reservoir states, defined in another Hilbert space $\mathcal{H}_R$. A composite state of the system and reservoir together is defined in a tensor product space: $\mathcal{H}_S \otimes \mathcal{H}_R$ [128]. Given a density operator of the system and reservoir χ, we calculate the reduced density operator of the system as,

$$\rho = \mathrm{tr}_R(\chi), \tag{4.1.1}$$

where $\mathrm{tr}_R(\,\cdot\,)$ is the partial trace over the reservoir state space. The partial trace is defined operationally from the trace procedure

$$\langle A \rangle_\rho \equiv \mathrm{tr}\big((A \otimes \mathbb{1}_R)\chi\big), \tag{4.1.2}$$

where A is an operator acting in $\mathcal{H}_S$, the Hilbert space of the system. The dynamics of

the system and reservoir together is given by a time reversible, unitary transformation. In contrast, the reduced dynamics of the system is

$$\rho(t) = \mathrm{tr}_{\mathrm{R}}\big(\chi(t)\big) = \mathrm{tr}_{\mathrm{R}}\big(U(t)\chi(0)U(t)^{\dagger}\big) \tag{4.1.3}$$

which is an irreversible dynamics in general.

4.1.2 Interaction dynamics of a system and reservoir

The interacting system and reservoir together have the Hamiltonian,

$$H = \underbrace{H_{\mathrm{S}} \otimes \mathbb{1}_{\mathrm{R}} + \mathbb{1}_{\mathrm{S}} \otimes H_{\mathrm{R}}}_{H_0} + V, \tag{4.1.4}$$

where H_{S} and H_{R} are each the Hamiltonian for the system and reservoir alone, and V is the system-reservoir interaction Hamiltonian. We move from the laboratory frame of Equation 4.1.4 to the interaction frame of the system and reservoir by defining $\chi(t) = e^{-iH_0t}\chi e^{+iH_0t}$ as the interaction frame density operator and $V(t) = e^{-iH_0t}Ve^{+iH_0t}$ as the time-dependent interaction frame Hamiltonian. In the Schrödinger picture, time evolution of the system and reservoir is

$$\dot{\chi}(t) = -i[V(t), \chi(t)]. \tag{4.1.5}$$

We substitute the integral of Equation 4.1.5 back into itself and find

$$\dot{\chi}(t) = -i[V(t), \chi(0)] - \int_0^t ds\, [V(t), [V(s), \chi(s)]], \tag{4.1.6}$$

where $\chi(0)$ is the initial state of the density operator. We can solve for an effective time evolution of the system by tracing over the reservoir state space,

$$\dot{\rho}(t) = -\int_0^t ds\, \mathrm{tr}_\mathrm{R}\big([V(t), [V(s), \chi(s)]]\big), \tag{4.1.7}$$

and we have chosen $\mathrm{tr}_\mathrm{R}\big([V(t), \chi(0)]\big) = 0$ by a convenient choice of the interaction Hamiltonian. While Equation 4.1.7 is an exact equation for the reduced dynamics of the system, a solution is generally intractable. However, we can solve for the system dynamics under certain conditions and assumptions which approximate the integrand of Equation 4.1.7.

Separable initial state First, we assume the initial density operator state is a separable state. This is a reasonable assumption given the system and reservoir are weakly interacting [129]. The density operator initial state is then

$$\chi(0) = \rho(0) \otimes \varrho(0), \tag{4.1.8}$$

where $\varrho(0)$ is the initial reduced density operator of the reservoir.

- Condition: no initial correlations between system and reservoir, weak coupling
- Assumption: $\chi(0) \approx \rho(0) \otimes \varrho(0)$

Born approximation (1) The density operator dynamics can be expressed as a perturbative expansion in time,

$$\chi(t) = \rho(0) \otimes \varrho(0) + \mathcal{O}(V). \tag{4.1.9}$$

Given the modulus of V is small, the state $\chi(t)$ will only deviate negligibly from a correlated state during the evolution [130]. We can approximate the density operator in the integrand of Equation 4.1.7 by neglecting terms higher than second order in V to solve for the reduced dynamics of the system.

- Condition: weak coupling
- Assumption: $\chi(t) = \rho(t) \otimes \varrho(t)$ in the integrand of Equation 4.1.7.

Born approximation (2) We assume a weak interaction between the system and reservoir, such that the reservoir state is negligibly affected by the system, which in turn, allows the system dynamics to be well approximated by an interaction with an unperturbed reservoir state.

- Condition: weak coupling, large reservoir
- Assumption: $\varrho(t) = \varrho$ in the integrand of Equation 4.1.7, where ϱ is the reduced density operator of the reservoir at all times.

Markov approximation (1) We assume the system is "small" compared to the "large" environment reservoir. Furthermore, the system weakly interacts with many eigenstates of the reservoir, all which form a continuous energy spectrum. The reservoir spectrum

must be continuous relative to the sharpness of all the system eigenstates. Consequently, the system dynamics cannot be significantly affected by its own effect on the reservoir, i.e. there is no "flow of information" from the reservoir back to the system [128]. We make the approximation that contributions to the integral in Equation 4.1.7 are significant only when $\rho(s) = \rho(t)$.

- Condition: weak coupling to many reservoir eigenstates that form a continuous spectrum
- Assumption: replace $\rho(s)$ by $\rho(t)$ in the integrand

Markov approximation (2) If the system state does not change appreciably on the time scale of decay for reservoir correlations, then contributions to the integrand of Equation 4.1.7 are negligible for times in the long past. Here the time scale for system dynamics is coarse-grained relative to the fast dynamics of the reservoir. We approximate the integral of Equation 4.1.7 by extending the lower limit to negative infinity. From this approximation, the effect of the reservoir on the system dynamics is independent of time.

- Condition: weak coupling, large environment, a continuum of reservoir eigenstates, coarse-grained time evolution
- Assumption: we extend the lower limit of integration in Equation 4.1.7 to an infinite time in the past.

The approximations above are all together called the *Born-Markov approximation*, which

leads to the Markovian quantum master equation [128],

$$\dot{\rho}(t) = -\int_0^\infty ds\, \mathrm{tr}_\mathrm{R}\big([V(t),[V(t-s),\rho(t)\otimes\varrho]]\big), \tag{4.1.10}$$

where we have substituted s with $t-s$ for the integration variable.

We continue to solve for the time evolution of the system by considering an interaction Hamiltonian $V = \sum_\alpha A_\alpha \otimes B_\alpha$ in the laboratory frame. Since we are interested in the time evolution of transitions between system states, we decompose the system interaction operators A_α in terms of transitions between the system energy eigenstates,

$$A_\alpha = \sum_\omega A_{\alpha,\omega} = \sum_\omega \sum_{\epsilon'-\epsilon=\omega} |\epsilon\rangle\langle\epsilon|A_\alpha|\epsilon'\rangle\langle\epsilon'|, \tag{4.1.11}$$

where the second sum is over all transitions for the constant eigenvalue difference $\epsilon' - \epsilon = \omega$ for each ω of the first sum [131]. From Equation 4.1.11 we can find the relation $A^\dagger_{\alpha,\omega} = A_{\alpha,-\omega}$. It follows that the interaction Hamiltonian in the interaction frame is

$$V(t) = \sum_{\alpha,\omega} e^{-i\omega t} A_{\alpha,\omega} \otimes B_\alpha(t) \tag{4.1.12}$$

and

$$\begin{aligned} V(t) &= \sum_{\alpha,\omega} e^{+i\omega t} A_{\alpha,-\omega} \otimes B_\alpha(t) \\ &= \sum_{\alpha,\omega} e^{+i\omega t} A^\dagger_{\alpha,\omega} \otimes B^\dagger_\alpha(t), \end{aligned} \tag{4.1.13}$$

where $B_\alpha(t)$ are the interaction Hamiltonian operators of the reservoir in the interaction

frame.

Inserting the interaction Hamiltonian (Eq. 4.1.12) into the master equation (Eq. 4.1.10) yields

$$\begin{aligned}\dot{\rho}(t) = -\int_0^\infty ds \sum_{\alpha,\beta}\sum_{\omega,\omega'} e^{i(\omega'-\omega)t}e^{-i\omega s}\,\mathrm{tr}_\mathrm{R}\big(\\ A^\dagger_{\alpha,\omega}A_{\beta,\omega'}\rho(t)\otimes B_\alpha(t)^\dagger B_\beta(t-s)\varrho\\ - A_{\beta,\omega'}\rho(t)A^\dagger_{\alpha,\omega}\otimes B_\beta(t-s)\varrho B^\dagger_\alpha(t) + \mathrm{h.c.}\big)\end{aligned} \tag{4.1.14}$$

Rotating wave approximation If the system eigenstates are close in energy relative to the interaction strength with the reservoir, then oscillating terms of Equation 4.1.14 do not contribute to the system dynamics during the time scale of system relaxation.

- Condition: weak coupling relative to system dynamics
- Assumption: Neglect the rapidly oscillating non-secular terms in Equation 4.1.14

We apply the rotating wave approximation to Equation 4.1.14 and integrate the partial trace over the reservoir state space to find

$$\dot{\rho}(t) = \sum_{\alpha,\beta}\sum_{\omega}\Gamma_{\alpha,\beta}(\omega)\big(A_{\beta,\omega}\rho(t)A^\dagger_{\alpha,\omega} - A^\dagger_{\alpha,\omega}A_{\beta,\omega}\rho(t)\big) + \mathrm{h.c.}, \tag{4.1.15}$$

where we define one-sided Fourier integrals of the reservoir correlation functions as

$$\Gamma_{\alpha,\beta}(\omega) = \int_0^\infty ds\, e^{i\omega s}\langle B^\dagger_\alpha(t)B_\beta(t-s)\rangle. \tag{4.1.16}$$

By collecting real and imaginary terms of Equation 4.1.16 and rearranging indices, we

rewrite the master equation in the form

$$\begin{aligned}\dot{\rho}(t) = &-i[H_{\mathrm{LS}}, \rho(t)] \\ &+ \sum_{\alpha,\beta}\sum_{\omega} \gamma_{\alpha,\beta}(\omega)\big(A_{\beta,\omega}\rho(t)A^{\dagger}_{\alpha,\omega} - \frac{1}{2}\{A^{\dagger}_{\alpha,\omega}A_{\beta,\omega}, \rho(t)\}\big),\end{aligned} \tag{4.1.17}$$

where we define $\gamma_{\alpha,\beta}(\omega) = \Gamma_{\alpha,\beta} + \Gamma^{*}_{\beta,\alpha}$ and $S_{\alpha,\beta}(\omega) = (\Gamma_{\alpha,\beta} - \Gamma^{*}_{\beta,\alpha})/2i$, and H_{LS} is the Lamb-shift Hamiltonian

$$H_{\mathrm{LS}} = \sum_{\alpha,\beta}\sum_{\omega} S_{\alpha,\beta}(\omega)A^{\dagger}_{\alpha,\omega}A_{\beta,\omega}. \tag{4.1.18}$$

We arrive at the master equation in Lindblad form by diagonalizing the matrix of coefficients $\sum_{\omega} \gamma_{\alpha,\beta}(\omega)$ and transforming the interaction operators accordingly,

$$\dot{\rho}(t) = -i[H_{\mathrm{LS}}, \rho(t)] + \sum_{k} \gamma_k \mathcal{D}[L_k], \tag{4.1.19}$$

where L_k are Lindblad jump operators and $\mathcal{D}[A]\rho = (2A\rho A^{\dagger} - \{A^{\dagger}A, \rho\})/2$ is the dissipation superoperator.

4.2 Quantum measurement theory

4.2.1 Measurement update

In the previous section, we solved for the dynamics of the system interacting with an environment. To explore the dynamics of quantum measurement, we consider the reversible

dynamics of the system and reservoir

$$\chi(t) = U\chi(0)U^{\dagger}, \tag{4.2.1}$$

where $\chi(0)$ is the initial system-environment state and U_t is the unitary time evolution operator for the system and environment together. After unitary time evolution, a partial trace over the environment state space gives the time evolved state of the system, which is a map for the system state:

$$\rho(0) \to \rho(t). \tag{4.2.2}$$

For a given duration of time evolution, we can calculate the reduced density operator of the system as

$$\rho(t) = \mathrm{tr}_{\mathrm{R}}\big(\chi(t)\big) = \sum_{m} \langle \phi_m | \, U\chi(0)U^{\dagger} \, | \phi_m \rangle \,, \tag{4.2.3}$$

where $\chi(0)$ is the initial state and we have chosen orthonormal bases $|\psi_i\rangle$ and $|\phi_k\rangle$ for the system and environment respectively. Since we sum projections over an orthonormal basis of the environment (Eq. 4.2.3), the reduced density operator of the system is, in general, not a pure state [132].

The time evolution operator acts in tensor product space as [133],

$$\begin{aligned} U &= \sum_{ijk\ell} u_{ijk\ell} |\psi_i\rangle\langle\psi_j| \otimes |\phi_k\rangle\langle\phi_\ell| \\ &= \sum_{k\ell} \underbrace{\left(\sum_{ij} u_{ijk\ell} |\psi_i\rangle\langle\psi_j| \right)}_{A_{k\ell}} \otimes |\phi_k\rangle\langle\phi_\ell| \\ &= \sum_{k\ell} A_{k\ell} \otimes |\phi_k\rangle\langle\phi_\ell|. \end{aligned} \tag{4.2.4}$$

We choose an initial state $\chi(0) = \rho(0) \otimes |\phi_0\rangle\langle\phi_0|$ and use Equation 4.2.4 to express each summation term contributing to the time evolved density operator of the system (Eq. 4.2.3),

$$\begin{aligned} \langle\phi_m| U\chi(0)U^\dagger |\phi_m\rangle &= \langle\phi_m| U\big(\rho(0) \otimes |\phi_0\rangle\langle\phi_0|\big)U^\dagger |\phi_m\rangle \\ &= A_{m0}\rho(0)A_{0m}^\dagger \otimes \mathbb{1}. \end{aligned} \tag{4.2.5}$$

Therefore the reduced density operator for the system, Equation 4.2.3, can be evaluated as

$$\rho(t) = \sum_m A_m \rho(0) A_m^\dagger \tag{4.2.6}$$

where we assume the initial environment state use the notation A_m for A_{m0}. In Equation 4.2.6, the sum represents an average of the system state over all the possibilities of projective measurement on the environment state. Note that the reduced dynamics of the system is invariant to the basis environment measurements, since the trace operation is basis independent.

Quantum measurement dynamics results from conditional evolution of the system. If we measure the environment state after a duration of time evolution, the measurement

projects the system-environment state into a known basis state of the environment. After a measurement of the environment state, we infer the environment is projected according to the operator $|\phi_c\rangle\langle\phi_c|$ which corresponds to a specific measurement outcome. The unnormalized system state conditioned on this environment measurement result is proportional to

$$\begin{aligned}\rho(t) &\propto \mathrm{tr}_\mathrm{R}\big(|\phi_c\rangle\langle\phi_c|\chi(t)|\phi_c\rangle\langle\phi_c|\big) \\ &= \langle\phi_c|\, U\chi(0)U^\dagger\, |\phi_c\rangle \\ &= A_c\rho(0)A_c^\dagger,\end{aligned} \tag{4.2.7}$$

where we now refer to the operator A_c as a measurement operator. The conditional density operator is normalized as,

$$\rho(t) = \frac{A_c\rho(0)A_c^\dagger}{\mathrm{tr}\big(A_c^\dagger A_c\rho(0)\big)}. \tag{4.2.8}$$

4.3 Dispersive measurement of quantum bit

The dispersive interaction of a qubit and resonator (Section 2.3) correlates qubit populations with a single quadrature of the resonator field. A Josephson parametric amplifier (Section 3.3) can perform a projective measurement on this field quadrature, in a process of homodyne measurement. As such, homodyne measurement of the resonator field corresponds to indirect measurement of the qubit. The measurement result, or measurement record, provides information of the qubit populations, while the measurement process itself induces measurement backaction dynamics on the qubit state. For dispersive

measurement, the dynamics imparted on the state, and the statistics of the measurement record, are described by the positive operator-valued measure (POVM) [133]

$$M_r = \left(\frac{\delta t}{2\pi\tau}\right)^{1/4} \exp\left[-\frac{\delta t}{4\tau}(r\mathbb{1} - \sigma_z)^2\right] \tag{4.3.1}$$

where the r is measurement strength is the product of the signal integration duration δt and the measurement rate $1/2\tau = 8\chi^2\bar{n}/\kappa$. Referring to Equation 2.3.13, the measurement strength is proportional to the magnitude of correlation between the resonator field quadrature amplitude and the expectation value of qubit populations.

Here, we first consider the statistics of dispersive measurement. The Gaussian form of the dispersive measurement POVM (Eq. 4.3.1) corresponds to the distribution of homodyne measurement results given a coherent state which probes the resonator. For a qubit state with an expectation value $z = \langle\sigma_z\rangle$, the probability density distribution of the measurement records is

$$\begin{aligned} P(r)\,dr &= \mathrm{tr}\left(M_r^\dagger M_r \rho\right) \\ &= \sqrt{\frac{\delta t}{2\pi\tau}}\left(\frac{1+z}{2}e^{-\frac{\delta t}{2\tau}(r-1)^2} + \frac{1-z}{2}e^{-\frac{\delta t}{2\tau}(r+1)^2}\right). \end{aligned} \tag{4.3.2}$$

On short timescale $\delta t \ll \tau$, the measurement record mean is equivalent to the expectation value of the qubit populations. We consider the POVM in the continuous limit and solve for the probability density

$$P(r)\,dr = \sqrt{\frac{\delta t}{2\pi\tau}}e^{-\frac{\delta t}{2\tau}(r-z)^2}. \tag{4.3.3}$$

From Equation 4.3.3 we find measurement results from the homodyne signal at short-

times are a Gaussian stochastic variable which has a mean that is the expectation value of the qubit populations.

We investigate measurement backaction from dispersive measurement in the continuous limit by considering the first-order measurement dynamics in δt [134]. The numerator of the measurement update (Eq. 4.2.8) is

$$\begin{aligned} M_r \rho M_r^\dagger &= \big(\mathbb{1} + \delta t \log\, M_r + \dots\big)\rho\big(\mathbb{1} + \delta t \log\, M_r^\dagger + \dots\big) \\ &\simeq \rho + \zeta, \end{aligned} \tag{4.3.4}$$

where $\zeta = \big(\log\, M_r\big)\rho - \rho\big(\log\, M_r\big)$. The denominator of the measurement update normalizes the density operator by rescaling all terms. Since normalization does not affect measurement dynamics at any order in δt, we treat this approximation separately. Up to first-order in δt, the normalization factor is

$$\big(\mathrm{tr}\big(M_r^\dagger M_r \rho\big)\big)^{-1} \simeq 1 - \mathrm{tr}\big(\zeta\big). \tag{4.3.5}$$

Combining the numerator and denominator, the measurement update on the density operator

$$d\rho = \zeta - \rho \mathrm{tr}\big(\zeta\big). \tag{4.3.6}$$

We rewrite this in terms of coupled first-order nonlinear ordinary differential equations,

$$\begin{aligned} \dot{x} &= -yz\frac{r}{\tau} \\ \dot{y} &= -xz\frac{r}{\tau} \\ \dot{z} &= (1-z^2)\frac{r}{\tau}. \end{aligned} \tag{4.3.7}$$

We recognize that measurement backaction on the qubit populations is independent of the qubit coherences. This is an artifact of the quantum non-demolition property of dispersive measurement; the qubit eigenstates are simultaneous eigenstate with the eigenstates of the measurement operator. Furthermore, the relative strength of the measurement backaction is reduced as the qubit state migrates towards the eigenstates of the measurement operator. A central aspect of dispersive measurement backaction is that the measurement record reinforces the qubit state and vice versa. Since the measurement record is as a Gaussian stochastic variable with a mean $\langle r \rangle \propto z$, changes of the qubit state are correlated to the qubit state itself. Consequently, the long-time dynamics of dispersive measurement behave as projective measurement toward the qubit population eigenstates, in a manner of wavefunction collapse.

Chapter 5

The Statistical Arrow of Time in Quantum Measurement

> *The problem of time in physics and chemistry is closely related to the formulation of the second law of thermodynamics. Therefore another possible title of this lecture could have been: "the macroscopic and microscopic aspects of the second law of thermodynamics."*
>
> — Ilya Prigogine, *Nobel Lecture, December 8th 1977*

In the opening statement of his Nobel lecture *Time, Structure and Fluctuations*, Ilya Prigogine alludes to a thermodynamic arrow of time that arises from reversible microscopic dynamics [135]. The arrow of time is a macroscopic property characterized by the statistical likelihood of reversible physical processes. Continuous quantum measurement is a time reversible physical process which is characteristically statistical in nature, due to the random outcomes of quantum measurements. In this chapter, we quantify a statistical arrow of time for individual measurement trajectories of a superconducting qubit

by comparing the likelihood of forward and backward trajectory time evolution. While measurement dynamics are reversible, trajectory statistics always favor a forward arrow of time for an ensemble of measurement trajectories, a phenomenon analogous to the second law of thermodynamics.

Section 5.1 of this chapter motivates a connection between continuous quantum measurement and stochastic thermodynamics through their shared statistical description. From the statistical description of the quantum measurement dynamics, we form statements of the arrow of time in the quantum measurement. In Section 5.2, I describe quantum measurement trajectories in terms of a path integral formalism, supported by a probability distribution from which experimentally observed trajectories are sampled. Following this model, I consider time reversal of the measurement process in terms of trajectory dynamics and statistics. Here, I introduce an arrow of time statistic for individual quantum trajectories. In Section 5.3, I discuss the role of finite efficiency measurement for characterizing the arrow of time for quantum measurement trajectories. Following this discussion into Section 5.4, I explain a method to estimate time reversible trajectories from an experiment measurement record, collected with finite efficiency. I relate the likelihood of individual trajectory dynamics to the statistics of trajectory ensembles, showing that the statistics of the measurement, together with the measurement dynamics, satisfy a detailed fluctuation theorem. Lastly, I discuss the role of initial conditions for the arrow of time statistic in terms of absolute irreversibility and an integral fluctuation theorem.

5.1 A statistical arrow of time

The entanglement between a quantum system and its environment can be harnessed for indirect measurements, since measurements of the environment alone convey information and induce measurement backaction dynamics on the system state [136]. Because the outcomes of measurements on quantum systems are inherently probabilistic, the outcomes of measurements on the environment have a random character and are statistically described by the quantum state as a model parameter. Since the quantum state informs a predictive model of environment fluctuations, measurements on the environment can, in turn, serve as a predictor for the quantum state. In the fashion of Bayesian inference, quantum state tracking consists of estimating model parameters conditioned on experimentally detected environment fluctuations. This results in a conditional stochastic evolution of the quantum state, namely, a quantum trajectory [129, 133].

In circuit quantum electrodynamics, the high efficiency sampling of environment fluctuations has enabled tracking of individual quantum measurement trajectories [137–140]. The statistical properties of these trajectories [141–145], bear a conceptual similarity to classical stochastic trajectories of particles interacting with a thermal reservoir. For such classical trajectories, entropy production can be characterized by tracking the evolution of single particles and comparing the probability density for forward versus time reversed trajectories [146–150]. Experiments in classical systems [151–161] have verified that these entropy measures satisfy fundamental fluctuation theorems that relate microscopic dynamics to ensemble behavior [162–168]. More broadly, these are related to fluctuation theorems for distributions of thermodynamics quantities, which have been extended to

quantum systems [169–175]. There have been several proposals for experimental tests [176–183], as well as recent experimental results in closed quantum systems [184, 185].

In contrast, open quantum systems present new phenomena associated with measurement backaction [186–195]. We characterize the entropy production of an open quantum system with individual quantum measurement trajectories [186, 189, 196–198], using information entropy measures to characterize a statistical arrow of time in quantum measurement. We show how a statistical arrow of time is revealed by path probabilities of forward versus time reversed quantum trajectories [199–202]. As in the case of classical trajectories, these probability densities satisfy a fluctuation theorem that is consistent with the correspondence between microscopic dynamics and ensemble behavior.

5.2 Time reversal of quantum measurement trajectories

5.2.1 Quantum measurement trajectories

We consider quantum measurement trajectories from continuous dispersive measurement of a qubit. From many consecutive measurements in real-time, we form a piecewise continuous trajectory of the qubit dynamics. An individual measurement trajectory is described uniquely by a set of measurement records $\{r_k\}_{k=0}^{k=n-1}$ corresponding to a homodyne signal (Section 2.3 and Section 4.3). From each set of measurement records, we reconstruct a trajectory as a time series of density operators $\{\rho_k\}_{k=0}^{k=n}$. We use an iterative update scheme to infer the qubit state as informed by each consecutive measurement record. The dynamics of the trajectory results from the impression each stochastic measurement

record r_k has on our state-of-knowledge ρ_k. Each measurement step is characterized by a positive operator-valued measure (POVM) [203, 204],

$$M_{r_k} = \left(\frac{\delta t}{2\pi\tau}\right)^{1/4} \exp\left[-\frac{\delta t}{4\tau}(r_k\mathbb{1} - \sigma_z)^2\right] \tag{5.2.1}$$

where the measurement strength is the product of the signal integration duration δt and the measurement rate $1/\tau$. The POVM provides a state update conditioned on the measurement record from the relation,

$$\rho_{k+1} = \frac{M_{r_k}\rho_k M_{r_k}^\dagger}{\mathrm{tr}[M_{r_k}\rho_k M_{r_k}^\dagger]}. \tag{5.2.2}$$

When applying a resonant Rabi drive on the qubit during the measurement process, the measurement POVM (Eq. 5.2.1) is modified as,

$$M_{r_k,\Omega} = \left(\frac{\delta t}{2\pi\tau}\right)^{1/4} \exp\left[-i\frac{\Omega\,\delta t}{2}\sigma_y - \frac{\delta t}{4\tau}(r_k\mathbb{1} - \sigma_z)^2\right], \tag{5.2.3}$$

where Ω is the angular frequency of Rabi oscillations and we have chosen the phase of the coherent drive without loss of generality. When measurement time steps are small compared to the measurement strength and Rabi frequency ($\delta t \ll \Omega, 1/\tau$), the POVM of Eq. 5.2.3 can be separated into two steps: a quantum non-demolition (QND) measurement step (Eq. 5.2.2) and a qubit state rotation by the unitary operator $U = e^{-i\Omega\sigma_y\,\delta t/2}$. In the

small time step limit, the state update for measurement with a Rabi drive is,

$$\rho_{k+1} = \frac{U M_{r_k} \rho_k M_{r_k}^\dagger U^\dagger}{\mathrm{tr}[U M_{r_k} \rho_k M_{r_k}^\dagger U^\dagger]}. \tag{5.2.4}$$

5.2.2 Time reversal of a trajectory

The notion that the quantum measurement process can be reversed stems from studies of 'measurement undoing' [205], where weak measurements can effectively erase information from previous measurements. As such, time reversal of the measurement process is established by reversing dynamics for a single measurement update step, where time reversed measurement 'undoes' the backaction from forward measurement in a physically realizable way (Fig. 5.1). This measurement reversal has been observed in a variety of experimental platforms [137, 206–208] and analyzed in the context of the POVMs we employ here [209]. For each measurement by POVM M_{r_k}, there is a corresponding measurement $\tilde{M}_{r_k} = M_{\tilde{r}_k}$, where $\tilde{r}_k = -r_k$ is the time reversed measurement record which restores the initial state-of-knowledge, albeit with a statistical weight,

$$\tilde{M}_{r_k} M_{r_k} \rho_k M_{r_k}^\dagger \tilde{M}_{r_k}^\dagger = \frac{\delta t}{2\pi\tau} e^{-\frac{\delta t}{2\tau}(r_k^2+1)} \rho_k. \tag{5.2.5}$$

In addition, at each step the unitary evolution of the Rabi drive is reversed ($\Omega \to -\Omega$).

To explore the statistical cost of time-reversed dynamics along a quantum trajectory, with many time steps, we examine time reversal in the measurement process by comparing the likelihood of quantum trajectories that are ordered forward versus backward in time.

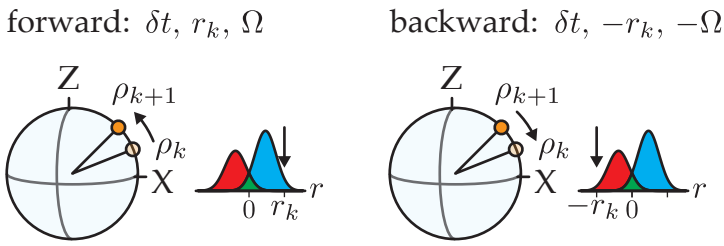

Figure 5.1: In a single update step, a measurement record r_k of duration δt from a continuous cavity probe induces backaction on the quantum state. Upon time reversal of this update step, the state responds to backaction of a measurement result of opposite sign $-r_k$ by returning to the initial state.

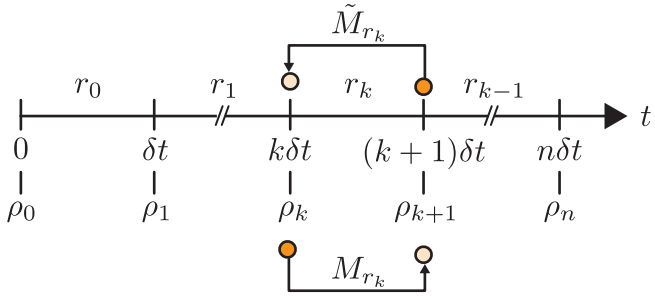

Figure 5.2: Schematic of the state and measurement labels for forward (M_{r_k}) and backward ($\tilde{M}_{r_k}$) state update procedures.

Given an initial state ρ, the probability density for a single measurement outcome r is,

$$\mathrm{tr}[M_r \rho M_r^\dagger]\, dr = \sqrt{\frac{\delta t}{2\pi\tau}} \left(\frac{1+z}{2} \exp\left[-\frac{\delta t}{2\tau}(r-1)^2 \right] + \frac{1-z}{2} \exp\left[-\frac{\delta t}{2\tau}(r+1)^2 \right] \right) dr \tag{5.2.6}$$

where $\rho = \frac{1}{2}(1 + x\sigma_x + y\sigma_y + z\sigma_z)$ and we write the probability density in terms of the Bloch sphere coordinates of the qubit density operator. Considering a short measurement duration relative to the inverse measurement strength ($\delta t \ll \tau$), we rewrite Eq. 5.2.6 in the

continuous limit as

$$P(r|z)\,dr \simeq \sqrt{\frac{\delta t}{2\pi\tau}}\exp\left[-\frac{\delta t}{2\tau}(r^2-2rz+1)\right]dr. \tag{5.2.7}$$

The path probability density for a measurement trajectory is the joint probability density for each measurement record along the trajectory [210]. We rewrite the measurement record and the trajectory coordinate as continuous functions of time and express the trajectory path probability density as,

$$\mathcal{P}(r(t))\,\mathcal{D}r = \exp\left[-\frac{1}{2\tau}\int_0^T dt\,\Big(r(t)^2-2r(t)z(t)+1\Big)\right]\mathcal{D}r(t), \tag{5.2.8}$$

and we have taken the product of probability densities for a continuous of set measurement records along the trajectory of duration T. The exponential prefactors of Eq. 5.2.8 are absorbed by $\mathcal{D}r$, the functional measure.

5.2.3 The arrow of time statistic

We statistically examine time reversal in the measurement process from the probability density of Eq. 5.2.8, and its associated information entropy. The relative likelihood of quantum trajectories that are ordered forward versus backward in time provides a statistical measure for the arrow of time. The relative likelihood between these physical processes is given by the ratio of path probability densities for forward-in-time and backward-in-time trajectories. We apply a time reversing transformation to the probability distribution of Eq. 5.2.8, $\mathcal{P} \to \tilde{\mathcal{P}}$ which is equivalent to the replacement $t \to T-t$ and flipping the

sign of the measurement records, $r(t) \to \tilde{r}(t) = -r(T-t)$, such that the time reversed trajectories adhere to the same equations of motion of their forward-in-time counterparts, ensuring reversible dynamics [200]. The time reversed probability density is

$$\begin{aligned}\tilde{\mathcal{P}}(r(t))\,\mathcal{D}r &= \mathcal{P}(\tilde{r}(t))\,\mathcal{D}\tilde{r} \\ &= \exp\left[-\frac{1}{2\tau}\int_0^T dt\,\left(\tilde{r}(t)^2 - 2\tilde{r}(t)\tilde{z}(t) + 1\right)\right]\mathcal{D}\tilde{r} \\ &= \exp\left[+\frac{1}{2\tau}\int_0^T dt\,\left(r(t)^2 + 2r(t)z(t) + 1\right)\right]\mathcal{D}r \\ &= \mathcal{P}(r(t))\exp\left[-\frac{2}{\tau}\int_0^T dt\,r(t)z(t)\right]\mathcal{D}r\end{aligned} \tag{5.2.9}$$

where we have expressed the time reversed probability density in terms of the forward-in-time probability density, with the replacements

$$\int_0^T dt\,(\tilde{r}(t)^2 + 1) = \int_0^T dt\,(r(t)^2 + 1) \tag{5.2.10}$$

and

$$\int_0^T dt\,\tilde{r}(t)\tilde{z}(t) = -\int_0^T dt\,r(t)z(t). \tag{5.2.11}$$

We calculate the arrow of time statistic $\mathcal{Q}$ as the logarithm ratio of the forward and backward probability densities,

$$\mathcal{Q} = \ln\frac{\mathcal{P}(r(t)|z_0)}{\tilde{\mathcal{P}}(\tilde{r}(t)|\tilde{z}(t))} = \frac{2}{\tau}\int_0^T dt\,r(t)z(t). \tag{5.2.12}$$

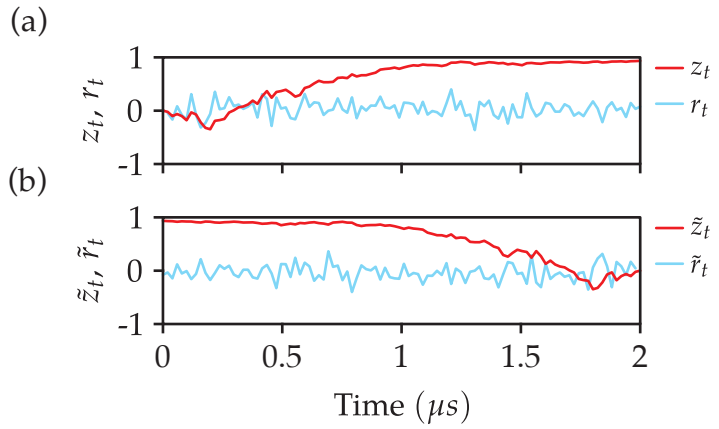

Figure 5.3: (a) The time evolution of a trajectory coordinate $z(t)$ (red) and its measurement record $r(t)$ (blue). (b) The backwards-in-time trajectory of (a) has a coordinate $\tilde{z}(t)$ that follows the same path as the forward-in-time trajectory coordinate $z(t)$, but with reversed time evolution. The backward-in-time trajectory has a measurement record $\tilde{r}(t)$ with an opposite sign and is reversed ordered in comparison to the forward trajectory measurement record.

This quantifies the arrow of time "length" in terms of the measurement record and trajectory coordinate. To gain a physical intuition for the arrow of time statistic $\mathcal{Q}$, we consider the measurement record in the limit of continuous time as a stochastic process $r(t) \propto z(t) + \sqrt{\tau} d\xi(t)$, where $d\xi$ is a zero mean Gaussian random variable. It is clear that positive contributions to the forward arrow of time occur when the record and state are correlated, since the integrand of Eq. 5.2.12 contains the product of the measurement record and coordinate. The path probability density of Eq. 5.2.8 describes the statistics and dynamics of QND measurement apart from Rabi driven qubit dynamics. In the case of measurement along with Rabi drive, Eq. 5.2.12 describes the arrow of time statistic in the weak driving limit $\Omega \delta t \ll 1$.

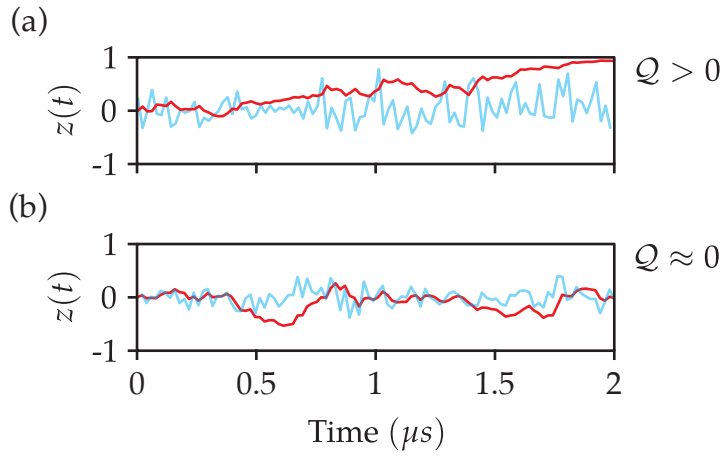

Figure 5.4: (a) The arrow of time statistic $\mathcal{Q}$ has a nonzero and positive value when the measurement record is correlated to the trajectory dynamics. This correlation is most pronounced by the dynamics of measurement projection. (b) A trajectory that does not display strong correlation between its coordinate and measurement record is similarly likely to evolve forwards or backwards in time.

5.2.4 A detailed fluctuation theorem

The time reversed probability density (Eq. 5.2.9) in terms of the arrow of time statistic (Eq. 5.2.12) defines the relation,

$$\frac{\mathcal{P}(r(t)|z_0)}{\tilde{\mathcal{P}}(r(t)|z_0)} = e^{\mathcal{Q}}, \tag{5.2.13}$$

which states the relative probability of a forward-in-time trajectory and its backward-in-time counterpart is exponential in the arrow of time statistic. Since the arrow of time statistic is determined by the measurement record and initial state of a trajectory (Eq. 5.2.12), we express Eq. 5.2.13 in terms of a fluctuation theorem

$$\frac{\mathcal{P}(+\mathcal{Q})}{\mathcal{P}(-\mathcal{Q})} = e^{\mathcal{Q}}. \tag{5.2.14}$$

This quantifies the relative probability of obtaining a forward pointing arrow of time with length $\mathcal{Q}$ to the probability of an arrow of the same length but backwards in time. The trajectories which produce a value of $\mathcal{Q}$ near zero have dynamics that appear similarly likely as either forward-in-time or backward-in-time trajectories. If a trajectory is characterized with a large value of $\mathcal{Q}$, the trajectory dynamics is exponentially more likely to be forward-in-time than backward-in-time. The fluctuation theorem expresses a relationship between the trajectory dynamics and the likelihood of the trajectory itself, which have interdependence that is ultimately captured by the arrow of time statistic definition (Eq. 5.2.12). When an ensemble of trajectories adheres to the fluctuation theorem of Equation 5.2.14, we establish a consistency between the microscopic dynamics of individual trajectories and the macroscopic statistics of trajectory ensembles.

5.3 Reversibility with inefficient measurement

5.3.1 Multiple measurement channels

In experiment, measurement occurs with finite quantum efficiency, which is evidenced by a discrepancy between the observed ensemble dephasing rate and the qubit dephasing rate due to the information acquired about qubit populations. Measurement with finite efficiency can be modeled with multiple measurement channels, where our experimental measurement record is but one of these channels [203]. When the qubit is measured by multiple channels, the measurement dynamics is described by a POVM characterizing the simultaneous measurement from every channel. An observer who has access to only one

channel then describes the qubit dynamics by averaging over all unknown measurement outcomes. Consequently, extra dephasing of the qubit state results from averaging over the unknown measurement outcomes, which leads to measurement dynamics that is not time reversible.

We construct a POVM for simultaneous measurement from multiple channels in two separate cases. In both cases, there is a measurement channel that corresponds to our experiment measurement record r, which is correlated to the qubit populations in the σ_z basis, denoted as z-measurement. In each case, there is another measurement channel for experimentally unmonitored measurements. In the first case, the experimentally unmonitored channel is a z-measurement with the measurement record ϑ_z. This corresponds to homodyne measurement of the cavity probe in the same quadrature as the experiment, conveying further information about the qubit populations. In the second case, the experimentally unmonitored measurement channel is a homodyne measurement of the cavity probe in a quadrature orthogonal to the experimentally monitored measurement channel, which we refer to as ϕ-measurement. For ϕ-measurement, the measurement record ϑ_ϕ contains information about phase shifts on the qubit imparted by an ac Stark shift due to photon fluctuations of the cavity probe [126, 211]. The measurement dynamics from z- and ϕ-measurement is depicted on the Bloch sphere in Figure 5.5. These two measurement schemes result in different backaction dynamics on the qubit state, which in turn, results in markedly different trajectory ensemble statistics.

Experimentally unmonitored z-measurement For the first case, both measurement channels are z-measurements and the measurement channels are described independently by

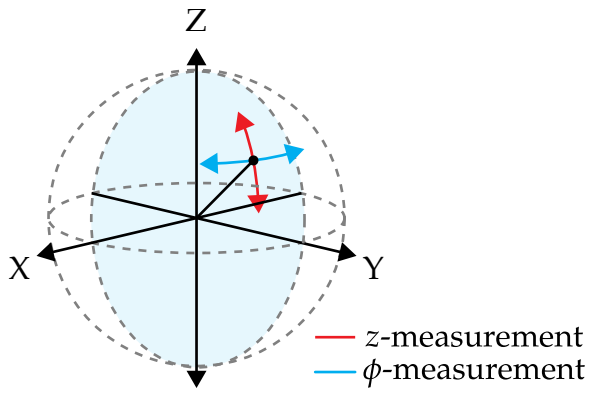

Figure 5.5: Homodyne measurements of the field quadrature correlated to the qubit populations (z-measurement) results in measurement projection toward the poles of the Bloch sphere. In contrast, homodyne measurements in the opposite field quadrature are correlated to the qubit phase and results in backaction dynamics without correlation to the qubit populations.

the POVMs M_{ϑ_z} and M_r which are of the same form as Eq. 5.2.1. The POVM for the simultaneous measurement of both of these channels is constructed from the product of their commuting POVM measurements,

$$\begin{aligned} M_{r,\vartheta_z} &= M_{\vartheta_z} M_r \\ &= \left(\frac{\delta t}{2\pi}\right)^{1/4} \left(\frac{2\gamma_z}{\tau}\right)^{1/4} \times \\ &\qquad \exp\left[-\frac{\delta t}{4\tau}(r-\sigma_z)^2 - \frac{\gamma_z \delta t}{2}(\vartheta_z - \sigma_z)^2\right], \end{aligned} \tag{5.3.1}$$

where $1/\tau$ and $2\gamma_z$ are the measurement rates for the experimentally monitored and unmonitored z-measurements. When an observer is informed by measurement records from both channels, the qubit state evolution follows the usual update equations for the density operator,

$$\rho_{k+1} = \frac{M_{r,\vartheta_z} \rho_k M_{r,\vartheta_z}^\dagger}{\mathrm{tr}[M_{r,\vartheta_z} \rho_k M_{r,\vartheta_z}^\dagger]}. \tag{5.3.2}$$

Upon averaging over all measurement records, the ensemble dephasing rate is $\Gamma = 1/2\tau + \gamma_z$, where $1/2\tau$ and γ_z are the measurement dephasing rates for each channel independently. Since the ensemble dephasing dynamics results from ignoring all measurement records, all observers agree on the ensemble dephasing rate.

With a description of the measurement process from multiple measurement channels, we can examine how an observer for each measurement channel accounts for the missing information of the other measurement channels. In the presence of multiple measurement channels, the POVM for a single measurement channel alone does not correctly describe the ensemble dynamics or statistics. Hence, any observer must update their qubit state of knowledge using the POVM that contains all measurement channels, such as Eq. 5.3.1, and then average over all possible measurement records from the other observers.

For example, for an observer who only knows the experimentally monitored measurement record r, the updated state is

$$\rho_a' \propto \int d\vartheta_z d\, M_{r,\vartheta_z} \rho_a M_{r,\vartheta_z}^\dagger. \tag{5.3.3}$$

In terms of state update equations, this expression is equivalent to performing an update with the experiment z-measurement POVM (Eq. 5.2.1) and then dephasing the qubit state by rescaling the magnitude of the qubit coherence by a factor $e^{-(\Gamma - 1/2\tau)\delta t} = e^{-\gamma_z \delta t}$.

Experimentally unmonitored ϕ-measurement In the second case, we consider an experimentally monitored z-measurement channel and an experimentally unmonitored ϕ-measurement channel. The ϕ-measurements induce qubit state backaction described by

the POVM,

$$M_{\vartheta_\phi} = \left(\frac{\gamma_\phi \delta t}{\pi}\right)^{1/4} \exp\left[-\frac{\gamma_\phi \delta t}{2}(\vartheta_\phi^2 + 2i\vartheta_\phi \sigma_z)\right], \tag{5.3.4}$$

which alters the qubit state by a unitary rotation of angle $\vartheta_\phi \gamma_\phi \delta t$ in the σ_z basis. The ϕ-measurement record ϑ_ϕ has a zero-mean Gaussian distribution according to the distribution of cavity photon number fluctuations. Upon integrating over ϕ-measurement outcomes, we find this POVM contributes an ensemble dephasing rate γ_ϕ due to photon number fluctuations of the cavity probe. The POVM for the simultaneous measurement of both of these channels is,

$$\begin{aligned} M_{r,\vartheta_\phi} &= M_r M_{\vartheta_\phi} \\ &= \left(\frac{\delta t}{2\pi}\right)^{1/2} \left(\frac{2\gamma_\phi}{\tau}\right)^{1/4} \times \\ &\qquad \exp\left[-\frac{\delta t}{4\tau}(r - \sigma_z)^2 - \frac{\gamma_\phi \delta t}{2}(\vartheta_\phi^2 + 2i\vartheta_\phi \sigma_z)\right], \end{aligned} \tag{5.3.5}$$

where $1/\tau$ and $2\gamma_\phi$ are the measurement rates for the experimentally monitored z-measurement and the experimentally unmonitored ϕ-measurements respectively. When an observer is informed by measurement records from both channels, state update occurs in similar form to Equation 5.3.2. As stated previously, if an observer only knows the experimentally monitored measurement record, the observer must average over unknown measurements. In this case, averaging at each time step is equivalent to rescaling off-diagonal elements according to the ensemble dephasing rate $\Gamma = 1/2\tau + \gamma_\phi$.

5.3.2 The path probability for multiple observers

We examine the arrow of time statistic for each case of multiple measurement channels and show that the arrow of time depends only on z-measurement. First, we consider the path probability density for the case of two z-measurement channels and calculate the arrow of time statistic following the procedure in Section 5.2.2. Following this discussion, we consider the case of z- and ϕ-measurement channels, to find that ϕ-measurement results do not contribute to the arrow of time statistic directly.

Path probability with additional z-measurements Given the qubit state ρ, the probability density of the measurement records for two z-measurement channnels is,

$$\begin{aligned}\mathrm{tr}[M_{r,\vartheta_z}\rho M_{r,\vartheta_z}^\dagger]\, dr d\vartheta_z = \frac{\delta t}{\pi}\sqrt{\frac{\gamma_z}{2\tau}}\Bigg(\cdots \\ \frac{1+z}{2}\exp\left[-\frac{\delta t}{2\tau}(r-1)^2 - \gamma_z \delta t(\vartheta_z - 1)^2\right] + \\ \frac{1-z}{2}\exp\left[-\frac{\delta t}{2\tau}(r+1)^2 - \gamma_z \delta t(\vartheta_z + 1)^2\right]\Bigg)\, dr d\vartheta_z,\end{aligned} \tag{5.3.6}$$

where $\rho = \frac{1}{2}(1 + x\sigma_x + y\sigma_y + z\sigma_z)$. We rewrite Eq. 5.3.6 in the continuous limit ($\delta t \ll \tau$, $1/2\gamma_z$) and only consider exponentiated terms since we are interested in path probability ratios,

$$P(r, \vartheta_z)\, dr d\vartheta_z \propto \exp\left[-\frac{\delta t}{2\tau}(r^2 - 2rz + 1) - \gamma_z \delta t\,(\vartheta_z^2 - 2\vartheta_z z + 1)\right] dr d\vartheta_z. \tag{5.3.7}$$

We rewrite the measurement record and the trajectory coordinate as continuous functions of time and express the trajectory path probability density such:

$$\begin{aligned} P(r(t),\vartheta_z(t))\,\mathcal{D}r\mathcal{D}\vartheta_z = \\ \exp\Big\{\int_0^T dt\,\Big[-\frac{r(t)^2+1}{2\tau}-\gamma_z(\vartheta_z(t)^2+1) \\ +\Big(\frac{r(t)}{\tau}+2\gamma_z\vartheta_z(t)\Big)z(t)\Big]\Big\}\,\mathcal{D}r\mathcal{D}\vartheta_z, \end{aligned} \tag{5.3.8}$$

where exponential prefactors are absorbed by the functional measures $\mathcal{D}r$ and $\mathcal{D}\vartheta_z$. We find the time reversed path probability density by the replacement $t \to T-t$ and flipping the sign of the measurement records,

$$r(t) \to -r(T-t), \quad \vartheta_z(t) \to -\vartheta_z(T-t). \tag{5.3.9}$$

The logarithm ratio of the forward and backward probability densities gives an arrow of time statistic,

$$\begin{aligned} \mathcal{Q} &= \ln\frac{P(r(t),\vartheta_z(t))}{\tilde{P}(r(t),\vartheta_z(t))} \\ &= 2\int_0^T dt\,\Big(\frac{r(t)}{\tau}z(t)+2\gamma_z\vartheta_z(t)z(t)\Big). \end{aligned} \tag{5.3.10}$$

The arrow of time statistic depends on both z-measurement channels additively; the first term of Eq. 5.3.10 is the correlation between the experimentally monitored z-measurement record $r(t)$ and the coordinate $z(t)$ and the second term is the correlation between the unmonitored z-measurement record $\vartheta_z(t)$ and the coordinate $z(t)$.

The arrow of time statistic is evaluated with the trajectory coordinate $z(t)$ according to an observer of *all* measurement channels. An observer with only partial information of all measurement records cannot calculate the arrow of time statistic for a single trajectory. Since this observer estimates a trajectory coordinate by averaging over unknown measurement outcomes, this does not match $z(t)$ in general and results in irreversible trajectory dynamics.

Path probability with additional ϕ-measurements We now examine the arrow of time statistic in the case of simultaneous z- and ϕ- measurement. Considering the POVM of Equation 5.3.5, the probability density in the measurement records r and ϑ_ϕ is,

$$\begin{aligned}\mathrm{tr}[M_{r,\vartheta_\phi}\rho M_{r,\vartheta_\phi}^\dagger]\,dr d\vartheta_\phi = \frac{\delta t}{\pi}\sqrt{\frac{\gamma_\phi}{2\tau}}\exp\big(-\gamma_\phi \delta t\,\vartheta_\phi^2\big)\times \\ \left(\frac{1+z}{2}\exp\left[-\frac{\delta t}{2\tau}(r-1)^2\right]+\frac{1-z}{2}\exp\left[-\frac{\delta t}{2\tau}(r+1)^2\right]\right)dr d\vartheta_\phi.\end{aligned} \tag{5.3.11}$$

The path probability density in the measurement record ϑ_ϕ is independent of the trajectory coordinate. The likelihood of a ϕ-measurement outcome manifestly does not depend on the trajectory due to the time reversal invariance of the cavity probe vacuum fluctuations. We again follow the procedure of Section 5.2.3 to determine the arrow of time statistic which for simultaneous z- and ϕ- measurement is

$$\begin{aligned}\mathcal{Q} &= \ln\frac{P(r(t),\vartheta_\phi(t))}{\tilde{P}(r(t),\vartheta_\phi(t))} \\ &= \frac{2}{\tau}\int_0^T dt\, r(t)z(t).\end{aligned} \tag{5.3.12}$$

The arrow of time statistic does not depend on ϕ-measurement records since both the statistics and the dynamics of ϕ-measurement are time reversal invariant. However, the arrow of time statistic can be influenced by ϕ-measurement indirectly, as the ϕ-measurement backaction dynamics enter into Equation 5.3.12 through the trajectory coordinate $z(t)$.

While Equation 5.3.12 is equivalent to the arrow of time statistic for a single z-measurement channel (Eq. 5.2.12), the rate of change of the arrow of time statistic is proportional to measurement rate for z-measurements and not the ensemble dephasing rate.

5.4 Measurement trajectories of a transmon qubit

5.4.1 Experiment setup

To experimentally investigate quantum trajectories, we measure a transmon qubit dispersively coupled to a single electromagnetic mode of a three dimensional waveguide cavity. The qubit and cavity mode resonator, of frequencies ω_q and ω_c respectively, have a dispersive Jaynes-Cummings interaction given by the interaction Hamiltonian $H_{\text{int}} = -\chi a^\dagger a \sigma_z$ where χ is the dispersive coupling rate, $a^\dagger a$ is the number operator for the cavity mode, and σ_z is the Pauli operator that commutes with the qubit Hamiltonian. This interaction Hamiltonian describes a qubit-state-dependent cavity resonance, for which the cavity resonance shifts by $2|\chi|$ whether the qubit occupies its ground or excited state. Thus, the cavity mode provides pointer states for the qubit populations.

Qubit measurement occurs when a microwave tone probes the cavity resonance and

acquires a qubit-state-dependent phase shift. Since the shift of the cavity resonance $2|\chi|$ is small compared to the cavity linewidth κ, the measurement tone has a relatively small qubit-state-dependent phase shift. By virtue of this qubit–cavity interaction, the qubit state is correlated to a single field quadrature of the microwave probe. The field quadrature is subsequently amplified by a near-quantum-limited Josephson parametric amplifier [212, 213] operating in phase sensitive mode.

Next, the amplified quadrature is downconverted to DC and digitized into time steps to obtain a set of measurement records, each corresponding to a duration δt. From these measurement records, we reconstruct trajectories iteratively by updating the qubit state using the Equation 5.2.1. We apply a Rabi drive in addition to measurement; the qubit evolution includes a dynamics due to the Hamiltonian $H/\hbar = \Omega\sigma_y/2$, which is in a rotating frame of the qubit transition.

$\omega_q/2\pi$	4.01 GHz
$\omega_c/2\pi$	6.8316 GHz
$\chi/2\pi$	-0.6 MHz
$\kappa/2\pi$	9.0 MHz
δt	16 ns
T_2^*	15 μs
$1/\tau$	1.97 μs^{-1}
$\Omega/2\pi$	2.16 MHz
η	0.4

Table 5.1: The quantum trajectory experiment parameters for dispersive measurement of a transmon qubit.

5.4.2 Modeling finite efficiency measurements

The dispersive measurement process occurs with a quantum efficiency η from the combined effects of collection efficiency, added noise from the amplification chain, and additional environmental dephasing characterized by T_2^* Ramsey measurements. The quantum efficiency is defined by the ratio of the expected dephasing rate from measurement to the total dephasing rate: $\eta = (1/2\tau)/\Gamma$, where Γ is the ensemble dephasing during the measurement.

As mentioned in Section 5.3.1, dephasing due to finite efficiency breaks the time reversibility of the measurement dynamics. To restore reversibility, we estimate the quantum trajectories that could be obtained by an observer with access to both experimentally monitored and unmonitored measurement channels. These trajectories serve as the model that governs the probability density for forward and reversed measurement sequences.

The finite quantum efficiency in our experiment arises predominantly from attenuation of the cavity probe between the cavity and Josephson parametric amplifier. This attenuation can be modeled as a beam splitter (Fig. 5.6a) where the cavity probe is split between two observers whom denote "Alice," who monitors the experiment z-measurement channel, and "Bob," who monitors an experimentally unmonitored measurement channel. A third observer, "Charlie" has access to both Alice and Bob's measurement records and can therefore track time reversible trajectories.

For every experimentally sampled quantum trajectory, we perform a statistical resampling method to create multiple trajectories, each of which is an estimate for a single trajectory observed by Charlie. This ensemble of possible trajectories for Charlie corresponds

to an unraveling of the Lindblad master equation that describes Alice's quantum trajectory. This unraveling, however, depends on which type of measurements Bob makes on his experimentally unmonitored homodyne measurement channel. While Alice uses a parametric amplifier to perform the z-measurement corresponding to our experimentally monitored measurement record, Bob's homodyne measurements are considered in both extremal cases: Bob can perform either z-measurement or ϕ-measurement as discussed in Section 5.3.1.

We model the beam splitter in a time segmented fashion. In this approach, a measurement channel is probabilistically selected to perform a measurement for a single time step. The inefficient measurement of this experiment is equivalent to Alice doing in qubit measurement for only a fraction of all time, but with perfectly efficient measurements and a measurement strength 2Γ set by the ensemble dephasing rate $\Gamma = 1/\eta\tau$, where $1/\tau$ is the strength of Alice's measurement channel alone. Alice makes perfectly efficient measurements for a fraction η of her measurement records, and records noise upon the remaining $1-\eta$ of measurement records. Likewise, Bob performs efficient measurements for a fraction of time steps $1-\eta$, at each time step when Alice records noise. A possible trajectory for Charlie is constructed by updating the state with Alice and Bob's efficient measurements. This approach is operationally equivalent to the model of multiple measurement channels presented Section 5.3 and this method is well suited to the discrete state update steps of the experimental data that we study.

This method enables us to construct an ensemble of possible trajectories for Charlie. For each of Alice's records, a random fraction η of the records are sampled as actual mea-

surements and contribute to an update of the qubit state with Equation 5.2.1 (using the measurement strength $1/\tau \to 1/\eta\tau = 2\Gamma$). For Bob's measurement steps, we create hypothetical measurements in either situation of z-measurements (Eq. 5.2.1) or ϕ-measurement (Eq. 5.3.4).

Since Bob's z-measurements are characterized by the POVM of Equation 5.2.1 we sample Bob's z-measurement records with the stochastic process $\vartheta_z(t) = z(t) + \sqrt{\eta\tau/\delta t}\xi(t)$, where $\vartheta_z(t)$ is Bob's measurement record for z-measurements, $z(t)$ is the trajectory coordinate according to Charlie, and $d\xi$ is a zero-mean Gaussian of unit variance. Likewise, Bob's ϕ-measurements are characterized by the POVM of Equation 5.3.4 and we sample the ϕ-measurement records according to the stochastic process $\vartheta_\phi(t) = \sqrt{\eta\tau/\delta t}\xi(t)$, where $\vartheta_\phi(t)$ is Bob's measurement record for ϕ-measurements. From a single sequence of experimentally obtained measurement records we create an ensemble of unraveled trajectories which has an average evolution consistent with the single finite efficiency experiment trajectory. In Figure 5.7, several unraveled quantum trajectories are shown for the two limiting cases of Bob's z- and ϕ- measurements.

5.4.3 The arrow of time of trajectory ensembles

We examine the arrow of time for an ensemble of experimentally sampled quantum trajectories. Figure 5.8a displays distributions of the arrow of time statistic, with each distribution evaluated from 2.8×10^5 trajectories at different evolution times. Each trajectory duration is associated with two different distributions, corresponding to the cases of z- or ϕ- measurement for Bob's measurement, the experimentally unmonitored measurement

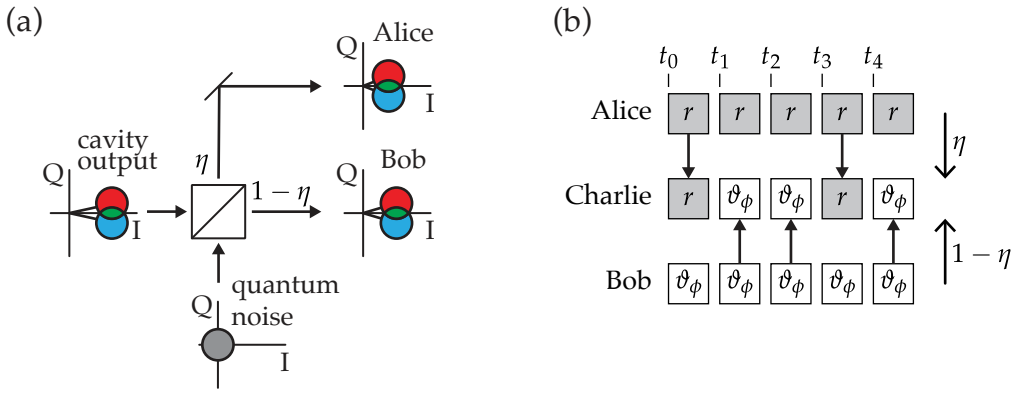

Figure 5.6: (a) Finite quantum efficiency can be modeled as a beam splitter, where the cavity probe is split between two observers, Alice and Bob. (b) We model the beamsplitter as a time segmented splitter, which directs the signal to Alice or Bob at each time step with probabilities η and $1-\eta$ respectively. The measurement record of a third observer, Charlie, who has access to both Alice and Bob's records can be constructed by taking either Alice's record or Bob's record at each time step. We construct an ensemble of possible pure state trajectories for Charlie, by sampling many possible measurement records for Bob's measurement channel.

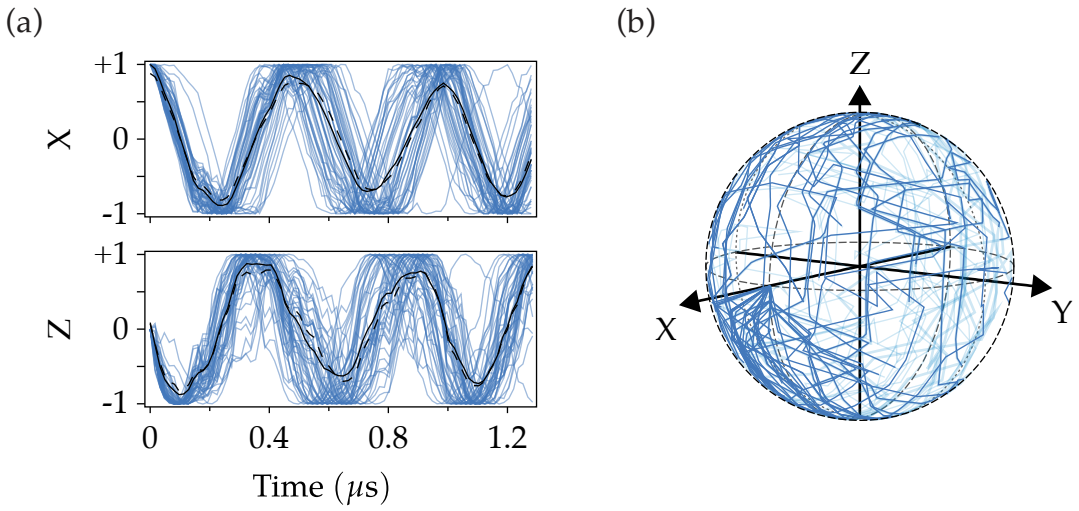

Figure 5.7: (a) An ensemble of estimated trajectories for Charlie's trajectory, when Bob has performed z-measurements. An average of these trajectories over Bob's measurement (black solid line) matches the finite quantum efficiency trajectory based only on Alice's record (dashed line). (b) If Bob instead performs ϕ-measurements, the resulting backaction on the qubit causes state evolution outside the X–Z plane.

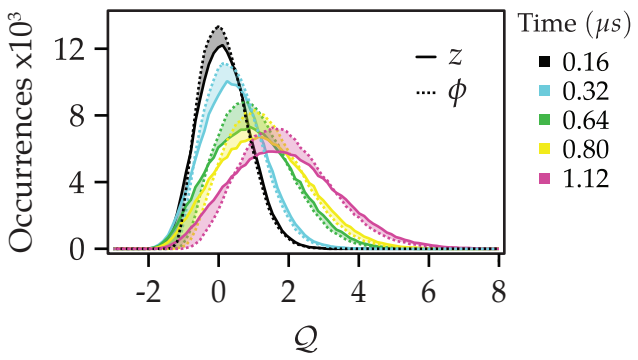

Figure 5.8: The distributions $\mathcal{P}(\mathcal{Q})$ for different propagation times. The solid curves represents Alice's arrow of time when Bob performs z-measurements and the dashed curve represents the case when Bob performs ϕ-measurements, constraining a range of possible values for Alice's arrow of time.

channel. In both cases, the distributions represent the contribution to the arrow of time statistic due to Alice's measurements. The arrow of time statistic is calculated from an estimate of Charlie's trajectory, according to either Equation 5.3.10 or Equation 5.3.12.

Here we see the role of measurement backaction in the choice of Bob's measurement, where Bob's z-measurement leads to a greater occurrence of both forward-likely and backward-likely trajectories as indicated by the broad $\mathcal{Q}$ distribution compared to the $\mathcal{Q}$ distribution for ϕ-measurements. When Bob performs z-measurements, trajectories take on extremal values of z at short times due to the backaction of Alice and Bob's collective z-measurements. In turn, the arrow of time statistic has a greater magnitude since there is a relatively stronger correlation and anti-correlation of Alice's measurement record.

5.4.4 A detailed fluctuation theorem

Notably, negative values of the arrow of time statistic $\mathcal{Q}$ occur for Alice's arrow of time for both Bob's z- and ϕ-measurements, corresponding to trajectories where the time reverse

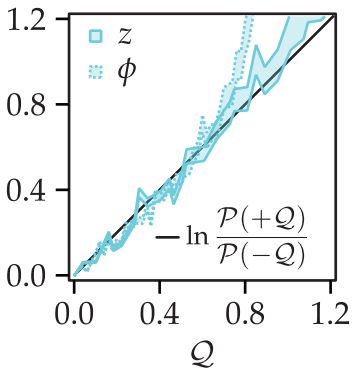

Figure 5.9: The detailed fluctuation relation. The distributions of $\mathcal{Q}$ at time $t = 0.32$ μs in Figure 5.8 are used to calculate the quantity $\ln(\mathcal{P}(\mathcal{Q})/\mathcal{P}(-\mathcal{Q}))$. The detailed fluctuation relation calculation agrees well with the theory prediction (black line) for both cases of Bob's measurement. The shaded region indicates the statistical uncertainty in quantity $\ln(\mathcal{P}(\mathcal{Q})/\mathcal{P}(-\mathcal{Q}))$.

process is more likely. This phenomenon of negative entropy production is well known in microscopic stochastic systems and is typically characterized by a fluctuation theorem [147–150, 163–167, 214]. In Figure 5.9 we show that the data are in agreement with a detailed fluctuation theorem (Eq. 5.2.14). For small values of the arrow of time statistic $\mathcal{Q}$, the agreement with the detailed fluctuation theorem indicates that the experimentally sampled relative occurrence of $\mathcal{Q}$, as given by the left hand side of Equation 5.2.14, is consistent with the definition of $\mathcal{Q}$ on the right hand side. The occurrence of trajectories in an ensemble is prescribed by the path probability density for each trajectory, which implies the relative occurrence of forward-in-time and backward-in-time trajectories coincides with arrow of time statistic as defined. However, for larger values of $\mathcal{Q}$, the fluctuation theorem is clearly nonlinear, a feature that is related to the presence of absolute irreversibility.

5.4.5 An integral fluctuation theorem and absolute irreversibility

To investigate the role of absolute irreversibility, we focus on measurement without Rabi drive ($\Omega = 0$). In this case, the measurement operators commute with the qubit Hamiltonian resulting in a quantum non-demolition measurement. We consider the case where the qubit is prepared such that $\langle \sigma_x \rangle \lesssim 1$ and measurements project the system toward the stationary points $\langle \sigma_z \rangle \to \pm 1$. Figure 5.10 displays the distributions for the arrow of time statistic for several evolution times. Note that Bob's measurement does not affect Alice's arrow of time in this case.

For the simple dynamics of this semi-classical measurement, the probability density of $\mathcal{Q}$ is found analytically by solving the measurement update equation of motion and performing a change of variables in the measurement record probability density [200],

$$\mathcal{P}(\mathcal{Q}) = \sqrt{\frac{T}{2\pi\tau}\frac{e^{\mathcal{Q}}}{e^{\mathcal{Q}}-1}}\exp\left\{-\frac{T}{2\tau}-\frac{\tau}{2T}[\cosh^{-1}(e^{\mathcal{Q}/2})]^2\right\}. \tag{5.4.1}$$

Histograms of $\mathcal{Q}$ from experiment are plotted for a selection of final times T with their corresponding theoretical probability density in dashed lines.

Clearly, the relative probabilities for forward and backwards arrows of time in this measurement case do not satisfy the detailed fluctuation theorem (Eq. 5.2.14). This is because the detailed fluctuation relation is only satisfied for the total statistical entropy change during a process [148]. In the presented case, the arrow of time statistic does not capture the contributing influence of the initial state of the trajectory, hence quantum measurement is, in general, a nonequilibrium, irreversible process. Here, the initial state imposes a

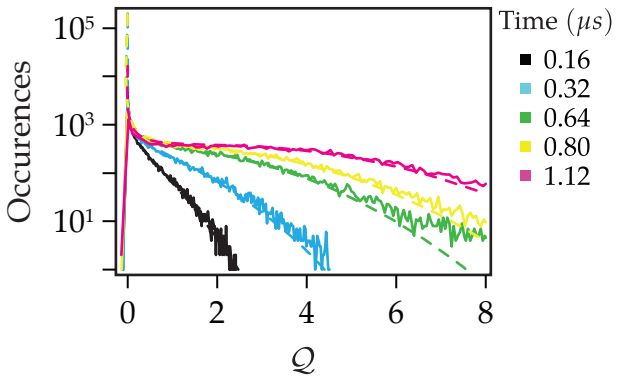

Figure 5.10: The distribution of the arrow of time statistic for several measurement durations. At all times the distribution is biased to positive values of $\mathcal{Q}$ due the strong correlation between the measurement record and the qubit state during the measurement process.

lower bound on the possible values of $\mathcal{Q}$ [200]. This sensitivity to initial conditions results from the 'un'-likelihood of a particular initial state, quantified by an absolute irreversibility [215–218]. As presented in Figure 5.10b, the absolute irreversibility is quantified by the integral fluctuation theorem,

$$\langle e^{-\mathcal{Q}} \rangle = 1 \tag{5.4.2}$$

which gives a deviation from unity resulting from the ensemble of trajectories containing a surplus of state updates that have a positive statistical arrow of time. This is due to the favoring of correlations between the qubit state and measure record from the measurement projection process. This contribution to the entropy is physically analogous to the entropy increase associated with irreversible expansion of gas. The semi-classical measurement case discussed here clearly illustrates absolute irreversibility due to initial conditions since the initial state is far from the fixed points of the measurement dynamics.

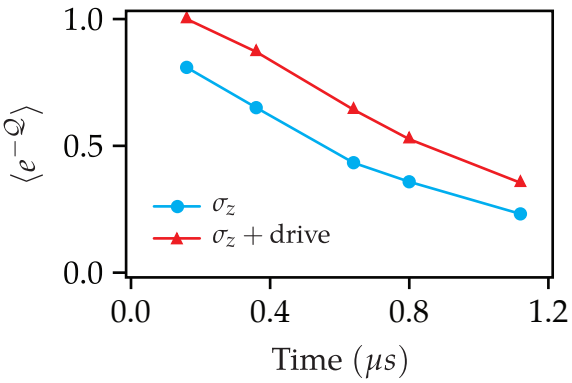

Figure 5.11: Calculation of the integral fluctuation theorem reveals absolute irreversibility of the measurement process due to initial conditions. Measurement projection favors dynamics with strong correlation between the measurement records and the qubit state, thus producing trajectories with a greater forward-in-time likelihood.

In summary, the dynamics of continuous quantum measurement exhibits a statistically defined arrow of time. Since continuous quantum measurement leads to a probabilistic dynamics of the quantum state and the measurement dynamics is time reversible, we can consider probabilities associated with both forward and reversed dynamics. We infer a statistical arrow of time from these probabilities, defined from the information entropy associated to the measurement process. The irreversible dynamics of measurement dephasing, an unavoidable feature in experimental quantum measurement, is addressed by a statistical sampling method to reconstruct the most-likely time reversible measurement dynamics. The experimental data show a statistical arrow of time emerges in quantum measurement consequent of the correlation between a qubit state and measurement outcomes. Ensembles of the trajectories are used to determined the likelihood for a certain arrow of time "length." The arrow of time likelihood follows a fluctuation relation, which confirms we have accurately defined the arrow of time statistic for dispersive quantum

measurement. Furthermore, we have identified an entropy contribution due to the dynamics of quantum measurement projection. This "absolute irreversibility" is associated to the process of wavefunction collapse, which makes an indisputable contribution to a forward arrow of time.

Chapter 6

Quantum Bath Engineering with a Photonic Crystal

This chapter summarizes a quantum bath engineering experiment for state preparation of a superconducting qubit using a microwave photonic crystal environment. As discussed in Chapter 1, quantum bath engineering is a method to leverage environment degrees of freedom as a resource for quantum control. In Section 6.1 of this chapter, I motivate an operational approach to quantum bath engineering by addressing how the environment density of states influences qubit dissipation. I present a microwave photonic crystal in the context of an environment for a quantum circuit in Section 6.2. In Section 6.3, I describe an experimental setup of a transmon circuit interacting with a photonic crystal environment. The photonic crystal density of state is characterized from unitary and dissipative dynamics of the transmon qubit. I then present a theoretical overview of Lindblad dynamics for a driven and dissipative qubit in Section 6.4. In Section 6.4.2, I present experimental results

of quantum state stabilization of qubit superposition states.

6.1 Bath engineering for quantum control

6.1.1 Engineering Lindblad dynamics

The Lindblad equation describes the dissipative dynamics of a quantum system (conditions and assumptions are discussed in Chapter 4). In the interaction frame, the reduced density matrix of the quantum system evolves accordingly to the master equation,

$$\dot{\rho} = \mathcal{L}\rho = \sum_k \gamma_k \left(L_k^\dagger \rho L_k - \frac{1}{2}\{L_k^\dagger L_k, \rho\} \right) \tag{6.1.1}$$

where the jump operators L_k account for dissipative transitions of the system state due to interactions with the environment and γ_k are the rates of these jump transitions. The Lindblad dynamics of Eq. 6.1.1 is an effective description of the quantum system which is obtained by averaging over environment degrees of freedom.

The jump operators result from specific interactions between the system and the quantum degrees of freedom of the environment. The dissipation rate for each jump operator is determined by correlations of environment degrees of freedom, given by the environment spectral density of states, and calculated by expectation values of system-environment interaction operators averaged over the environment evolution. The rate of dissipation γ_k for a jump transition L_k is proportional to the environment spectral density of states at the transition energy of the system.

A typical decay process described by the Lindblad master equation is the energy relaxation of a qubit due to spontaneous emission. By considering the joint dynamics of the system and its environment in the rotating frame of the qubit transition (see Section 4.1), the qubit decays to its ground state according to the master equation,

$$\dot{\rho} = \gamma \mathcal{D}[\sigma]\rho, \tag{6.1.2}$$

where γ is the rate of spontaneous emission, $\sigma = |g\rangle\langle e|$ is the lowering operator in the qubit eigenbasis, and $\mathcal{D}[L]\rho = (2L\rho L^\dagger - \{L^\dagger L, \rho\})/2$ is the dissipation operator. In Fig. 6.1a, the time evolution of this decay process is depicted on the Bloch sphere as all qubit states evolve toward the ground state.

While qubit decay is generally undesirable, the inevitable decay of a qubit to its ground state is exceptionally useful for preparation of high fidelity qubit states. In principle, a qubit can decay to an arbitrary state on the Bloch sphere (Fig. 6.1b) by adapting its interaction with its environment and the environment spectral density of states.

The process of spontaneous emission can be drastically altered by applying a strong dipole-resonant coherent drive. A single electromagnetic mode supporting a coherent drive enhances the effective coupling between qubit eigenstates, and we refer to the qubit as *dressed* by the electromagnetic mode. The qubit dynamics are described by an effective Hamiltonian with *dressed qubit* eigenstates, provided the qubit is driven strongly $g\sqrt{\bar{n}} \gg \gamma$, where $2g$ is the angular frequency of vacuum Rabi oscillations between the qubit and electromagnetic mode and $\bar{n}$ is the average photon occupation of the coherent drive.

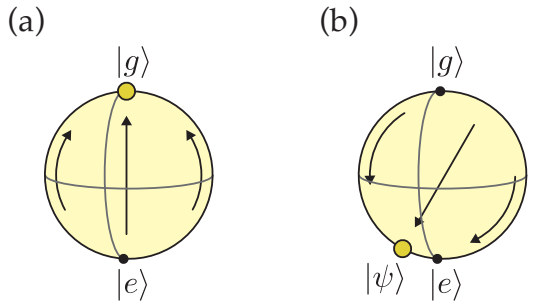

Figure 6.1: (a) The ubiquitous situation of a qubit decaying to its ground state via spontaneous emission. (b) In principle, the dissipation of a qubit can be engineered to decay to a new effective ground state on the Bloch sphere.

Although the coherent drive has introduced a new energy scale $g\sqrt{\bar{n}}$ to the system dynamics, we will assume the environment density of states is independent to this energy scale. The time evolution of the dressed qubit, as derived from the joint system-environment dynamics, is given by reduced density matrix master equation,

$$\dot{\rho} = \frac{\gamma}{4}\mathcal{D}[\tilde{\sigma}_z]\rho + \frac{\gamma}{4}\mathcal{D}[\tilde{\sigma}]\rho + \frac{\gamma}{4}\mathcal{D}[\tilde{\sigma}^\dagger]\rho, \tag{6.1.3}$$

where the operator $\tilde{\sigma}_z$ commutes with the dressed qubit Hamiltonian. As illustrated in Fig. 6.2a, the jump operator $\tilde{\sigma}_z$ dephases the dressed qubit, and the jump operators $\tilde{\sigma} = |+x\rangle\langle -x|$ and $\tilde{\sigma}^\dagger = |-x\rangle\langle +x|$ correspond to transitions between the dressed qubit eigenstates. The latter two dissipation terms ($\tilde{\sigma}$ and $\tilde{\sigma}^\dagger$) describe equal and opposite incoherent dynamics, which results in a maximally mixed qubit steady state.

Since we have assumed the environment correlations are frequency independent, all the dissipation processes of Eq. 6.1.3 have matching dissipation rates, which is proportional to γ, the spontaneous emission rate. The separate modification of each dissipation rate in Eq. 6.1.3 can result in a qubit steady state with nonzero coherence. Similar to en-

ergy relaxation of a bare qubit, the driven qubit can decay to a pure state by suppressing one of the jump transitions between the dressed qubit eigenstates.

The essence of quantum bath engineering is to selectively control system dynamics by the modification of the environment density of states. In terms of Fermi's Golden Rule [219], the dissipation rates are proportional to the spectral density of states at the frequency of the jump operator transition,

$$\gamma \propto \rho_{\mathrm{DOS}}(\omega)|\langle f|\,\mathcal{H}\,|i\rangle|^2, \tag{6.1.4}$$

where $\rho_{\mathrm{DOS}}(\omega)$ is the local density of states of the environment at the jump transition frequency ω, $|i\rangle$ and $|f\rangle$ are respectively the initial and final states of the system and environment, and $\mathcal{H}$ is the interaction Hamiltonian of the joint system and environment. When the environment density of states is frequency dependent, the dissipation rate for each jump transition can be treated independently. The independent modification of each dissipation rate is a resource for quantum state preparation.

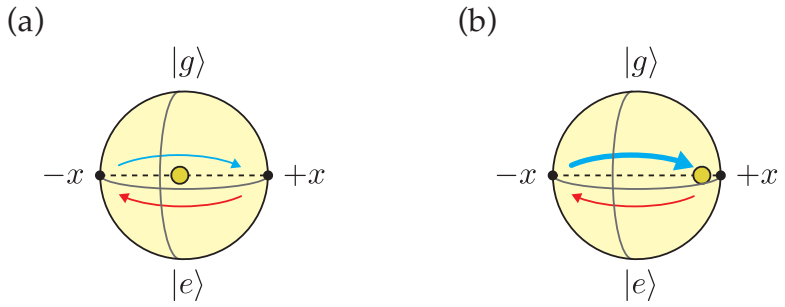

Figure 6.2: In the rotating frame of bare qubit, the long-time dynamics of the jump transitions result in a steady state (yellow point). Qubit dynamics also include Rabi oscillations and dephasing about the x-axis. (a) When the environment correlations are frequency independent, the steady state is maximally mixed qubit steady state. (b) When environment correlations favor a jump transition disproportionately, the qubit steady state has nonzero coherence.

6.2 A photonic crystal to shape the density of states

The preparation of a pure qubit superposition state requires dissipation rates to be incommensurate when there are competing dissipation processes. This implies that the environment spectral density of states must strongly vary on an energy scale corresponding to the driven qubit dynamics. The electromagnetic modes that form the bands and gaps of a photonic crystal are a resource for energy selective dissipation, since the decay of an emitter into a photonic crystal is strongly influenced by the presence of the photonic band gap [220, 221].

In an optical context, a photonic crystal is a medium with a spatially modulated index of refraction. When the modulation length scale is comparable to the wavelength of the light, the medium will act as a mirror for certain wavelengths of light, which corresponds to the opening of a photonic band gap in the dispersion relation of the medium [222]. Analogously, a spatially periodic impedance along a one-dimensional microwave transmission line forms a photonic crystal (Fig. 6.3a).

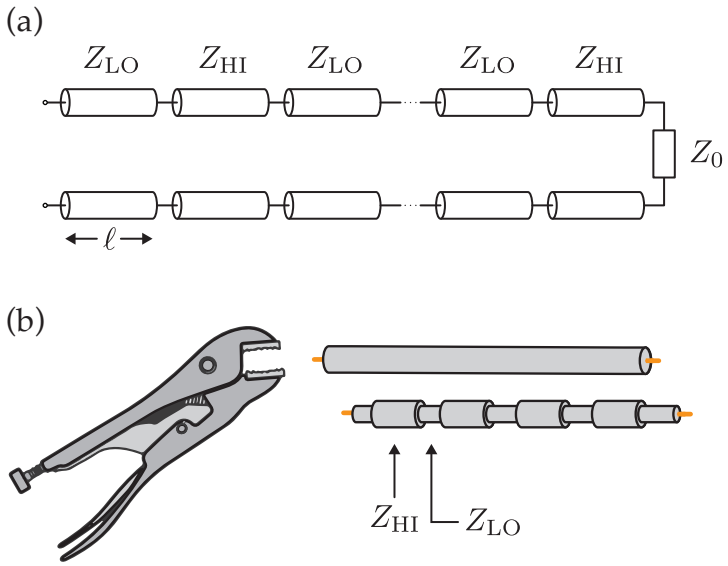

Figure 6.3: (a) A spatially periodic impedance along a one-dimensional microwave transmission line forms a photonic crystal. Here, each transmission line section has a physical length ℓ and a characteristic impedance (Z_{HI} or Z_{LO}). (b) The photonic crystal filter was hand fabricated by squashing sections of a coaxial transmission line to create a spatially periodic capacitive loading of an otherwise standard 50-Ω coaxial cable.

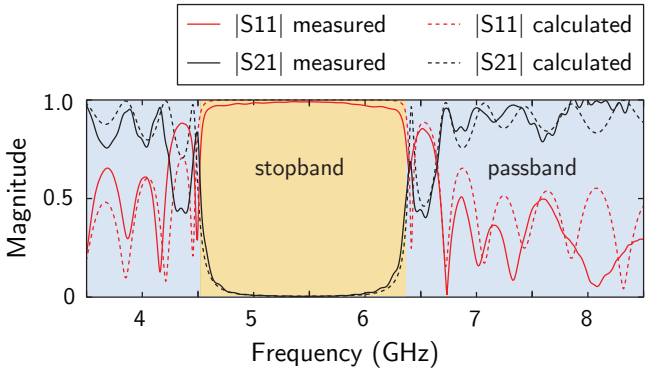

Figure 6.4: The scattering parameters of the photonic crystal filter were measured from a two-port 50-Ω calibrated vector network analyzer. We compare the measured reflection magnitude $|S_{11}|$ and transmission magnitude $|S_{21}|$ to those calculated from cascaded $ABCD$ transfer matrices of the transmission line sections which consitute the photonic crystal.

We fabricate a photonic crystal from a coaxial transmission line by 25 discrete impedance steps ($Z_{\mathrm{LO}} = 30\,\Omega$, $Z_{\mathrm{HI}} = 50\,\Omega$), resulting in the opening of a band gap (Fig. 6.3) [223]. The photonic crystal was hand fabricated (Fig. 6.3) from a 50-Ω semi-rigid transmission line (Micro-Coax UT-085C-TP-LL). Since the (quasi-)TEM propagation mode geometry determines the characteristic impedance of the transmission line, sections of the transmission line geometry were mechanically deformed by crushing the coax, creating lengths of characteristic impedance $Z_0 \simeq 30\,\Omega$, which were found to be consistent with Ansys High Frequency Electromagnetic Field Simulation Software (HFSS) simulation.

The photonic crystal was modeled as a Chebyshev type-I bandstop filter in AWR Microwave Office. Given prior knowledge that squashed transmission line sections have $\simeq$ 30-Ω characteristic impedance and the dielectric constant of the transmission line ($\epsilon_{\mathrm{r}} \simeq 2$ for polytetrafluoroethylene), the lengths of the transmission line sections were modeled in AWR Microwave Office and optimized for an experimentally convenient frequency of the upper band edge.

We measured the photonic crystal scattering parameters at room temperature with a vector network analyzer calibrated with Short-Open-Load-Thru standards. In Figure 6.4, we show the magnitude of the scattering parameter measurements are well matched to scattering parameters calculated, given the lengths in Table B.1 (Appendix B) and a minor adjustment to the transmission line dielectric constant ($\epsilon = 1.96$). The calculation of the photonic crystal scattering parameters were performed in MATLAB using cascaded $ABCD$ transfer matrices of transmission line sections.

The phase of the scattering parameter for transmission $\arg(\mathrm{S}_{21})$ provides information

of the photonic crystal density of states. In particular, the density of photonic states at a given frequency is

$$\rho_{\mathrm{DOS}}(\omega) = -\frac{dk(\omega)}{d\omega}, \tag{6.2.1}$$

where $k(\omega)$ is the wave vector of the photonic crystal. The photonic crystal itself is a medium for the propagation of electromagnetic waves, such that it can be considered a finite length transmission line. The amplitude of fixed frequency signal transmitted through the photonic crystal is

$$\mathrm{S}_{21} = e^{ik(\omega)\ell}, \tag{6.2.2}$$

where ℓ is the length of the transmission line. Therefore, the phase of Eq. 6.2.2, encodes the effective propagation constant of photonic crystal. Figure 6.5 shows the photonic crystal band structure and density of states.

6.3 A qubit coupled to a photonic crystal

6.3.1 Experiment setup

This experiment comprises a transmon-type superconducting qubit [66, 116] coupled to a one-dimensional photonic crystal. The transmon junction has a SQUID geometry which allows for tuning of its resonant frequency. The transmon circuit is placed inside a waveguide cavity with a $\omega_r/2\pi = 7.801\,\mathrm{GHz}$ resonance of its fundamental mode (Fig. 6.6). The cavity has an antenna port for applying drive pulses to the qubit and a second antenna port that is relatively strongly coupled to the coaxial transmission line photonic crystal.

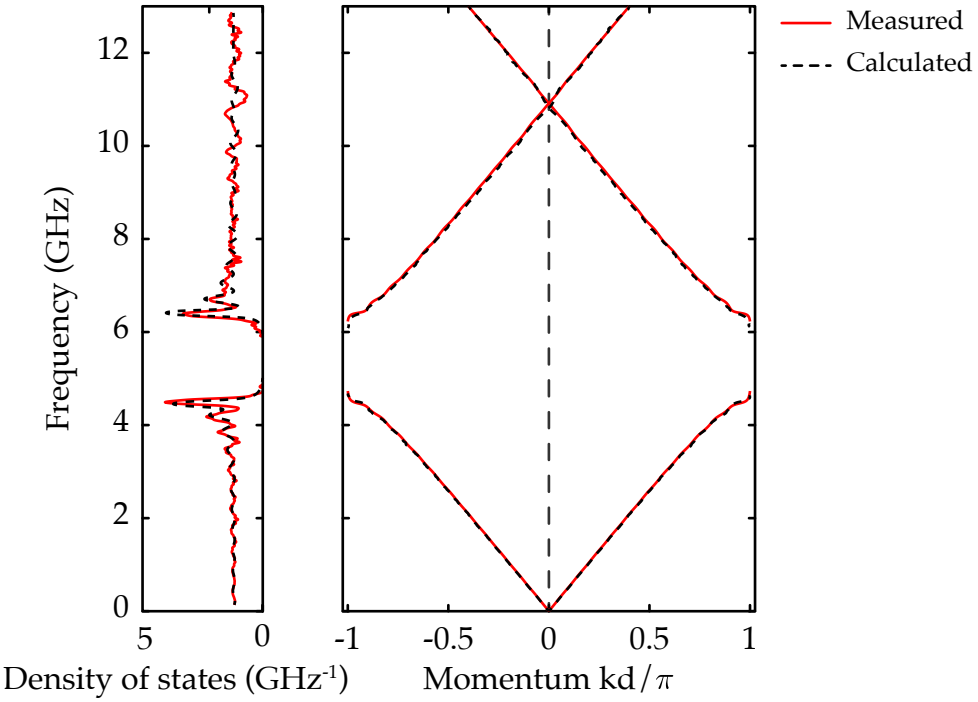

Figure 6.5: The photonic crystal band structure and density of states. The density of state is greatest near the edge of the photonic crystal stop band, where a light of a given energy can propagate in many photonic modes.

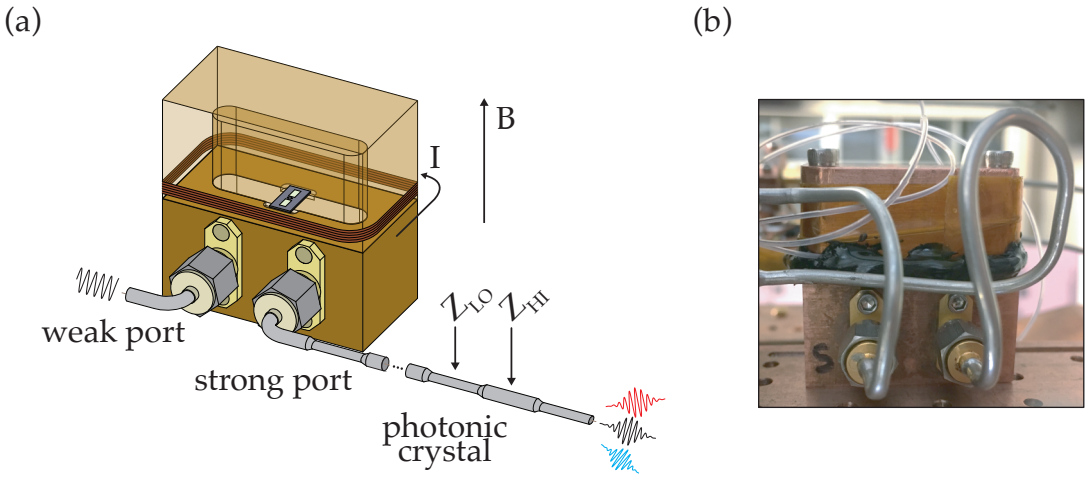

Figure 6.6: (a) A transmon circuit is dispersively coupled to a copper waveguide cavity. The dispersively coupled cavity resonator is effectively a capacitive filter between the transmon and the photonic crystal enironment. (b) The 3D transmon cavity mounted to the cryostat sample holder.

The finite length photonic crystal is connected to the 50-Ω electromagnetic environment of the microwave readout chain.

The transmon, copper cavity, and photonic crystal were attached to an oxygen free high purity copper (OFHC) mount, thermalized to the mixing chamber plate of a BlueFors LD250 dilution refrigerator. The cavity and photonic crystal were shielded from thermal radiation and stray magnetic fields by an indium sealed OFHC box placed inside a Cryoperm can. We illustrate the microwave components of the experimental setup in Fig. 6.7, including transmission line attenuation and filtering. The microwave measurement setup (Fig. 6.7) has a circulator placed between the photonic crystal and the microwave readout amplifier, enabling measurement by microwave signal reflection. Additionally, the microwave cavity has a relatively weakly coupled antenna port, for applying drive pulses to the qubit.

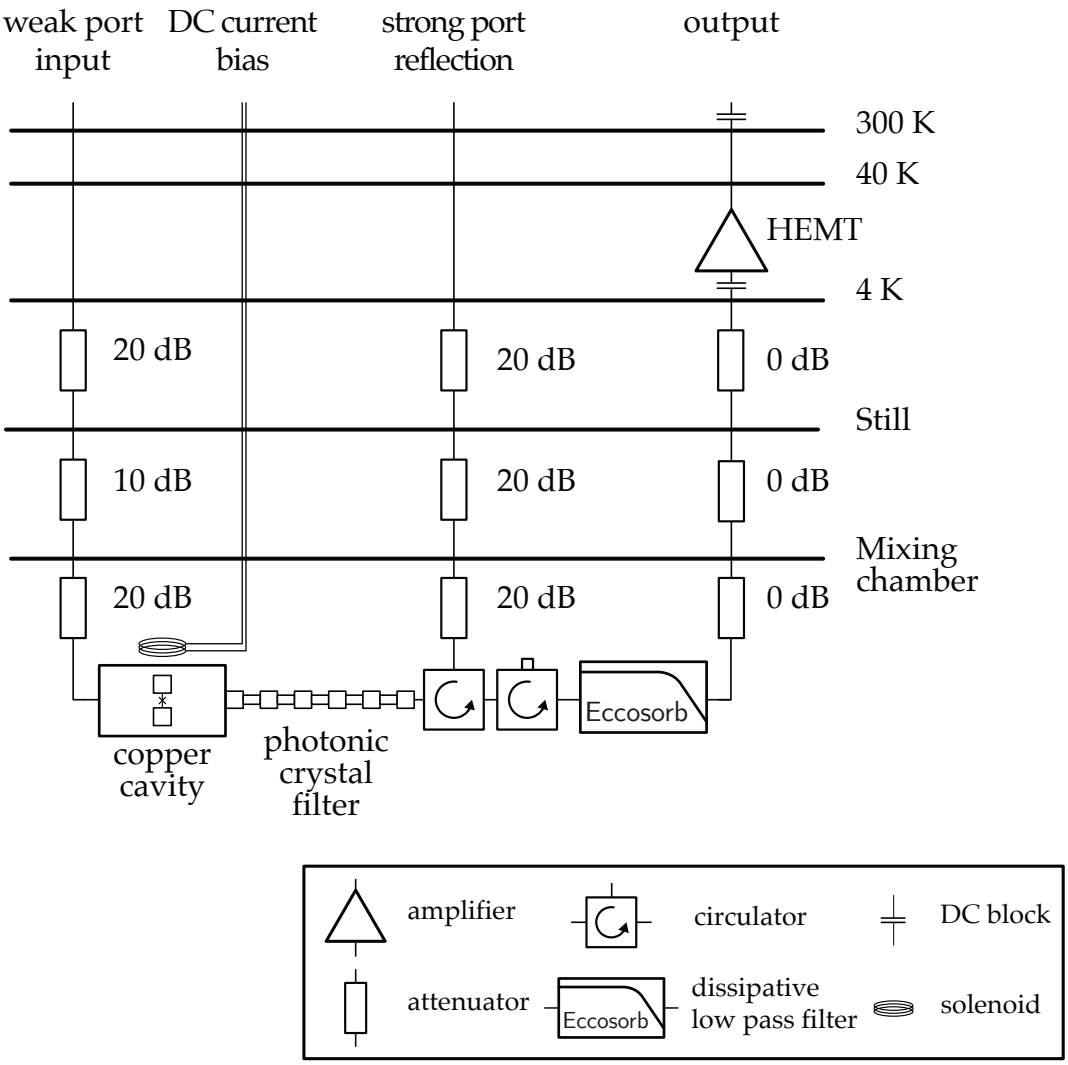

Figure 6.7: The transmon, copper cavity, and photonic filter were placed inside a sealed copper box thermalized to the 10 mK mixing chamber plate.

6.3.2 Purcell decay

The decay of the transmon qubit strongly influenced by the presence of the photonic band gap, since the rate of spontaneous emission is proportional to the local density of states at the transition frequency of an emitter [219, 224]. In this experiment, the Purcell-limited qubit decay rate is moderated by its coupling to the cavity resonance. The schematic of Figure 6.8 displays the transmon, resonator, and environment as capacitively coupled lumped element circuits. The decay of the qubit is determined by the net admittance shunting the transmon at the qubit transition frequency [225]. For a qubit dispersively coupled to a resonator, we determine the qubit decay rate according to the density of states offered by the admittance shunting the resonator and the strength of the qubit-resonator coupling. In this way, the resonator is a Lorentzian filter between the transmon and the environment. The decay rate of a qubit dispersively coupled to a single cavity mode is [226, 227],

$$\gamma_1 = \gamma_\mathrm{d} + \rho(\omega_q)(g/\Delta_\mathrm{q})^2\kappa. \tag{6.3.1}$$

where $\kappa/2\pi = 18\,\mathrm{MHz}$ is the cavity linewidth, $g/2\pi = 200\,\mathrm{MHz}$ is the qubit-cavity coupling rate, $\Delta_\mathrm{q} = \omega_r - \omega_q$ is the qubit-cavity detuning, $\rho(\omega_q)$ is the local density of states at the qubit frequency, and γ_d is the qubit decay rate into other dissipation channels. We attribute any variation of the qubit decay rate to changes in the environment density of states of the photonic crystal.

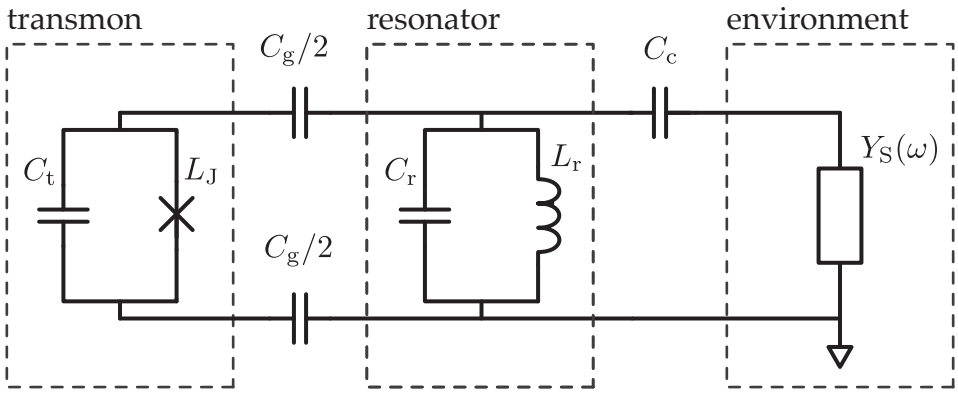

Figure 6.8: The 3D transmon is capacitively coupled to the fundamental mode of the waveguide cavity. The cavity resonator is then capacitivly coupled to the 50-Ω microwave readout chain through the photonic crystal, which are depected as a frequency dependent admittance.

6.3.3 Qubit state readout and tomography

The qubit-cavity dispersive coupling enables single shot readout using the Jaynes-Cummings nonlinearity technique at the bare cavity resonance [228]. We use this to conduct full quantum state tomography of the qubit and characterize the bath engineering decay process. Readout is performed by driving the strongly coupled port of the cavity through the photonic crystal. At a critical drive power the threshold behavior of this readout technique is observed in the phase shift of the reflection tone, achieving a readout fidelity of $\mathcal{F} = 0.8$, amenable to qubit state tomography. To account for this non-ideal readout fidelity, we calibrate tomography measurements by preparing eigenstates of $\langle\sigma_x\rangle$, $\langle\sigma_y\rangle$, and $\langle\sigma_z\rangle$, measuring their expectation values, and rescaling experimental expectation values accordingly.

6.3.4 Characterizing the spectral density of states

We characterize the environment spectral density of states before implementing a bath engineering protocol for energy selective decay. Since the interaction of the qubit and the photonic crystal is determined by the spectral density of states at the qubit resonance, we perform experiments across a frequency range by flux tuning the qubit resonance. The photonic crystal density of states should determine the rate of qubit decay and the rate of photon absorption through the photonic crystal. We use the qubit decay rate and the coupling strength to a resonant coherent drive to verify the qubit decay rate is determined by the photonic crystal density of states. The qubit decay rates and Rabi frequency measurements are extracted from qubit state readout on time varied measurement sequences illustrated in Figure 6.9.

We characterize the spectral density of states by first performing standard energy relaxation measurements (Fig. 6.9a). We determine the qubit energy relaxation rate γ_1 for a range of qubit transition frequencies by adjusting the flux bias on the transmon circuit between sets of measurement. To verify that the measured qubit decay is in fact influenced by the local density of states of the photonic crystal, we additionally investigate variations of the coupling rate between the qubit and its photonic crystal environment. At each flux bias, we perform resonant Rabi frequency measurements from a drive of a fixed amplitude applied through the photonic crystal (Fig. 6.9b). Similar to qubit decay, variation of the Rabi oscillation frequency is attributed to the rates of qubit absorption and emission, which are due to the spectral density of states of the photonic crystal.

We find agreement in the proportional changes of the qubit decay rate γ_1 and the Rabi

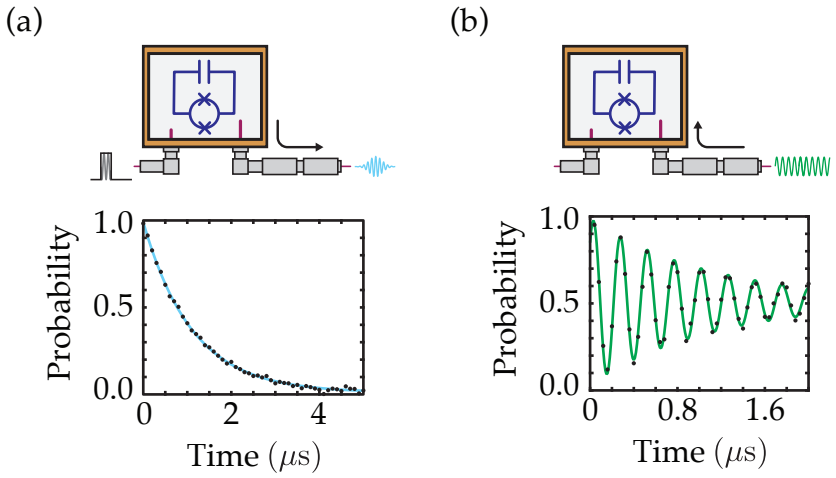

Figure 6.9: At a given transmon flux bias we perform a measurement of the qubit decay rate and we measure the frequency of Rabi oscillations for a resonant drive of fixed amplitude for each flux bias.

frequency squared $(\Omega_R/2\pi)^2$ (Fig. 6.10). This establishes that the photonic crystal forms the spectral density of states for qubit emission and absorption, since both the qubit decay rate γ_1 and the squared Rabi frequency both depend proportionally on the local density of states. From this, we attribute changes of the qubit decay rate to the large variation of the local density of states between the stopband and passband of the photonic crystal.

6.4 Dressed state dissipation

6.4.1 The dynamics of dressed state dissipation

The dressed qubit basis

We apply a coherent drive on the qubit through the weakly coupled cavity port to implement the bath engineering protocol. The coherent drive, along with the photonic crystal spectral density of states, determines the steady state of the bath engineering process by

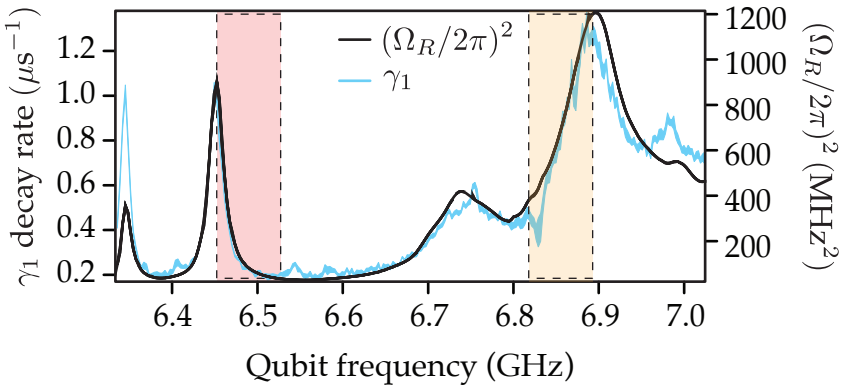

Figure 6.10: The qubit energy relaxation rate γ_1 (cyan trace) and the qubit Rabi frequency squared $(\Omega_R/2\pi)^2$ (black trace) versus the qubit resonance frequency $\omega_q/2\pi$. The qubit decay rate and Rabi frequency resulting from a resonant drive applied through the photonic crystal both indicate the frequency dependent coupling to the environment. The width of the data traces represents the standard error based on nine separate measurements. The outlined and shaded regions indicate the the local density of states for the measurements of Section 6.4.2 (yellow) and Section 6.4.2 (red).

inducing specific decay transitions of the qubit [229]. We solve for this steady state by considering the system dynamics under drive and decay.

The bare qubit with an energy eigenbasis $\{|g\rangle, |e\rangle\}$ is described by the Hamiltonian $H = -\omega_q\sigma_z/2$ in the laboratory frame. When the qubit is dipole coupled to a coherent drive of frequency ω_d, we transform the laboratory frame Hamiltonian of the driven qubit $H = -\omega_q\sigma_z/2 + \Omega\sigma_x\cos(\omega_d t)$ into the rotating frame of the drive with the unitary operator $U = e^{-i\omega_d t\sigma_z/2}$ as $H \rightarrow UHU^\dagger + i\dot{U}U^\dagger$. The rotating frame Hamiltonian is

$$H_q = \frac{\Delta}{2}\sigma_z + \frac{\Omega}{2}\sigma_x \tag{6.4.1}$$

upon neglecting rapidly oscillating terms and where $\Delta = \omega_d - \omega_q$ is the qubit-drive detuning and Ω is the frequency of Rabi oscillations in the case of a resonant drive. We

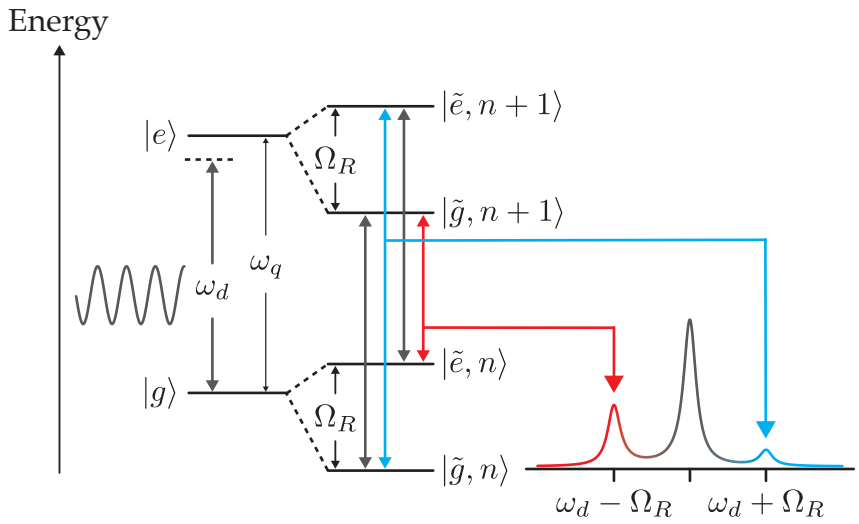

Figure 6.11: The emitter, dressed by a coupling to the light field, has an emission spectrum known as the Mollow triplet. The Mollow triplet takes on an asymmetric character in the presence of an off-resonant drive or when the local density of states of the driven emitter enhances one of the sideband transitions.

diagonalize Eq. 6.4.3 to find the dressed energy eigenstates,

$$\begin{aligned} |\tilde{g}\rangle &= \cos(\theta)\,|g\rangle - \sin(\theta)\,|e\rangle \\ |\tilde{e}\rangle &= \sin(\theta)\,|g\rangle + \cos(\theta)\,|e\rangle\,, \end{aligned} \tag{6.4.2}$$

where $\tan 2\theta = -\Omega/\Delta$ and $0 \leq \theta < \pi/2$. We define the energy eigenstates such that $|\tilde{g}\rangle \simeq |g\rangle$ when the qubit is driven far-red detuned and $|\tilde{e}\rangle \simeq |g\rangle$ when the qubit is driven far-blue detuned. We rewrite the Hamiltonian in the dressed state basis as,

$$H_q = \frac{\Omega_R}{2}\tilde{\sigma}_z \tag{6.4.3}$$

where $\Omega_R = \sqrt{\Omega^2 + \Delta^2}$ and $\tilde{\sigma}_z = \sin(2\theta)\sigma_x - \cos(2\theta)\sigma_z$.

Dissipation of dressed states

We now consider the interaction picture of the driven qubit weakly coupled to a dissipative environment, such that we can treat the interaction as a perturbation. The driven qubit interacting with dissipative modes of the electromagnetic environment is described by the interaction Hamiltonian in the rotating frame of the drive,

$$H_{int} = \sum_k g_k(\sigma {b_k}^\dagger e^{i\Delta_k t} + h.c.) \tag{6.4.4}$$

where g_k is the coupling strength to the electromagnetic mode of frequency $\omega_k = \Delta_k - \omega_d$ with creation operator ${b_k}^\dagger$. Each term of the interaction Hamiltonian can be expressed in terms of dressed state operators as,

$$\begin{aligned} H_{int}^k = g_k(&\cos^2(\theta)\tilde{\sigma} - \sin^2(\theta)\tilde{\sigma}^\dagger \\ &+ \sin(\theta)\cos(\theta)\tilde{\sigma}_z){b_k}^\dagger e^{i\Delta_k t} + h.c. \end{aligned}$$

where we have simply made the substitution

$$\sigma = \cos^2(\theta)\tilde{\sigma} - \sin^2(\theta)\tilde{\sigma}^\dagger + \sin(\theta)\cos(\theta)\tilde{\sigma}_z. \tag{6.4.5}$$

We transform both the qubit and interaction Hamiltonian into the rotating frame of the dressed qubit described by the transformation $H \to UHU^\dagger + i\dot{U}U^\dagger$ where

$$U = \exp\left(i\frac{\Omega_R}{2}\tilde{\sigma}_z\right) \tag{6.4.6}$$

which gives the time-dependent Hamiltonian,

$$H(t) = \sum_k g_k(\cos^2(\theta)\tilde{\sigma}e^{i(\Delta_k+\Omega_R)t} - \sin^2(\theta)\tilde{\sigma}^\dagger e^{i(\Delta_k-\Omega_R)t} + \sin(\theta)\cos(\theta)\tilde{\sigma}_z e^{i\Delta_k t}){b_k}^\dagger + h.c. \tag{6.4.7}$$

As we consider the time evolution of both the qubit and dissipative environment in the interaction picture, we assume the environment modes are sufficiently dissipative, such that we can make the Born approximation and trace out the environment degrees of freedom [128]. We subsequently make the Markov approximation, and assume time evolution is coarse grained enough for the environment local density of states to determine jump rates of the open system dynamics [112, 230–233]. The time evolution for the reduced density matrix of the qubit is described by the Lindblad master equation [234]. We include the unitary dynamics of Eq. 6.4.3 in the following master equation to make reference to the time evolution of tomography measurements in experiment:

$$\dot{\rho} = -i[\Omega_R\tilde{\sigma}_z/2, \rho] + \gamma_-\mathcal{D}[\sin^2(\theta)\tilde{\sigma}^\dagger]\rho + \gamma_+\mathcal{D}[\cos^2(\theta)\tilde{\sigma}]\rho + \gamma_0\mathcal{D}[\sin(\theta)\cos(\theta)\tilde{\sigma}_z]\rho, \tag{6.4.8}$$

where $\mathcal{D}[L]\rho = 2(L\rho L^\dagger - L^\dagger L\rho - \rho L^\dagger L)/2$, $\gamma_- = 2\pi\sum_k g_k^2\delta(\omega_k - (\Delta_k - \Omega_R))$, $\gamma_+ = 2\pi\sum_k g_k^2\delta(\omega_k - (\Delta_k + \Omega_R))$, and $\gamma_0 = 2\pi\sum_k g_k^2\delta(\omega_k - \Delta_k)$.

Emission of the driven system creates field correlations that manifest as the Mollow triplet emission spectrum (Fig. 6.11). The joint eigenbasis of the qubit and coherent drive field is an infinite ladder of dressed states connected by single photon transitions. Inelastic

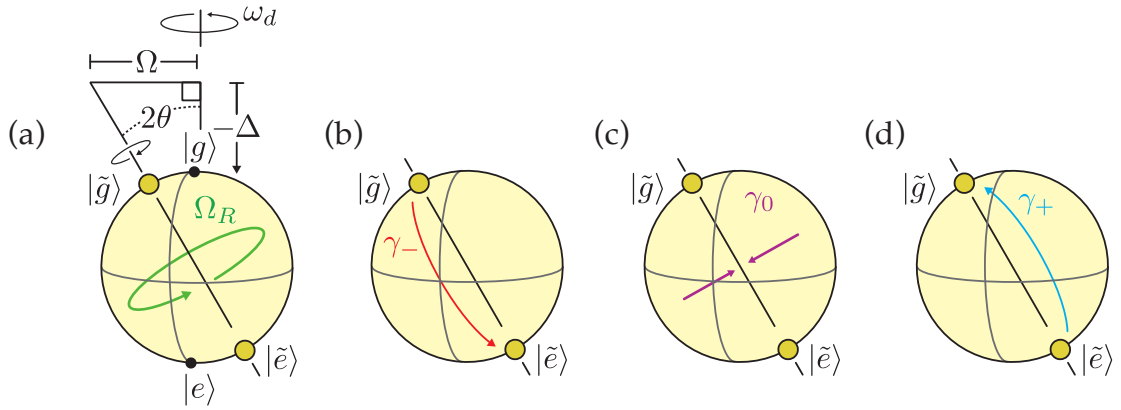

Figure 6.12: (a) The dressed qubit eigenstates evolve in a frame rotating at the drive frequency relative to the laboratory frame. Superpositions of the dressed qubit eigenstates states evolve at the generalized Rabi frequency along a tilted axis in the Bloch sphere representing the bare qubit eigenstates. The dissipation dynamics of the dressed qubit include (b) jump transitions in which the qubit absorbs energy from the field $|\tilde{g}\rangle \rightarrow |\tilde{e}\rangle$, (c) dephasing in the dressed basis, and (d) jump transitions in which the qubit emits energy into the field $|\tilde{e}\rangle \rightarrow |\tilde{g}\rangle$.

transitions between dressed basis eigenstates of the qubit result in the two sidebands of the Mollow triplet [235]. An asymmetry in jump transition decay rates $\gamma_- \neq \gamma_+$ results in an asymmetry of the Mollow triplet emission power spectral density [236–238]. In an ideal scenario for qubit state stabilization, the Mollow triplet spectrum would have only a single sideband since a thoroughly dissimilar local density of states at frequencies $\omega_d \pm \Omega_R$ would cause deterministic decay to only one of the two dressed states.

The dynamics of Eq. 6.4.8 are depicted in Figure 6.12. After sufficiently long time evolution of Eq. 6.4.8, the qubit relaxes to a nonequilibrium effective ground state: a steady state of the driven-dissipative dynamics [239]. Importantly, a superposition state results from an asymmetry in transition rates $\tilde{\sigma}_\pm$ between the dressed states, due to the frequency dependence of the photonic density of states.

Numerical calculation of Lindblad dynamics

Numerical calculations were performed in the dressed state basis including unitary evolution from Rabi oscillations described by the master equation (Eq. 6.4.8) with an additional pure dephasing term with decay rate γ_ϕ in the laboratory frame of the qubit. The density matrix time evolution was numerically solved by recasting the Lindblad superoperator into a 4×4 matrix which maps a vector representation of the density matrix to another vector. The qubit density matrix is expressed as the column vector, $\vec{\rho} = (\rho_{gg}, \rho_{ge}, \rho_{eg}, \rho_{ee})^T$. We construct the Lindblad operator $\mathcal{L}$ as a matrix in operator space by expressing left-operation ($A\rho$) and right-operation (ρA) on the density matrix with tensor products. Matrices of left- and right- operation are

$$A\rho \rightarrow (\mathbb{I} \otimes A)\vec{\rho} = \begin{pmatrix} A_{11} & A_{12} & 0 & 0 \\ A_{21} & A_{22} & 0 & 0 \\ 0 & 0 & A_{11} & A_{12} \\ 0 & 0 & A_{21} & A_{22} \end{pmatrix},$$

and,

$$\rho A \rightarrow (A \otimes \mathbb{I})\vec{\rho} = \begin{pmatrix} A_{11} & 0 & A_{12} & 0 \\ 0 & A_{11} & 0 & A_{12} \\ A_{21} & 0 & A_{22} & 0 \\ 0 & A_{21} & 0 & A_{22} \end{pmatrix}.$$

Time evolution from an initial qubit state is calculated from the equation, $\vec{\rho}(t) = e^{\mathcal{L}t}\vec{\rho}(0)$, where we perform matrix exponentiation of $\mathcal{L}t$ by finding the matrix V which diagonalizes

the Lindblad matrix. After converting the density matrix vector into a matrix operator ($\vec{\rho}(t) \rightarrow \rho_t$), we then calculate expectation values in the laboratory frame rotating with the drive,

$$\langle \sigma_x \rangle_t = \mathrm{tr}(\sigma_x \rho), \quad \langle \sigma_y \rangle_t = \mathrm{tr}(\sigma_y \rho), \quad \langle \sigma_z \rangle_t = \mathrm{tr}(\sigma_z \rho),$$

where the Pauli operators, in terms of the dressed state basis, are $\sigma_x = \cos(2\theta)\tilde{\sigma}_x - \sin(2\theta)\tilde{\sigma}_z$, $\sigma_y = \tilde{\sigma}_y$, and $\sigma_z = \sin(2\theta)\tilde{\sigma}_x + \cos(2\theta)\tilde{\sigma}_z$.

6.4.2 Tomography of dressed state dissipation

Time evolution of dressed state decay

We demonstrate the bath engineering protocol in the time domain driving the qubit transition with a nearly resonant Rabi drive for a long duration compared to the decay rates of the dressed qubit state. The qubit transition is flux biased near 6.85 GHz (Fig. 6.10, yellow region) where there is a strong asymmetry in the spectral density of states. Beginning with the qubit in the ground state for each experiment, the qubit was driven for a variable amount of time before tomography pulses and state readout. Qubit state tomography (Fig. 6.13) shows the expectation values $\langle \sigma_y \rangle$ and $\langle \sigma_z \rangle$, which are coherences in the dressed qubit eigenbasis, undergo dephasing. However, the expectation value of $\langle \sigma_x \rangle$ demonstrates relaxation to state of nonzero purity at long times. From the bath engineering protocol, the qubit is effectively "cooled" to a superposition state in the bare qubit eigenbasis.

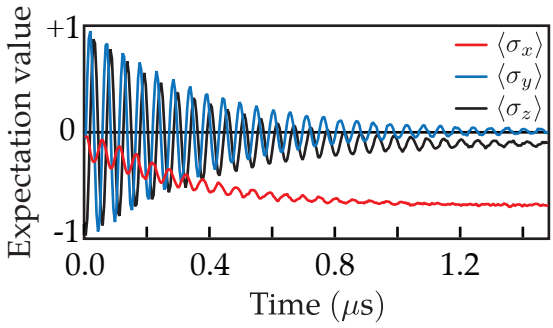

Figure 6.13: Time evolution of qubit expectation values in the bare qubit eigenbasis. The qubit is initialized in the ground state before applying a near resonant drive dipole-coupled to the qubit σ_x operator. At long times, the qubit is stabilized to a superposition state in the bare qubit eigenbasis.

Steady state tomography

Since, at long times, the qubit stabilizes to a steady state of the driven conditions, the now characterize dependence of the stabilized state for a range of Rabi frequencies and qubit-drive detuning values. We demonstrate bath engineering decay to a dressed state by flux tuning the qubit to $\omega_q/2\pi = 6.4766\,\text{GHz}$ where the local density of states varies dramatically, as shown in Fig. 6.10. In Fig. 6.14, we display the measured steady state qubit coherence $\langle X\rangle_{\text{ss}} \equiv \text{Tr}(\rho_{\text{ss}}\sigma_x)$, where ρ_{ss} is the tomographically reconstructed qubit state after $15.95\,\mu\text{s} \gg 1/\gamma_\pm$ of driving and σ_x is the Pauli operator in the undressed basis.

Here, we observe two signatures of the photonic crystal density of states. First, we find that the steady states mapped in Figure 6.14 contain a feature of zero coherence (black dashed line) for certain coherent drive parameters of detuning and amplitude. This occurs when the two terms $\gamma_\pm$ in Eq. 6.4.8 cancel due to the dependence of both θ and $\gamma_\pm$ on Δ and Ω. A maximally mixed steady state is a consequence of equal transition rates between dressed states (Fig. 6.15). Physically, the overlap of the dressed states with the

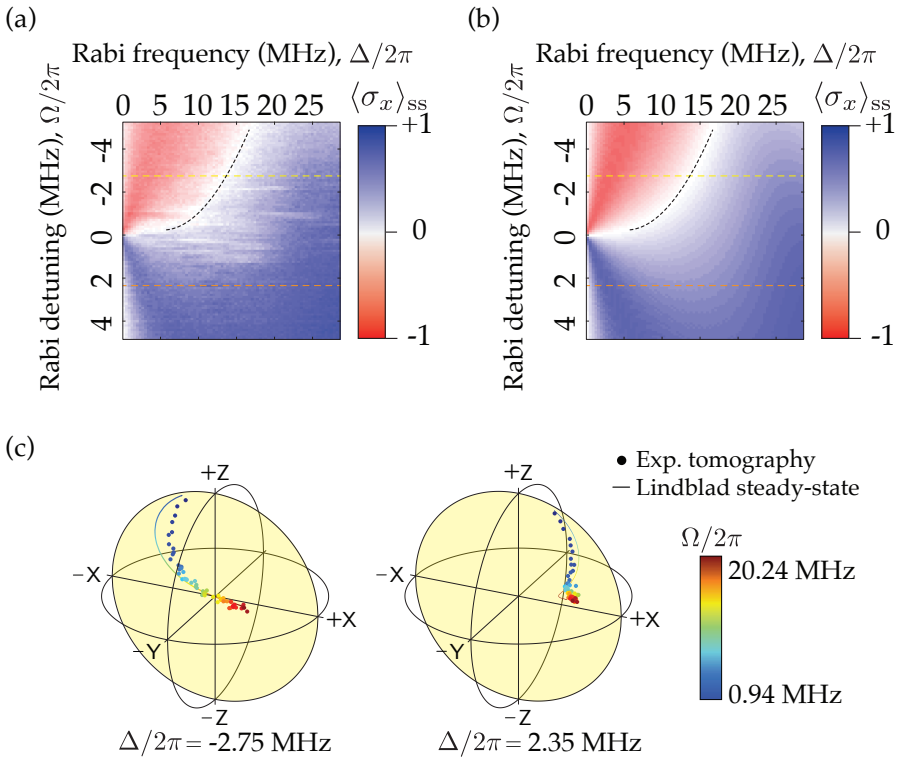

Figure 6.14: (a) The steady state coherence $\langle X\rangle_{ss}$ for a range of Rabi drive amplitudes and detunings. The black dashed line indicates drive parameters that give a steady state of zero coherence determined by the decay rates given by measurements in Fig. 6.10 Eq. 6.4.9. (b) The calculated $\langle X\rangle_{ss}$ based on Eq. 6.4.8 and the experimental driving parameters. The black dashed line indicates the same drive parameters as in panel (a). (c) The Bloch sphere representation of the calculated and measured qubit steady state, $\vec{r} = \mathrm{Tr}(\rho_{ss}\vec{\sigma})$, for the drive detuning $\Delta/2\pi = -2.75\,\mathrm{MHz}$ (yellow dashed line in panels (a) and (b)), and $\Delta/2\pi = 2.35\,\mathrm{MHz}$ (orange dashed line in panels (a) and (b)).

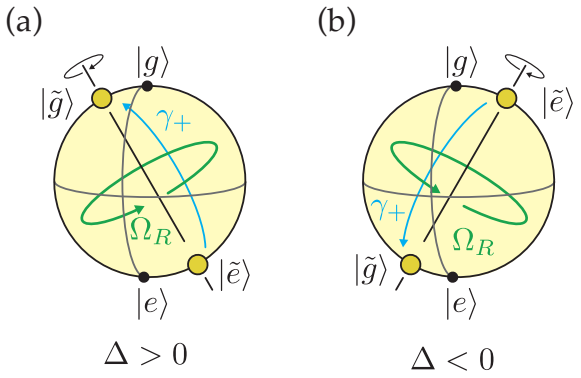

Figure 6.15: For this illustration, we consider the $\tilde{\sigma}$ dissipation process at rate γ_+ to be favored over the $\tilde{\sigma}^\dagger$ dissipation process due to an asymmetry of the environment density of states. (a) When the drive is blue-detuned from the qubit transition, the dressed qubit dissipates toward a ground-like state, assisted from the asymmetry of the environment density of states. (b) For a red-detuned drive, the effective rates of the $\tilde{\sigma}$ and the $\tilde{\sigma}^\dagger$ transition cancel, because the environment density of states inhibits ground-like state decay.

globally favored ground state competes with the dressed state favored by $\gamma_\pm$. In a picture of detailed balance for the rate of transitions between dressed states, this occurs for drive parameters satisfying the relation

$$\gamma_-(\Omega, \Delta) \sin^4(\theta) = \gamma_+(\Omega, \Delta) \cos^4(\theta), \tag{6.4.9}$$

which was used to calculate the dashed lines of Figure 6.14.

A second signature of the photonic crystal is observed by the increase of the steady state coherence for a resonant drive. Although this coherence is limited in our experiment by decay to other dissipation channels, we find an overall increase of steady state coherence because the dressed state transition rates become more asymmetric as the Mollow triplet spectrum widens in the presence of a colored local density of states. While small coherences can be created from a weak drive in resonance fluorescence [240], the observa-

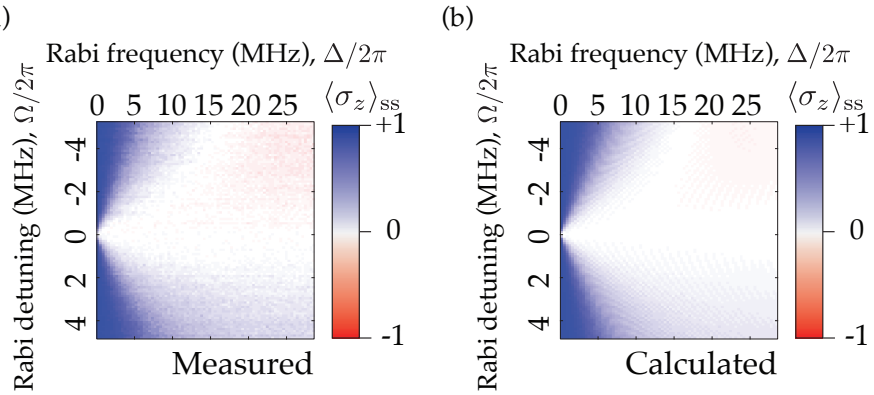

Figure 6.16: Tomographic measurements of the qubit expectation value $\langle\sigma_z\rangle$ after 15.95 μs of drive. The phase of tomography pulses were chosen to be in the rotating frame of the drive, thus $\langle\sigma_y\rangle_{ss} = 0$ and all states lie in the X-Z plane of the Bloch sphere.

tion of coherence from a strong drive is a clear indicator of an asymmetry in the rates $\gamma_\pm$ due to the density of state of the photonic crystal. Furthermore, we note that the asymmetric density of states of the readout cavity is negligible due to its large detuning from the qubit resonance $\Omega, \Delta \ll \Delta_q$.

The quantum state tomography for the qubit populations $\langle Z\rangle_{ss}$ in Fig. 6.16. We find the calculated $\langle Z\rangle_{ss}$ agrees well with the measurement quantum state tomography from experiment.

Consequently, we find that the qubit is "cooled" to a chosen superposition state in the eigenbasis of the undriven qubit from a proper selection of a drive phase, frequency, and amplitude (Fig. 6.14), enabled by the asymmetric density of states of the photonic crystal. The theory colormap of Figure 6.14b was produced by solving for the steady states of Eq. 6.4.8 given the local density of states as inferred from measurements shown in Fig. 6.10. This theory reproduces all qualitative features of the tomography results and has quantitative agreement when including additional pure dephasing of the qubit tran-

sition $\gamma_\phi = 0.029\,\mu\text{s}^{-1}$, consistent with typical limits of coherence for transmon qubits. In conclusion, we have shown that the driven and dissipative dynamics of a transmon qubit weakly coupled to a photonic crystal can be used for quantum bath engineering, as we have verified with full state tomography. Our protocol robustly prepares a desired qubit superposition state, realized as an effective ground state of the driven-dissipative system. The colored density of states introduced from the photonic crystal is crucial for our method and highlights impedance engineering of the electromagnetic environment as a key aspect of bath engineering for circuit quantum electrodynamics. In future bath engineering implementations, the photonic density of states can be tailored by fabrication techniques with lumped element metamaterials [223] and in situ tunability of coupling rates between photonic modes [92, 241]. Additionally, quantum monitoring of dissipative photonic modes of the environment can further the scope of bath engineering protocols for nonunitary heralding of quantum states and quantum control by dynamical feedback [87, 138–140, 242–245].

Bibliography

[1] A. O. Leggett. Prospects in ultralow temperature physics. J. Phys. Colloques **39**, 1264 (1978). Cited on page 1

[2] A. J. Leggett. Macroscopic quantum systems and the quantum theory of measurement. Progress of Theoretical Physics Supplement **69**, 80 (1980). Cited on pages 1 and 12

[3] E. Schrödinger. Die gegenwärtige Situation in der Quantenmechanik. Naturwissenschaften **23**, 807 (1935). Cited on page 1

[4] J. D. Trimmer. The present situation in quantum mechanics: A translation of Schrödinger's "cat paradox" paper. Proceedings of the American Philosophical Society **124**, 323 (1980). Cited on page 1

[5] F. London, E. Bauer. La théorie de l'observation en mécanique quantique [The theory of observation in quantum mechanics]. In J. A. Wheeler, W. H. Zurek (editors), *Quantum Theory and Measurement*, 217–259. Princeton University (1983). Cited on page 1

[6] J. von Neumann. *Mathematische Grundlagen der Quantenmechanik [Mathematical Foundations of Quantum Mechanics]*. Springer, Berlin (1932). Cited on page 1

[7] J. von Neumann, R. T. Beyer. *Mathematical Foundations of Quantum Mechanics*. Goldstine Printed Materials. Princeton University Press (1955). Cited on page 1

[8] H. S. Green. Observation in quantum mechanics. Nuovo Cim **9**, 880 (1958). Cited on page 1

[9] W. Pauli, P. Achuthan, K. Venkatesan. *General Principles of Quantum Mechanics*. Springer-Verlag Berlin Heidelberg (1980). Cited on page 1

[10] M. Born, G. Ludwig. Zur Quantenmechanik des kräftefreien Teilchens [Quantum mechanics of force free particles]. Zeitschrift für Physik A Hadrons and Nuclei **150**, 106 (1958). Cited on page 1

[11] G. Ludwig. Der Meßprozeß [The measurement process]. Zeitschrift für Physik A Hadrons and Nuclei **135**, 483 (1953). Cited on page 1

[12] G. Ludwig. Zum Ergodensatz und zum Begriff der makroskopischen Observablen [Ergodic principle and the concept of macroscopic observables]. Zeitschrift für Physik A Hadrons and Nuclei **152**, 98 (1958). Cited on page 1

[13] A. Daneri, A. Loinger, G. M. Prosperi. Quantum theory of measurement and ergodicity conditions. Nuclear Physics **33**, 297 (1962). Cited on page 1

[14] A. Daneri, A. Loinger, G. M. Prosperi. Further remarks on the relations between statistical mechanics and quantum theory of measurement. Nuovo Cimento B Series **44**, 119 (1966). Cited on page 1

[15] H. D. Zeh. On the interpretation of measurement in quantum theory. Foundations of Physics **1**, 69 (1970). Cited on page 1

[16] H. D. Zeh. Toward a quantum theory of observation. Foundations of Physics **3**, 109 (1973). Cited on page 1

[17] E. Joos, H. D. Zeh. The emergence of classical properties through interaction with the environment. Zeitschrift fur Physik B Condensed Matter **59**, 223 (1985). Cited on page 1

[18] M. Simonius. Spontaneous symmetry breaking and blocking of metastable states. Phys. Rev. Lett. **40**, 980 (1978). Cited on page 1

[19] W. H. Zurek. Pointer basis of quantum apparatus: Into what mixture does the wave packet collapse? Phys. Rev. D **24**, 1516 (1981). Cited on page 1

[20] W. H. Zurek. Environment-induced superselection rules. Phys. Rev. D **26**, 1862 (1982). Cited on page 1

[21] W. H. Zurek. Decoherence, einselection, and the quantum origins of the classical. Rev. Mod. Phys. **75**, 715 (2003). Cited on page 1

[22] P. C. E. Stamp. The decoherence puzzle. Studies in History and Philosophy of Science Part B: Studies in History and Philosophy of Modern Physics **37**, 467 (2006). Cited on page 2

[23] Y. M. Ivanchenko, L. A. Zil'berman. The Josephson effect in small tunnel contacts. JETP **28**, 1272 (1969). Cited on page 2

[24] A. O. Caldeira, A. J. Leggett. Influence of dissipation on quantum tunneling in macroscopic systems. Phys. Rev. Lett. **46**, 211 (1981). Cited on page 2

[25] R. J. Prance, A. P. Long, T. D. Clark, A. Widom, J. E. Mutton, J. Sacco, M. W. Potts, G. Megaloudis, F. Goodall. Macroscopic quantum electrodynamic effects in a superconducting ring containing a Josephson weak link. Nature **289**, 543 (1981). Cited on page 2

[26] M. Büttiker, E. P. Harris, R. Landauer. Thermal activation in extremely underdamped Josephson-junction circuits. Phys. Rev. B **28**, 1268 (1983). Cited on page 2

[27] A. J. Leggett. Quantum tunneling in the presence of an arbitrary linear dissipation mechanism. Phys. Rev. B **30**, 1208 (1984). Cited on page 2

[28] L. D. Jackel, W. W. Webb, J. E. Lukens, S. S. Pei. Measurement of the probability distribution of thermally excited fluxoid quantum transitions in a superconducting ring closed by a Josephson junction. Phys. Rev. B **9**, 115 (1974). Cited on page 2

[29] T. A. Fulton, L. N. Dunkleberger. Lifetime of the zero-voltage state in Josephson tunnel junctions. Phys. Rev. B **9**, 4760 (1974). Cited on page 2

[30] W. den Boer, R. de Bruyn Ouboter. Flux transition mechanisms in superconducting loops closed with a low capacitance point contact. Physica **98B**, 185 (1980). Cited on page 2

[31] L. D. Jackel, J. P. Gordon, E. L. Hu, R. E. Howard, L. A. Fetter, D. M. Tennant, R. W. Epworth, J. Kurkijärvi. Decay of the zero-voltage state in small-area, high-current-density Josephson junctions. Phys. Rev. Lett. **47**, 697 (1981). Cited on page 2

[32] R. F. Voss, R. A. Webb. Macroscopic quantum tunneling in 1-μm Nb Josephson junctions. Phys. Rev. Lett. **47**, 265 (1981). Cited on page 2

[33] D. W. Bol, R. van Weelderen, R. de Bruyn Ouboter. On the conditional transition probabilities of the magnetic flux at low temperatures in a superconducting loop closed with a low-capacitance superconducting point contact. Physica **122B**, 1 (1983). Cited on page 2

[34] M. H. Devoret, J. M. Martinis, D. Esteve, J. Clarke. Resonant activation from the zero-voltage state of a current-biased Josephson junction. Phys. Rev. Lett. **53**, 1260 (1984). Cited on page 2

[35] D. W. Bol, R. van Weelderen, R. de Bruyn Ouboter. Thermal activation in the quantum regime and macroscopic quantum tunnelling in the thermal regime in a metabistable system consisting of a superconducting ring interrupted by a weak junction: Part I: Thermal activation in the quantum regime. Physica **133B**, 196 (1985). Cited on page 2

[36] I. Dmitrenko, V. Khlus, G. Tsoi, V. Shnyrkov. Study of quantum decays of metastable current states in RF SQUIDs. Soviet Journal of Low Temperature Physics **11**, 77 (1985). Cited on page 2

[37] D. B. Schwartz, B. Sen, C. N. Archie, J. E. Lukens. Quantitative study of the effect of the environment on macroscopic quantum tunneling. Phys. Rev. Lett. **55**, 1547 (1985). Cited on page 2

[38] S. Washburn, R. A. Webb, R. F. Voss, S. M. Faris. Effects of dissipation and temperature on macroscopic quantum tunneling. Phys. Rev. Lett. **54**, 2712 (1985). Cited on page 2

[39] M. H. Devoret, J. M. Martinis, J. Clarke. Measurements of macroscopic quantum tunneling out of the zero-voltage state of a current-biased Josephson junction. Phys. Rev. Lett. **55**, 1908 (1985). Cited on page 2

[40] J. M. Martinis, M. H. Devoret, J. Clarke. Energy-level quantization in the zero-voltage state of a current-biased Josephson junction. Phys. Rev. Lett. **55**, 1543 (1985). Cited on page 2

[41] M. H. Devoret, D. Esteve, J. M. Martinis, A. Cleland, J. Clarke. Resonant activation of a Brownian particle out of a potential well: Microwave-enhanced escape from the zero-voltage state of a Josephson junction. Phys. Rev. B **36**, 58 (1987). Cited on page 2

[42] A. O. Caldeira, A. J. Leggett. Quantum tunnelling in a dissipative system. Annals of Physics **149**, 374 (1983). Cited on pages 2 and 11

[43] J. M. Martinis, M. H. Devoret, J. Clarke. Experimental tests for the quantum behavior of a macroscopic degree of freedom: The phase difference across a Josephson junction. Phys. Rev. B **35**, 4682 (1987). Cited on page 2

[44] E. Turlot, D. Esteve, C. Urbina, J. M. Martinis, M. H. Devoret, S. Linkwitz, H. Grabert. Escape oscillations of a Josephson junction switching out of the zero-voltage state. Phys. Rev. Lett. **62**, 1788 (1989). Cited on page 2

[45] P. Lafarge, P. Joyez, A. Cleland, T. Holst, D. Esteve, C. Urbina, M. H. Devoret. Direct observation of macroscopic charge quantization: a Millikan experiment in a submicron solid state device. C. R. Acad. Sci. Paris **t. 314**, 883 (1992). Cited on page 2

[46] M. H. Devoret, D. Esteve, H. Grabert, G.-L. Ingold, H. Pothier, C. Urbina. Effect of the electromagnetic environment on the Coulomb blockade in ultrasmall tunnel junctions. Phys. Rev. Lett. **64**, 1824 (1990). Cited on page 2

[47] P. Joyez, P. Lafarge, A. Filipe, D. Esteve, M. H. Devoret. Observation of parity-induced suppression of Josephson tunneling in the superconducting single electron transistor. Phys. Rev. Lett. **72**, 2458 (1994). Cited on page 2

[48] D. J. Flees, S. Han, J. E. Lukens. Interband transitions and band gap measurements in Bloch transistors. Phys. Rev. Lett. **78**, 4817 (1997). Cited on page 2

[49] Y. Nakamura, C. D. Chen, J. S. Tsai. Spectroscopy of energy-level splitting between two macroscopic quantum states of charge coherently superposed by Josephson coupling. Phys. Rev. Lett. **79**, 2328 (1997). Cited on page 2

[50] V. Bouchiat, D. Vion, P. Joyez, E. D., M. H. Devoret. Quantum coherence with a single Cooper pair. Physica Scripta **T76**, 165 (1998). Cited on page 2

[51] K. K. Likharev, A. B. Zorin. Theory of the Bloch-wave oscillations in small Josephson junctions. Journal of Low Temperature Physics **59**, 347 (1985). Cited on page 2

[52] M. Büttiker. Zero-current persistent potential drop across small-capacitance Josephson junctions. Phys. Rev. B **36**, 3548 (1987). Cited on page 2

[53] Y. Nakamura, Y. A. Pashkin, J. S. Tsai. Coherent control of macroscopic quantum states in a single-Cooper-pair box. Nature **398**, 786 (1999). Cited on page 2

[54] Y. Nakamura, Y. A. Pashkin, J. S. Tsai. Rabi oscillations in a Josephson-junction charge two-level system. Phys. Rev. Lett. **87**, 246601 (2001). Cited on page 2

[55] T. Yamamoto, Y. A. Pashkin, O. Astafiev, Y. Nakamura, J. S. Tsai. Demonstration of conditional gate operation using superconducting charge qubits. Nature **425**, 941 (2003). Cited on page 2

[56] O. Astafiev, Y. A. Pashkin, Y. Nakamura, T. Yamamoto, J. S. Tsai. Quantum noise in the Josephson charge qubit. Phys. Rev. Lett. **93**, 267007 (2004). Cited on page 2

[57] Y. Nakamura, Y. A. Pashkin, T. Yamamoto, J. S. Tsai. Charge echo in a Cooper-pair box. Phys. Rev. Lett. **88**, 047901 (2002). Cited on page 3

[58] D. Vion, A. Aassime, A. Cottet, P. Joyez, H. Pothier, C. Urbina, D. Esteve, M. H. Devoret. Manipulating the quantum state of an electrical circuit. Science **296**, 886 (2002). Cited on page 3

[59] G. Ithier, E. Collin, P. Joyez, P. J. Meeson, D. Vion, D. Esteve, F. Chiarello, A. Shnirman, Y. Makhlin, J. Schriefl, G. Schön. Decoherence in a superconducting quantum bit circuit. Phys. Rev. B **72**, 134519 (2005). Cited on page 3

[60] R. J. Schoelkopf, P. Wahlgren, A. A. Kozhevnikov, P. Delsing, D. E. Prober. The radio-frequency single-electron transistor (RF-SET): A fast and ultrasensitive electrometer. Science **280**, 1238 (1998). Cited on page 3

[61] K. W. Lehnert, K. Bladh, L. F. Spietz, D. Gunnarsson, D. I. Schuster, P. Delsing, R. J. Schoelkopf. Measurement of the excited-state lifetime of a microelectronic circuit. Phys. Rev. Lett. **90**, 027002 (2003). Cited on page 3

[62] T. Duty, D. Gunnarsson, K. Bladh, P. Delsing. Coherent dynamics of a Josephson charge qubit. Phys. Rev. B **69**, 140503 (2004). Cited on page 3

[63] A. Blais, R.-S. Huang, A. Wallraff, S. M. Girvin, R. J. Schoelkopf. Cavity quantum electrodynamics for superconducting electrical circuits: An architecture for quantum computation. Phys. Rev. A **69**, 062320 (2004). Cited on page 3

[64] A. Wallraff, D. I. Schuster, A. Blais, L. Frunzio, R.-S. Huang, J. Majer, S. Kumar, S. M. Girvin, R. J. Schoelkopf. Strong coupling of a single photon to a superconducting qubit using circuit quantum electrodynamics. Nature **431**, 162 (2004). Cited on page 3

[65] D. Sank. What is the difference between transmon and Xmon qubits? Quantum Computing Stack Exchange. `https://quantumcomputing.stackexchange.com/a/1537 (version: 2020-04-10)`. Cited on page 3

[66] J. Koch, T. M. Yu, J. Gambetta, A. A. Houck, D. I. Schuster, J. Majer, A. Blais, M. H. Devoret, S. M. Girvin, R. J. Schoelkopf. Charge-insensitive qubit design derived from the Cooper pair box. Phys. Rev. A **76**, 042319 (2007). Cited on pages 3, 18, and 101

[67] J. A. Schreier, A. A. Houck, J. Koch, D. I. Schuster, B. R. Johnson, J. M. Chow, J. M. Gambetta, J. Majer, L. Frunzio, M. H. Devoret, S. M. Girvin, R. J. Schoelkopf. Suppressing charge noise decoherence in superconducting charge qubits. Phys. Rev. B **77**, 180502 (2008). Cited on page 3

[68] A. A. Houck, J. Koch, M. H. Devoret, S. M. Girvin, R. J. Schoelkopf. Life after charge noise: recent results with transmon qubits. Quantum Information Processing **8**, 105 (2009). Cited on page 3

[69] F. Arute, K. Arya, R. Babbush, D. Bacon, J. C. Bardin, R. Barends, R. Biswas, S. Boixo, F. G. S. L. Brandao, D. A. Buell, B. Burkett, Y. Chen, Z. Chen, B. Chiaro, R. Collins, W. Courtney, A. Dunsworth, E. Farhi, B. Foxen, A. Fowler, C. Gidney, M. Giustina, R. Graff, K. Guerin, S. Habegger, M. P. Harrigan, M. J. Hartmann, A. Ho, M. Hoffmann, T. Huang, T. S. Humble, S. V. Isakov, E. Jeffrey, Z. Jiang, D. Kafri, K. Kechedzhi, J. Kelly, P. V. Klimov, S. Knysh, A. Korotkov, F. Kostritsa, D. Landhuis, M. Lindmark, E. Lucero, D. Lyakh, S. Mandrà, J. R. McClean, M. McEwen, A. Megrant, X. Mi, K. Michielsen, M. Mohseni, J. Mutus, O. Naaman, M. Neeley, C. Neill, M. Y. Niu, E. Ostby, A. Petukhov, J. C. Platt, C. Quintana, E. G. Rieffel, P. Roushan, N. C. Rubin, D. Sank, K. J. Satzinger, V. Smelyanskiy, K. J. Sung, M. D. Trevithick, A. Vainsencher, B. Villalonga, T. White, Z. J. Yao, P. Yeh, A. Zalcman, H. Neven, J. M. Martinis. Quantum supremacy using a programmable superconducting processor. Nature **574**, 505 (2019). Cited on page 3

[70] R. P. Poplavskii. Thermodynamic models of information processes. Phys. Usp. **18**, 222 (1975). Cited on page 4

[71] R. P. Feynman. Simulating physics with computers. International Journal of Theoretical Physics **21**, 467 (1982). Cited on page 4

[72] R. P. Feynman. Quantum mechanical computers. Optics News **11**, 11 (1985). Cited on page 4

[73] Y. I. Manin. Vychislimoe i nevychislimoe [Computable and uncomputable]. Sovetskoye Radio, Moscow 13–15 (1980). Cited on page 4

[74] D. Deutsch. Quantum theory, the Church–Turing principle and the universal quantum computer. Proceedings of the Royal Society of London. A. Mathematical and Physical Sciences **400**, 97 (1985). Cited on page 4

[75] D. E. Deutsch. Quantum computational networks. Proceedings of the Royal Society of London. A. Mathematical and Physical Sciences **425**, 73 (1989). Cited on page 4

[76] S. Lloyd. Universal quantum simulators. Science **273**, 1073 (1996). Cited on page 4

[77] D. P. Divincenzo. Quantum computation. Science **270**, 255 (1995). Cited on page 4

[78] J. F. Poyatos, J. I. Cirac, P. Zoller. Quantum reservoir engineering with laser cooled trapped ions. Phys. Rev. Lett. **77**, 4728 (1996). Cited on page 6

[79] D. J. Wineland, W. M. Itano. Laser cooling of atoms. Phys. Rev. A **20**, 1521 (1979). Cited on page 6

[80] M. Aspelmeyer, T. J. Kippenberg, F. Marquardt. Cavity optomechanics. Rev. Mod. Phys. **86**, 1391 (2014). Cited on page 6

[81] C. M. Wilson, T. Duty, F. Persson, M. Sandberg, G. Johansson, P. Delsing. Coherence times of dressed states of a superconducting qubit under extreme driving. Phys. Rev. Lett. **98**, 257003 (2007). Cited on page 6

[82] S. Boutin, C. K. Andersen, J. Venkatraman, A. J. Ferris, A. Blais. Resonator reset in circuit QED by optimal control for large open quantum systems. Phys. Rev. A **96**, 042315 (2017). Cited on page 6

[83] P. Magnard, P. Kurpiers, B. Royer, T. Walter, J.-C. Besse, S. Gasparinetti, M. Pechal, J. Heinsoo, S. Storz, A. Blais, A. Wallraff. Fast and unconditional all-microwave reset of a superconducting qubit. Phys. Rev. Lett. **121**, 060502 (2018). Cited on page 6

[84] S. O. Valenzuela, W. D. Oliver, D. M. Berns, K. K. Berggren, L. S. Levitov, T. P. Orlando. Microwave-induced cooling of a superconducting qubit. Science **314**, 1589 (2006). Cited on page 6

[85] K. W. Murch, U. Vool, D. Zhou, S. J. Weber, S. M. Girvin, I. Siddiqi. Cavity-assisted quantum bath engineering. Phys. Rev. Lett. **109**, 183602 (2012). Cited on page 6

[86] K. Geerlings, Z. Leghtas, I. M. Pop, S. Shankar, L. Frunzio, R. J. Schoelkopf, M. Mirrahimi, M. H. Devoret. Demonstrating a driven reset protocol for a superconducting qubit. Phys. Rev. Lett. **110**, 120501 (2013). Cited on page 6

[87] S. Shankar, M. Hatridge, Z. Leghtas, K. M. Sliwa, A. Narla, U. Vool, S. M. Girvin, L. Frunzio, M. Mirrahimi, M. H. Devoret. Autonomously stabilized entanglement between two superconducting quantum bits. Nature **504**, 419 (2013). Cited on pages 6 and 120

[88] E. T. Holland, B. Vlastakis, R. W. Heeres, M. J. Reagor, U. Vool, Z. Leghtas, L. Frunzio, G. Kirchmair, M. H. Devoret, M. Mirrahimi, R. J. Schoelkopf. Single-photon-resolved cross-kerr interaction for autonomous stabilization of photon-number states. Phys. Rev. Lett. **115**, 180501 (2015). Cited on page 6

[89] Z. Leghtas, S. Touzard, I. M. Pop, A. Kou, B. Vlastakis, A. Petrenko, K. M. Sliwa, A. Narla, S. Shankar, M. J. Hatridge, M. Reagor, L. Frunzio, R. J. Schoelkopf, M. Mirrahimi, M. H. Devoret. Confining the state of light to a quantum manifold by engineered two-photon loss. Science **347**, 853 (2015). Cited on page 6

[90] M. E. Kimchi-Schwartz, L. Martin, E. Flurin, C. Aron, M. Kulkarni, H. E. Türeci, I. Siddiqi. Stabilizing entanglement via symmetry-selective bath engineering in superconducting qubits. Phys. Rev. Lett. **116**, 240503 (2016). Cited on page 6

[91] Y. Liu, S. Shankar, N. Ofek, M. Hatridge, A. Narla, K. M. Sliwa, L. Frunzio, R. J. Schoelkopf, M. H. Devoret. Comparing and combining measurement-based and driven-dissipative entanglement stabilization. Phys. Rev. X **6**, 011022 (2016). Cited on page 6

[92] Y. Lu, S. Chakram, N. Leung, N. Earnest, R. K. Naik, Z. Huang, P. Groszkowski, E. Kapit, J. Koch, D. I. Schuster. Universal stabilization of a parametrically coupled qubit. Phys. Rev. Lett. **119**, 150502 (2017). Cited on pages 6 and 120

[93] L. Bretheau, P. Campagne-Ibarcq, E. Flurin, F. Mallet, B. Huard. Quantum dynamics of an electromagnetic mode that cannot contain N photons. Science **348**, 776 (2015). Cited on page 6

[94] S. Hacohen-Gourgy, V. V. Ramasesh, C. De Grandi, I. Siddiqi, S. M. Girvin. Cooling and autonomous feedback in a Bose-Hubbard chain with attractive interactions. Phys. Rev. Lett. **115**, 240501 (2015). Cited on page 6

[95] R. Ma, B. Saxberg, C. Owens, N. Leung, Y. Lu, J. Simon, D. I. Schuster. A dissipatively stabilized Mott insulator of photons. Nature **566**, 51 (2019). Cited on page 6

[96] Y. Yanay, J. Braumüller, S. Gustavsson, W. D. Oliver, C. Tahan. Realizing the two-dimensional hard-core Bose-Hubbard model with superconducting qubits. arXiv e-prints arXiv:1910.00933 (2019). Cited on page 6

[97] E. Kapit. The upside of noise: Engineered dissipation as a resource in superconducting circuits. Quantum Science and Technology **2**, 033002 (2017). Cited on page 6

[98] Z. Leghtas, G. Kirchmair, B. Vlastakis, R. J. Schoelkopf, M. H. Devoret, M. Mirrahimi. Hardware-efficient autonomous quantum memory protection. Phys. Rev. Lett. **111**, 120501 (2013). Cited on page 6

[99] S. Touzard, A. Grimm, Z. Leghtas, S. O. Mundhada, P. Reinhold, C. Axline, M. Reagor, K. Chou, J. Blumoff, K. M. Sliwa, S. Shankar, L. Frunzio, R. J. Schoelkopf, M. Mirrahimi, M. H. Devoret. Coherent oscillations inside a quantum manifold stabilized by dissipation. Phys. Rev. X **8**, 021005 (2018). Cited on page 6

[100] P. M. Harrington, D. Tan, M. Naghiloo, K. W. Murch. Characterizing a statistical arrow of time in quantum measurement dynamics. Phys. Rev. Lett. **123**, 020502 (2019). Cited on page 7

[101] P. M. Harrington, M. Naghiloo, D. Tan, K. W. Murch. Bath engineering of a fluorescing artificial atom with a photonic crystal. Phys. Rev. A **99**, 052126 (2019). Cited on page 7

[102] M. H. Devoret. Quantum fluctuations in electrical circuits (1997). Cited on page 10

[103] B. Yurke, J. S. Denker. Quantum network theory. Phys. Rev. A **29**, 1419 (1984). Cited on page 11

[104] U. Vool, M. Devoret. Introduction to quantum electromagnetic circuits. International Journal of Circuit Theory and Applications **45**, 897 (2017). Cited on page 11

[105] A. N. Cleland. *Macroscopic Quantum Tunneling in Josephson Tunnel Junctions and Coulomb Blockade in Single Small Tunnel Junctions*. Ph.D. dissertation, University of California, Berkeley (1991). Cited on page 12

[106] C. W. Gardiner, P. Zoller. *Quantum Noise: A Handbook of Markovian and Non-Markovian Quantum Stochastic Methods with Applications to Quantum Optics*. Springer-Verlag Berlin Heidelberg, 3rd edition (2004). Cited on page 12

[107] S. M. Girvin. *Circuit QED: Superconducting Qubits Coupled to Microwave Photons*. Oxford University Press (2009). Cited on pages 13 and 16

[108] U. Vool. *Engineering Synthetic Quantum Operations*. Ph.D. dissertation, Yale University (2017). Cited on page 16

[109] J. Puertas Martínez. *Probing light-matter interaction in the many-body regime of superconducting quantum circuits*. Ph.D. dissertation, Laboratoire Institut Néel, CNRS (2018). Cited on pages 17 and 31

[110] E. T. Jaynes, F. W. Cummings. Comparison of quantum and semiclassical radiation theories with application to the beam maser. Proceedings of the IEEE **51**, 89 (1963). Cited on page 19

[111] J. R. Schrieffer, P. A. Wolff. Relation between the Anderson and Kondo Hamiltonians. Phys. Rev. **149**, 491 (1966). Cited on page 23

[112] M. Boissonneault, J. M. Gambetta, A. Blais. Dispersive regime of circuit QED: Photon-dependent qubit dephasing and relaxation rates. Phys. Rev. A **79**, 013819 (2009). Cited on pages 23 and 112

[113] J. Niemeyer. Eine einfache Methode zur Herstellung kleinster Josephson-Elemente [A simple method for producing the smallest Josephson elements]. PTB-Mitt. **84**, 251 (1974). Cited on page 30

[114] G. J. Dolan. Offset masks for lift-off photoprocessing. Applied Physics Letters **31**, 337 (1977). Cited on page 30

[115] V. Ambegaokar, A. Baratoff. Tunneling between superconductors. Phys. Rev. Lett. **10**, 486 (1963). Cited on page 31

[116] H. Paik, D. I. Schuster, L. S. Bishop, G. Kirchmair, G. Catelani, A. P. Sears, B. R. Johnson, M. J. Reagor, L. Frunzio, L. I. Glazman, S. M. Girvin, M. H. Devoret, R. J. Schoelkopf. Observation of high coherence in Josephson junction qubits measured in a three-dimensional circuit QED architecture. Phys. Rev. Lett. **107**, 240501 (2011). Cited on pages 32 and 101

[117] F. Pobell. *Matter and Methods at Low Temperatures*. Springer-Verlag Berlin Heidelberg, 3rd edition (2007). Cited on page 33

[118] J. W. Ekin. *Experimental Techniques for Low-Temperature Measurements*. Oxford University Press (2006). Cited on page 34

[119] H. Nyquist. Thermal agitation of electric charge in conductors. Physical Review **32**, 110 (1928). Cited on page 35

[120] J. B. Johnson. Thermal agitation of electricity in conductors. Phys. Rev. **32**, 97 (1928). Cited on page 35

[121] D. M. Pozar. *Microwave Engineering*. John Wiley & Sons, Inc., Hoboken, NJ, USA, 4th edition (2012). Cited on page 36

[122] D. H. Slichter. *Quantum Jumps and Measurement Backaction in a Superconducting Qubit*. Ph.D. dissertation, University of California, Berkeley (2011). Cited on page 38

[123] W. C. Stewart. Current-voltage characteristics of Josephson junctions. Applied Physics Letters **12**, 277 (1968). Cited on page 40

[124] D. E. McCumber. Effect of AC impedance on DC voltage-current characteristics of superconductor weak-link junctions. Journal of Applied Physics **39**, 3113 (1968). Cited on page 40

[125] V. E. Manucharyan, E. Boaknin, M. Metcalfe, R. Vijay, I. Siddiqi, M. Devoret. Microwave bifurcation of a Josephson junction: Embedding-circuit requirements. Phys. Rev. B **76**, 014524 (2007). Cited on page 44

[126] M. Hatridge, S. Shankar, M. Mirrahimi, F. Schackert, K. Geerlings, T. Brecht, K. M. Sliwa, B. Abdo, L. Frunzio, S. M. Girvin, R. J. Schoelkopf, M. H. Devoret. Quantum back-action of an individual variable-strength measurement. Science **339**, 178 (2013). Cited on pages 46 and 73

[127] K. Gottfried, T.-M. Yan. *Quantum Mechanics: Fundamentals*. Graduate Texts in Contemporary Physics. Springer New York (2003). Cited on page 47

[128] H. P. Breuer, F. Petruccione. *The Theory of Open Quantum Systems*. Oxford University Press (2002). Cited on pages 47, 51, 52, and 112

[129] H. Wiseman, G. Milburn. *Quantum Measurement and Control*. Cambridge University Press (2010). Cited on pages 49 and 63

[130] H. J. Carmichael. *An Open Systems Approach to Quantum Optics*. Springer-Verlag (1999). Cited on page 50

[131] L. S. Bishop. *Circuit Quantum Electrodynamics*. Ph.D. dissertation, Yale University (2010). Cited on page 52

[132] A. Chantasri. *Stochastic Path Integral Formalism For Continuous Quantum Measurement*. Ph.D. dissertation, University of Rochester (2016). Cited on page 55

[133] K. Jacobs. *Quantum Measurement Theory*. Cambridge (2014). Cited on pages 56, 58, and 63

[134] P. Lewalle, A. Chantasri, A. N. Jordan. Prediction and characterization of multiple extremal paths in continuously monitored qubits. Phys. Rev. A **95**, 042126 (2017). Cited on page 59

[135] I. Prigogine. *Time, Structure and Fluctuations, Nobel Lecture*. The Nobel Foundation (1977). Cited on page 61

[136] V. B. Braginsky, F. Y. Khalili. *Quantum Measurement*. Cambridge University Press (1992). Cited on page 63

[137] K. W. Murch, S. J. Weber, C. Macklin, I. Siddiqi. Observing single quantum trajectories of a superconducting qubit. Nature **502**, 211 (2013). Cited on pages 63 and 66

[138] N. Roch, M. E. Schwartz, F. Motzoi, C. Macklin, R. Vijay, A. W. Eddins, A. N. Korotkov, K. B. Whaley, M. Sarovar, I. Siddiqi. Observation of measurement-induced entanglement and quantum trajectories of remote superconducting qubits. Phys. Rev. Lett. **112**, 170501 (2014). Cited on pages 63 and 120

[139] P. Campagne-Ibarcq, P. Six, L. Bretheau, A. Sarlette, M. Mirrahimi, P. Rouchon, B. Huard. Observing quantum state diffusion by heterodyne detection of fluorescence. Phys. Rev. X **6**, 011002 (2016). Cited on pages 63 and 120

[140] M. Naghiloo, N. Foroozani, D. Tan, A. Jadbabaie, K. W. Murch. Mapping quantum state dynamics in spontaneous emission. Nature Communications **7**, 11527 (2016). Cited on pages 63 and 120

[141] A. Chantasri, J. Dressel, A. N. Jordan. Action principle for continuous quantum measurement. Phys. Rev. A **88**, 042110 (2013). Cited on page 63

[142] S. J. Weber, A. Chantasri, J. Dressel, A. N. Jordan, K. W. Murch, I. Siddiqi. Mapping the optimal route between two quantum states. Nature **511**, 570 (2014). Cited on page 63

[143] A. N. Jordan, A. Chantasri, P. Rouchon, B. Huard. Anatomy of fluorescence: quantum trajectory statistics from continuously measuring spontaneous emission. Quantum Studies: Mathematics and Foundations **3**, 237 (2016). Cited on page 63

[144] A. Chantasri, J. Atalaya, S. Hacohen-Gourgy, L. S. Martin, I. Siddiqi, A. N. Jordan. Simultaneous continuous measurement of noncommuting observables: Quantum state correlations. Physics Review A **97**, 012118 (2018). Cited on page 63

[145] M. Naghiloo, D. Tan, P. M. Harrington, P. Lewalle, A. N. Jordan, K. W. Murch. Quantum caustics in resonance-fluorescence trajectories. Physics Review A **96**, 053807 (2017). Cited on page 63

[146] G. E. Crooks. Entropy production fluctuation theorem and the nonequilibrium work relation for free energy differences. Phys. Rev. E **60**, 2721 (1999). Cited on page 63

[147] G. E. Crooks. Path-ensemble averages in systems driven far from equilibrium. Phys. Rev. E **61**, 2361 (2000). Cited on pages 63 and 87

[148] U. Seifert. Entropy production along a stochastic trajectory and an integral fluctuation theorem. Phys. Rev. Lett. **95**, 040602 (2005). Cited on pages 63, 87, and 88

[149] R. J. Harris, G. M. Schütz. Fluctuation theorems for stochastic dynamics. Journal of Statistical Mechanics: Theory and Experiment **7**, 07020 (2007). Cited on pages 63 and 87

[150] J. M. Horowitz. Quantum-trajectory approach to the stochastic thermodynamics of a forced harmonic oscillator. Phys. Rev. E **85**, 031110 (2012). Cited on pages 63 and 87

[151] J. Liphardt, S. Dumont, S. B. Smith, I. Tinoco, C. Bustamante. Equilibrium information from nonequilibrium measurements in an experimental test of Jarzynski's equality. Science **296**, 1832 (2002). Cited on page 63

[152] G. M. Wang, E. M. Sevick, E. Mittag, D. J. Searles, D. J. Evans. Experimental demonstration of violations of the second law of thermodynamics for small systems and short time scales. Phys. Rev. Lett. **89**, 050601 (2002). Cited on page 63

[153] C. Tietz, S. Schuler, T. Speck, U. Seifert, J. Wrachtrup. Measurement of stochastic entropy production. Phys. Rev. Lett. **97**, 050602 (2006). Cited on page 63

[154] M. Esposito, U. Harbola, S. Mukamel. Entropy fluctuation theorems in driven open systems: Application to electron counting statistics. Phys. Rev. E **76**, 031132 (2007). Cited on page 63

[155] V. Blickle, T. Speck, L. Helden, U. Seifert, C. Bechinger. Thermodynamics of a colloidal particle in a time-dependent nonharmonic potential. Phys. Rev. Lett. **96**, 070603 (2006). Cited on page 63

[156] T. Speck, V. Blickle, C. Bechinger, U. Seifert. Distribution of entropy production for a colloidal particle in a nonequilibrium steady state. EPL (Europhysics Letters) **79**, 30002 (2007). Cited on page 63

[157] Y. Utsumi, D. S. Golubev, M. Marthaler, K. Saito, T. Fujisawa, G. Schön. Bidirectional single-electron counting and the fluctuation theorem. Phys. Rev. B **81**, 125331 (2010). Cited on page 63

[158] B. Küng, C. Rössler, M. Beck, M. Marthaler, D. S. Golubev, Y. Utsumi, T. Ihn, K. Ensslin. Irreversibility on the level of single-electron tunneling. Phys. Rev. X **2**, 011001 (2012). Cited on page 63

[159] O.-P. Saira, Y. Yoon, T. Tanttu, M. Möttönen, D. V. Averin, J. P. Pekola. Test of the Jarzynski and Crooks fluctuation relations in an electronic system. Phys. Rev. Lett. **109**, 180601 (2012). Cited on page 63

[160] J. V. Koski, T. Sagawa, O.-P. Saira, Y. Yoon, A. Kutvonen, P. Solinas, M. Möttönen, T. Ala-Nissila, J. P. Pekola. Distribution of entropy production in a single-electron box. Nature Physics **9**, 644 EP (2013). Cited on page 63

[161] T. M. Hoang, R. Pan, J. Ahn, J. Bang, H. T. Quan, T. Li. Experimental test of the differential fluctuation theorem and a generalized Jarzynski equality for arbitrary initial states. Phys. Rev. Lett. **120**, 080602 (2018). Cited on page 63

[162] C. Jarzynski. Nonequilibrium equality for free energy differences. Phys. Rev. Lett. **78**, 2690 (1997). Cited on page 63

[163] G. E. Crooks. Nonequilibrium measurements of free energy differences for microscopically reversible Markovian systems. Journal of Statistical Physics **90**, 1481 (1998). Cited on pages 63 and 87

[164] M. Esposito, C. Van den Broeck. Three detailed fluctuation theorems. Phys. Rev. Lett. **104**, 090601 (2010). Cited on pages 63 and 87

[165] C. Jarzynski. Equalities and inequalities: Irreversibility and the second law of thermodynamics at the nanoscale. C. Annu. Rev. Condens. Matter Phys. **2**, 329 (2011). Cited on pages 63 and 87

[166] U. Seifert. Thermodynamics, fluctuation theorems and molecular machines. Rep. Prog. Phys. **75**, 126001 (2012). Cited on pages 63 and 87

[167] S. Ciliberto, R. Gomez-Solano, A. Petrosyan. Fluctuations, linear response, and currents in out-of-equilibrium systems. C. Annu. Rev. Condens. Matter Phys. **4**, 235 (2013). Cited on pages 63 and 87

[168] G. Manzano, J. M. Horowitz, J. M. R. Parrondo. Quantum fluctuation theorems for arbitrary environments: Adiabatic and nonadiabatic entropy production. Phys. Rev. X **8**, 031037 (2018). Cited on page 63

[169] J. Kurchan. A quantum fluctuation theorem. arXiv e-prints cond-mat/0007360 (2000). Cited on page 64

[170] S. Mukamel. Quantum extension of the Jarzynski relation: Analogy with stochastic dephasing. Phys. Rev. Lett. **90**, 170604 (2003). Cited on page 64

[171] M. Campisi, P. Talkner, P. Hänggi. Fluctuation theorem for arbitrary open quantum systems. Phys. Rev. Lett. **102**, 210401 (2009). Cited on page 64

[172] S. Deffner, E. Lutz. Nonequilibrium entropy production for open quantum systems. Phys. Rev. Lett. **107**, 140404 (2011). Cited on page 64

[173] Y. Morikuni, H. Tasaki. Quantum Jarzynski-Sagawa-Ueda relations. Journal of Statistical Physics **143**, 1 (2011). Cited on page 64

[174] R. Chetrite, K. Mallick. Quantum fluctuation relations for the Lindblad master equation. Journal of Statistical Physics **148**, 480 (2012). Cited on page 64

[175] J. M. Horowitz, J. M. R. Parrondo. Entropy production along nonequilibrium quantum jump trajectories. New Journal of Physics **15**, 085028 (2013). Cited on page 64

[176] H. T. Quan, Y. D. Wang, Y.-x. Liu, C. P. Sun, F. Nori. Maxwell's demon assisted thermodynamic cycle in superconducting quantum circuits. Phys. Rev. Lett. **97**, 180402 (2006). Cited on page 64

[177] H. T. Quan, Y.-x. Liu, C. P. Sun, F. Nori. Quantum thermodynamic cycles and quantum heat engines. Phys. Rev. E **76**, 031105 (2007). Cited on page 64

[178] R. Dorner, S. R. Clark, L. Heaney, R. Fazio, J. Goold, V. Vedral. Extracting quantum work statistics and fluctuation theorems by single-qubit interferometry. Phys. Rev. Lett. **110**, 230601 (2013). Cited on page 64

[179] L. Mazzola, G. De Chiara, M. Paternostro. Measuring the characteristic function of the work distribution. Phys. Rev. Lett. **110**, 230602 (2013). Cited on page 64

[180] P. Campagne-Ibarcq, L. Bretheau, E. Flurin, A. Auffèves, F. Mallet, B. Huard. Observing interferences between past and future quantum states in resonance fluorescence. Phys. Rev. Lett. **112**, 180402 (2014). Cited on page 64

[181] J. Goold, U. Poschinger, K. Modi. Measuring the heat exchange of a quantum process. Phys. Rev. E **90**, 020101 (2014). Cited on page 64

[182] A. J. Roncaglia, F. Cerisola, J. P. Paz. Work measurement as a generalized quantum measurement. Phys. Rev. Lett. **113**, 250601 (2014). Cited on page 64

[183] G. D. Chiara, A. J. Roncaglia, J. P. Paz. Measuring work and heat in ultracold quantum gases. New Journal of Physics **17**, 035004 (2015). Cited on page 64

[184] T. B. Batalhão, A. M. Souza, R. S. Sarthour, I. S. Oliveira, M. Paternostro, E. Lutz, R. M. Serra. Irreversibility and the arrow of time in a quenched quantum system. Phys. Rev. Lett. **115**, 190601 (2015). Cited on page 64

[185] S. An, J.-N. Zhang, M. Um, D. Lv, Y. Lu, J. Zhang, Z.-Q. Yin, H. T. Quan, K. Kim. Experimental test of the quantum Jarzynski equality with a trapped-ion system. Nature Physics **11**, 193 (2015). Cited on page 64

[186] J. J. Alonso, E. Lutz, A. Romito. Thermodynamics of weakly measured quantum systems. Phys. Rev. Lett. **116**, 080403 (2016). Cited on page 64

[187] G. Watanabe, B. P. Venkatesh, P. Talkner. Generalized energy measurements and modified transient quantum fluctuation theorems. Phys. Rev. E **89**, 052116 (2014). Cited on page 64

[188] J. Yi, P. Talkner, Y. W. Kim. Single-temperature quantum engine without feedback control. Phys. Rev. E **96**, 022108 (2017). Cited on page 64

[189] M. Campisi, P. Hänggi, P. Talkner. Colloquium: Quantum fluctuation relations: Foundations and applications. Rev. Mod. Phys. **83**, 771 (2011). Cited on page 64

[190] G. Watanabe, B. P. Venkatesh, P. Talkner. Generalized energy measurements and modified transient quantum fluctuation theorems. Phys. Rev. E **89**, 052116 (2014). Cited on page 64

[191] C. Elouard, D. A. Herrera-Martí, M. Clusel, A. Auffèves. The role of quantum measurement in stochastic thermodynamics. npj Quantum Information **3** (2017). Cited on page 64

[192] T. Benoist, V. Jakšić, Y. Pautrat, C.-A. Pillet. On entropy production of repeated quantum measurements I. general theory. Communications in Mathematical Physics **357**, 77 (2017). Cited on page 64

[193] C. Elouard, D. Herrera-Martí, B. Huard, A. Auffèves. Extracting work from quantum measurement in Maxwell's demon engines. Phys. Rev. Lett. **118**, 260603 (2017). Cited on page 64

[194] C. Elouard, A. N. Jordan. Efficient quantum measurement engines. Phys. Rev. Lett. **120**, 260601 (2018). Cited on page 64

[195] L. Buffoni, A. Solfanelli, P. Verrucchi, A. Cuccoli, M. Campisi. Quantum measurement cooling. Phys. Rev. Lett. **122**, 070603 (2019). Cited on page 64

[196] M. Esposito, U. Harbola, S. Mukamel. Nonequilibrium fluctuations, fluctuation theorems, and counting statistics in quantum systems. Rev. Mod. Phys. **81**, 1665 (2009). Cited on page 64

[197] C. Elouard, D. A. Herrera-Martí, M. Clusel, A. Auffèves. The role of quantum measurement in stochastic thermodynamics. npj Quantum Information **3**, 9 (2017). Cited on page 64

[198] M. Naghiloo, D. Tan, P. M. Harrington, J. J. Alonso, E. Lutz, A. Romito, K. W. Murch. Heat and work along individual trajectories of a quantum bit. Phys. Rev. Lett. **124**, 110604 (2020). Cited on page 64

[199] L. S. Schulman. *Time's Arrow and Quantum Measurement*. Cambridge University Press, Cambridge (1997). Cited on page 64

[200] J. Dressel, A. Chantasri, A. N. Jordan, A. N. Korotkov. Arrow of time for continuous quantum measurement. Phys. Rev. Lett. **119**, 220507 (2017). Cited on pages 64, 69, 88, and 89

[201] K. Micadei, J. P. S. Peterson, A. M. Souza, R. S. Sarthour, I. S. Oliveira, G. T. Landi, T. B. Batalhão, R. M. Serra, E. Lutz. Reversing the direction of heat flow using quantum correlations. arXiv e-prints arXiv:1711.03323 (2017). Cited on page 64

[202] S. K. Manikandan, A. N. Jordan. Time reversal symmetry of generalized quantum measurements with past and future boundary conditions. arXiv:1801.04364 (2018). Cited on page 64

[203] K. Jacobs, D. A. Steck. A straightforward introduction to continuous quantum measurement. Contemp. Phys. **47**, 279 (2006). Cited on pages 65 and 72

[204] A. N. Jordan, A. N. Korotkov. Qubit feedback and control with kicked quantum nondemolition measurements: A quantum Bayesian analysis. Phys. Rev. B **74**, 085307 (2006). Cited on page 65

[205] A. N. Korotkov, A. N. Jordan. Undoing a weak quantum measurement of a solid-state qubit. Phys. Rev. Lett. **97**, 166805 (2006). Cited on page 66

[206] N. Katz, M. Ansmann, R. C. Bialczak, E. Lucero, R. McDermott, M. Neeley, M. Steffen, E. M. Weig, A. N. Cleland, J. M. Martinis, A. N. Korotkov. Coherent state evolution in a superconducting qubit from partial-collapse measurement. Science **312**, 1498 (2006). Cited on page 66

[207] N. Katz, M. Neeley, M. Ansmann, R. C. Bialczak, M. Hofheinz, E. Lucero, A. O'Connell, H. Wang, A. N. Cleland, J. M. Martinis, A. N. Korotkov. Reversal of the weak measurement of a quantum state in a superconducting phase qubit. Phys. Rev. Lett. **101**, 200401 (2008). Cited on page 66

[208] Y.-S. Kim, J.-C. Lee, O. Kwon, Y.-H. Kim. Protecting entanglement from decoherence using weak measurement and quantum measurement reversal. Nature Physics **8**, 117 (2011). Cited on page 66

[209] G. S. Paraoanu. Partial measurements and the realization of quantum-mechanical counterfactuals. Foundations of Physics **41**, 1214 (2011). Cited on page 66

[210] A. Chantasri, A. N. Jordan. Stochastic path-integral formalism for continuous quantum measurement. Phys. Rev. A **92**, 032125 (2015). Cited on page 68

[211] A. N. Korotkov. Quantum Bayesian approach to circuit QED measurement. arXiv:1111.4016 (2011). Cited on page 73

[212] M. A. Castellanos-Beltran, K. D. Irwin, G. C. Hilton, L. R. Vale, K. W. Lehnert. Amplification and squeezing of quantum noise with a tunable Josephson metamaterial. Nature Physics **4**, 929 (2008). Cited on page 81

[213] M. Hatridge, R. Vijay, D. H. Slichter, J. Clarke, I. Siddiqi. Dispersive magnetometry with a quantum limited squid parametric amplifier. Phys. Rev. B **83**, 134501 (2011). Cited on page 81

[214] C. Jarzynski. Microscopic analysis of Clausius-Duhem processes. Journal of Statistical Physics **96**, 415 (1999). Cited on page 87

[215] Y. Murashita, K. Funo, M. Ueda. Nonequilibrium equalities in absolutely irreversible processes. Phys. Rev. E **90**, 042110 (2014). Cited on page 89

[216] K. Funo, Y. Murashita, M. Ueda. Quantum nonequilibrium equalities with absolute irreversibility. New Journal of Physics **17**, 075005 (2015). Cited on page 89

[217] G. Manzano, J. M. Horowitz, J. M. R. Parrondo. Nonequilibrium potential and fluctuation theorems for quantum maps. Phys. Rev. E **92**, 032129 (2015). Cited on page 89

[218] S. K. Manikandan, C. Elouard, A. N. Jordan. Fluctuation theorems for continuous quantum measurements and absolute irreversibility. Phys. Rev. A **99**, 022117 (2019). Cited on page 89

[219] P. A. M. Dirac. The quantum theory of the emission and absorption of radiation. Proceedings of the Royal Society of London. Series A, Containing Papers of a Mathematical and Physical Character **114**, 243 (1927). Cited on pages 96 and 105

[220] V. P. Bykov. Spontaneous emission in a periodic structure. Soviet Journal of Experimental and Theoretical Physics **35**, 269 (1972). Cited on page 98

[221] E. Yablonovitch. Inhibited spontaneous emission in solid-state physics and electronics. Phys. Rev. Lett. **58**, 2059 (1987). Cited on page 98

[222] J. D. Joannopoulos, S. G. Johnson, J. N. Winn, R. D. Meade. *Photonic Crystals: Molding the Flow of Light*. Princeton University Press, Princeton, New Jersey, 2nd edition (2008). Cited on page 98

[223] M. Mirhosseini, E. Kim, V. S. Ferreira, M. Kalaee, A. Sipahigil, A. J. Keller, O. Painter. Superconducting metamaterials for waveguide quantum electrodynamics. Nature Communications **13**, 48 (2018). Cited on pages 100 and 120

[224] E. M. Purcell, H. C. Torrey, R. V. Pound. Resonance absorption by nuclear magnetic moments in a solid. Phys. Rev. **69**, 37 (1946). Cited on page 105

[225] S. E. Nigg, H. Paik, B. Vlastakis, G. Kirchmair, S. Shankar, L. Frunzio, M. H. Devoret, R. J. Schoelkopf, S. M. Girvin. Black-box superconducting circuit quantization. Phys. Rev. Lett. **108**, 240502 (2012). Cited on page 105

[226] D. I. Schuster. *Circuit Quantum Electrodynamics*. Ph.D. dissertation, Yale University (2007). Cited on page 105

[227] A. A. Houck, J. A. Schreier, B. R. Johnson, J. M. Chow, J. Koch, J. M. Gambetta, D. I. Schuster, L. Frunzio, M. H. Devoret, S. M. Girvin, R. J. Schoelkopf. Controlling the spontaneous emission of a superconducting transmon qubit. Phys. Rev. Lett. **101**, 080502 (2008). Cited on page 105

[228] M. D. Reed, L. DiCarlo, B. R. Johnson, L. Sun, D. I. Schuster, L. Frunzio, R. J. Schoelkopf. High-fidelity readout in circuit quantum electrodynamics using the Jaynes-Cummings nonlinearity. Phys. Rev. Lett. **105**, 173601 (2010). Cited on page 106

[229] F. Yan, S. Gustavsson, J. Bylander, X. Jin, F. Yoshihara, D. G. Cory, Y. Nakamura, T. P. Orlando, W. D. Oliver. Rotating-frame relaxation as a noise spectrum analyser of a superconducting qubit undergoing driven evolution. Nature Communications **4**, 2337 (2013). Cited on page 109

[230] M. Scala, B. Militello, A. Messina, J. Piilo, S. Maniscalco. Microscopic derivation of the Jaynes-Cummings model with cavity losses. Phys. Rev. A **75**, 013811 (2007). Cited on page 112

[231] J. Gambetta, A. Blais, M. Boissonneault, A. A. Houck, D. I. Schuster, S. M. Girvin. Quantum trajectory approach to circuit QED: Quantum jumps and the Zeno effect. Phys. Rev. A **77**, 012112 (2008). Cited on page 112

[232] C. Aron, M. Kulkarni, H. E. Türeci. Photon-mediated interactions: A scalable tool to create and sustain entangled states of N atoms. Phys. Rev. X **6**, 011032 (2016). Cited on page 112

[233] Y. Liu, A. A. Houck. Quantum electrodynamics near a photonic bandgap. Nature Physics **13**, 48 (2017). Cited on page 112

[234] G. Lindblad. On the generators of quantum dynamical semigroups. Commun. Math. Phys. **48** (1976). Cited on page 112

[235] D. A. Steck. *Quantum and Atom Optics* (2019). Cited on page 113

[236] M. Baur, S. Filipp, R. Bianchetti, J. M. Fink, M. Göppl, L. Steffen, P. J. Leek, A. Blais, A. Wallraff. Measurement of Autler-Townes and Mollow transitions in a strongly driven superconducting qubit. Phys. Rev. Lett. **102**, 243602 (2009). Cited on page 113

[237] D. M. Toyli, A. W. Eddins, S. Boutin, S. Puri, D. Hover, V. Bolkhovsky, W. D. Oliver, A. Blais, I. Siddiqi. Resonance fluorescence from an artificial atom in squeezed vacuum. Phys. Rev. X **6**, 031004 (2016). Cited on page 113

[238] B. R. Mollow. Power spectrum of light scattered by two-level systems. Phys. Rev. **188**, 1969 (1969). Cited on page 113

[239] J. Raftery, D. Sadri, S. Schmidt, H. E. Türeci, A. A. Houck. Observation of a dissipation-induced classical to quantum transition. Phys. Rev. X **4**, 031043 (2014). Cited on page 113

[240] H. J. Carmichael, A. S. Lane, D. F. Walls. Resonance fluorescence from an atom in a squeezed vacuum. Phys. Rev. Lett. **58**, 2539 (1987). Cited on page 118

[241] M. C. Collodo, A. Potočnik, S. Gasparinetti, J.-C. Besse, M. Pechal, M. Sameti, M. J. Hartmann, A. Wallraff, C. Eichler. Observation of the crossover from photon ordering to delocalization in tunably coupled resonators. Phys. Rev. Lett. **122**, 183601 (2019). Cited on page 120

[242] C. Sayrin, I. Dotsenko, X. Zhou, B. Peaudecerf, T. Rybarczyk, G. Sebastien, P. Rouchon, M. Mirrahimi, H. Amini, M. Brune. Real-time quantum feedback prepares and stabilizes photon number states. Nature **477**, 73 (2011). Cited on page 120

[243] R. Vijay, C. Macklin, D. H. Slichter, S. J. Weber, K. W. Murch, R. Naik, A. N. Korotkov, I. Siddiqi. Stabilizing Rabi oscillations in a superconducting qubit using quantum feedback. Nature **490**, 77 (2012). Cited on page 120

[244] D. Ristè, M. Dukalski, C. Watson, G. de Lange, M. Tiggelman, Y. Blanter, K. Lehnert, R. Schouten, L. DiCarlo. Deterministic entanglement of superconducting qubits by parity measurement and feedback. Nature **502**, 350 (2013). Cited on page 120

[245] G. de Lange, D. Ristè, M. J. Tiggelman, C. Eichler, L. Tornberg, et al. Reversing quantum trajectories with analog feedback. Phys. Rev. Lett. **112**, 080501 (2014). Cited on page 120

Appendix A

Quantum Operator Methods

Moving to the rotating frame

In the Schrödinger picture, the Hamiltonian operating on a state ψ is

$$H\psi = i\partial_t\psi = i\dot{\psi}. \tag{A.0.1}$$

A unitary transformation of the states ψ defines eigenstates $\psi' = U\psi$ of a Hamiltonian H'. We solve for the Hamiltonian H' in terms of the original Hamilotnian H by the relation,

$$\begin{aligned} H'\psi' &= i\partial_t\psi' \\ &= i\partial_t\big(U\psi\big) \\ &= iU(\partial_t\psi) + i\big(\partial_t U\big)\psi \\ &= UHU^\dagger\psi' + i\dot{U}U^\dagger\psi' \\ H'\psi' &= \big(UHU^\dagger + i\dot{U}U^\dagger\big)\psi'. \end{aligned} \tag{A.0.2}$$

While the states transform as $\psi \to \psi' = U\psi$, we find the Hamiltonian transforms as

$$H \to H' = UHU^\dagger + i\dot{U}U^\dagger. \tag{A.0.3}$$

A transformation into a rotating frame is often used to eliminate terms from a Hamiltonian. If the time evolution is explicitly expressed by a unitary transformation, then the Hamiltonian terms which would otherwise generate this time evolution can be eliminated.

The Rotating Wave Approximation

We examine the rotating wave approximation in the context of two coupled harmonic oscillators. The coupling of quantum harmonic oscillators can be solved readily in the classical limit and then performing quantization of the coupled modes. However, we develop an intuition of the rotating wave approximation by considering the physics of coupled modes at the quantum limit.

We approximate the interaction of two electromagnetic modes as a dipole coupling

when excitations of both modes have a similar energy scale which is relatively strong compared to the interaction strength. Two independent electromagnetic modes, defined by commuting annihilation operators a and b have a dipole-dipole interaction described by the Hamiltonian

$$\hat{H} = \underbrace{\omega_a a^\dagger a}_{\hat{H}_a} + \underbrace{\omega_b b^\dagger b}_{\hat{H}_b} + \underbrace{4g x_a x_b}_{\hat{H}ab}, \tag{A.0.4}$$

where $x_a = (a + a^\dagger)/2$ is the field amplitude of mode a which is coupled to the field amplitude x_b for mode b, chosen up to the phase of the field without loss of generality.

We investigate the time evolution of the coupled system by transforming the Hamiltonian (Eq. A.0.4) into the interaction picture defined from the uncoupled modes. In the interaction picture, the operators evolve as $A \to A(t) = UAU^\dagger$ with the unitary operator $U = e^{i(\hat{H}_a + \hat{H}_b)t}$. In the interaction picture, we define an interaction Hamiltonian by the relation $\hat{H}(t) = \hat{H}_a + \hat{H}_b + \hat{V}(t)$, which has the time evolution

$$\hat{V}(t) = g(ae^{-i\omega_a t})(b^\dagger e^{+i\omega_b t}) + g(ae^{-i\omega_a t})(be^{-i\omega_b t}) + \text{h.c.} \tag{A.0.5}$$

$$= ga\left(e^{+i\Delta t}b^\dagger + e^{-i\Sigma t}b\right) + \text{h.c.} \tag{A.0.6}$$

where $\Delta = \omega_b - \omega_a$ and $\Sigma = \omega_b + \omega_a$ are the detuning and sum of uncoupled frequencies. The interaction terms which time evolve at the sum of the uncoupled mode frequencies are dubbed *counter-rotating* terms. Notably, the counter-rotating terms are considered off-resonant processes which do not conserve excitation number.

The interaction Hamiltonian in the rotating wave approximations is

$$\hat{V}(t) = ge^{+i\Delta t}ab^\dagger + \text{h.c.}, \tag{A.0.7}$$

where we have omitted counter-rotating terms from the interaction Hamiltonian. This approximation is applicable based on our initial assumptions to justify a dipole interaction: weak coupling ($g \ll \omega_a, \omega_b$) and the uncoupled mode excitation energies that are of similar scale ($\Delta \ll \Sigma$). The rotating wave approximation is physically motivated by the rapid evolution time scale of the counter-rotating terms. The operators evolving at rate Σ describe interaction processes, i.e. two photon transitions, which do not contribute significantly to the interaction dynamics which evolve at much rates ($g, \Delta \ll \Sigma$).

Appendix B

Photonic Crystal Fabrication Parameters

Table B.1 displays lengths of the 25 impedance sections referenced for fabrication of the photonic crystal filter discussed in Chapter 6.

Step #	Z_0 (Ω)	ℓ (mm)	Step #	Z_0 (Ω)	ℓ (mm)
1	30	9.1	14	50	9.7
2	50	9.4	15	30	10.2
3	30	9.1	16	50	9.7
4	50	10.7	17	30	10.2
5	30	9.7	18	50	9.7
6	50	9.4	19	30	9.9
7	30	9.9	20	50	9.4
8	50	9.7	21	30	9.7
9	30	10.2	22	50	10.9
10	50	9.7	23	30	9.1
11	30	10.2	24	50	9.4
12	50	9.7	25	30	9.1
13	30	10.2	—	—	—

Table B.1: The photonic crystal filter was fabricated by creating a modulation of the characteristic impedance Z_0 of a transmission line. The photonic crystal is modeled as a Chebychev type-I bandstop filter. The lengths of the impedance sections were informed from filter simulations in AWR Microwave Office.